5-2023

The Growth and Characterization of InN Quantum Dots Using Droplets Epitaxy in MBE

Malak Refaei
University of Arkansas-Fayetteville

Citation

Refaei, M. (2023). The Growth and Characterization of InN Quantum Dots Using Droplets Epitaxy in MBE. *Graduate Theses and Dissertations* Retrieved from https://scholarworks.uark.edu/etd/4987

The Growth and Characterization of InN Quantum Dots Using Droplets Epitaxy in MBE

A dissertation submitted in partial fulfillment
of the requirements for the degree of
Doctor of Philosophy in Microelectronics-Photonics

by

Malak Refaei
Jazan University
Bachelor of Science in Physics, 2011
University of Arkansas
Master of Science in Microelectronics-Photonics, 2017

May 2023
University of Arkansas

This dissertation is approved for recommendation to the Graduate Council.

Morgan Ware, Ph.D.
Dissertation Director

Min Zou, Ph.D. Committee Member	Hugh Churchill, Ph.D. Committee Member
Zhong Chen, Ph.D. Committee Member	Matt Leftwich, Ph.D. Ex-Officio Member

The following signatories attest that all software used in this dissertation was legally licensed for use by Malak Refaei for research purposes and publication.

Mrs. Malak Refaei, Student
Dr. Morgan Ware, Dissertation Director

This dissertation was submitted to http://www.turnitin.com for plagiarism review by the TurnItIn company’s software. The signatories have examined the report on this dissertation that was returned by TurnItIn and attest that, in their opinion, the items highlighted by the software are incidental to common usage and are not plagiarized material.

Dr. Matt Leftwich, Program Director
Dr. Morgan Ware, Dissertation Director

Abstract

III-nitride semiconductor material systems offer great potential for next-generation optoelectronic devices due to their direct bandgaps, which vary from 0.7 eV (InN) to 3.5 eV (GaN) to 6.2 eV (AlN), as well as their other unique properties. InN has gained much less attention than GaN and AlN within this family of semiconductors due to its complicated low-temperature growth. However, the prediction that an InN quantum well on GaN can become a two-dimensional (2D) topological insulator has resulted in expanding the research interest in InN. At the same time, this renewed interest has begun to reveal that the formation of an appropriate 2D InN film is difficult at best and physically forbidden by strain at worst. This has shifted the focus on InN to 3D nanostructures in an attempt to achieve similar novel affects. However, this shifted focus has revealed a challenging landscape for the study of the growth of these 3D nanostructures. This research has focused on investigating the growth of InN quantum dots (QDs) by droplet epitaxy (DE) using radio frequency plasma-assisted molecular beam epitaxy (MBE) in order to discover and learn to control the growth kinetics of this novel system.

The QD growth kinetics from the formation of liquid In droplets to the crystallization of InN QDs was studied with a focus on the effects of ambient nitrogen and substrate type and temperature. The substrates studied were c-plane sapphire and (0001) GaN, while the temperature varied from nearly room temperature to ~400 °C. The growth quality, dot density, diameter, and height of In droplets as well as InN QDs were investigated utilizing reflection high-energy electron diffraction (RHEED), X-Ray Diffraction (XRD), Atomic Force Microscopy (AFM*)*, and Scanning Electron Microscopy (SEM).

The droplet formation was determined to follow well known principles of nucleation theory with ripening. By analyzing the areal density of nanostructures as functions of

temperature, the corresponding activation energies for surface diffusion where determined. The resulting activation energy for In surface diffusion on sapphire was found to be 0.62 ± 0.07 eV in ultra-high vacuum, ~10^{-10} Torr, and 0.57 ± 0.08 eV in ambient N_2, ~10^{-5} Torr. For the InN QDs on GaN, the resulting activation energy for In surface diffusion on GaN was found to be 0.23 ± 0.03 eV. In addition, it was found that by analyzing the density of crystallized QDs, following the droplet formation under ambient N_2, a very close activation energy of 0.25 ± 0.1 eV was found.

Acknowledgements

First of all, I would like to thank “Allah Almighty” for giving me the strength, patience, and the ability to undertake this research and complete it successfully. This research would not have been achieved without his blessings.

I would like to express my sincere gratefulness and thankfulness to my research’s advisor Dr. Morgan Ware for providing his support, motivation, and guidance at all times throughout this research. He has given me the freedom to explore my research, but at the same time, he has always been there to assist me whenever I was stuck and to guide me to not deviate from the primary goals of my research. He has taught me the way to carry out this study and to present my research as clearly as possible. It was a great honor to work under his supervising. Also, I would like to thank him for his friendship, empathy, and a great sense of humor.

I would like to thank Dr. Matt Leftwich, my academic advisor, for his guidance and encouragements. He was always there to answer my questions, to advise, and to support whenever I needed. I am very thankful to him for spending time reading my dissertation.

I would like to thank my research group, Pijush and Rohith for helping and training on the MBE device, and Saeed Sarollahi for his support and guidance. I also would like to thank the rest of the group for the good time and support throw-out this journey. I would like to thank Mohammad Zamani Alavijeh for the training on AFM. I would like to thank Dr. Mourad Benamara for his help in answering some of my questions and training on SEM, EDX and XRD. Finally, I would like to thank Dr. Fernando Maia de Oliveira and Dr. Yuriy Mazur for their assistance in doing the optical measurements.

In my journey towards my doctoral degree, I have faced many obstacles and difficulties, and I would not have complete this degree without the support of my husband, Mr. Mohammed

Reefai. I am deeply thankful for his love, friendship, support, encouragement, motivation, understanding, and prayers. I also would like to thank my children, Yazan, Abdulmajeed, and Farah for their patience and understanding when I could not be there with them. I am very thankful to my parents, Amena and Ibrahim, for their love, support, prayers, caring and preparing me to be successful person in my life. Also, I express my thanks to my sister, Amwaj, and my brothers.

Dedication

I dedicate this thesis to my husband Mohammed Reefai whose support made this degree possible to complete. His friendship and love made my journey here remarkable and memorable. Also, I dedicate this thesis to my children, Yazan, Abdulmajeed, and Farah. To my dear parents, Amena and Ibrahim, who supported and encouraged me to pursue my education. Furthermore, I would like to dedicate my thesis to my sister, Amwaj, and my brothers for their love, support, prayers, and encouragement.

Table of Contents

Chapter 1: Motivation and Organization of the Dissertation 1

Chapter 2: Background and the future application.. 5

- 2.1 Quantum Computing.. 5
- 2.2 Topological Insulators 6
- 2.3 III-Nitride Semiconductor Materials.. 7
  - 2.3.1 Crystalline Structure 8
  - 2.3.2 Growth Limitations... 10
  - 2.3.3 Quantum Dots of III-Nitride Materials 10
- 2.4 The Basic Principle of Nanomaterial growth.. 11
  - 2.4.1 Quantum Confinement Effects 11
  - 2.4.2 Quantum Confined Stark Effect (QCSE).. 15
  - 2.4.3 Growth of Quantum Dots.. 16
  - 2.4.4 Nucleation 20

Chapter 3: Indium Nitride Quantum Dots Growth and Characterizations Techniques............. 27

- 3.1 Molecular Beam Epitaxy 27
- 3.2 In situ real-time material characterization RHEED 30
- 3.3 Structural Characterization Techniques 33
  - 3.3.1 Atomic Force Microscopy 34
  - 3.3.2 Scanning Electron Microscopy 35
  - 3.3.3 X-ray Diffraction 37
- 3.4 Opticale Characterization Techniques 40
  - 3.4.1 Raman spectroscopy 40

Chapter 4: Controlling the Density and Size of InN QDs formed on Sapphire Substrate via Droplet Epitaxy 43
4.1 Introduction 43
4.2 Experimental Methods 45
4.3 Results and Discussion 46
4.5 Conclusion 57
Chapter 5: Investigating self-assembled strain free growth of InN QDs grown on GaN using droplet epitaxy. 58
5.1 Introduction 58
5.2 The growth of In droplets on GaN under ultra high vaccum 61
5.3 The growth of In droplets on GaN under low vacuum conditions 69
5.4 The growth of InN QDs on GaN 76
5.5 Capping the InN QDs with GaN layer 99
5.6 Conclusion 108
Chapter 6: Conclusions and Future Work 109
References 113
Appendix A: Description of Research for Popular Publication 123
Appendix B: Executive Summary of Newly Created Intellectual Property 125
Appendix C: Potential Patent and Commercialization Aspects of Listed Intellectual Property Items 126
Appendix D: Broader Impact of Research 127
Appendix E: Microsoft Project for PhD MicroEP Degree Plan 128
Appendix F: Identification of All Software Used in Research and Dissertation Generation... 129

Appendix G: All Publications Published, Submitted and Planned.. 130

List of Figures

Figure 1: A comparison between (a) a bit in the classical computer and (b) qubit in the quantum computer [9]. 5

Figure 2: Semiconductors electronic band showing the bands at zero gap transition and the inverted [5]. 6

Figure 3: Diagram of bandgap versus lattice constants for III-nitride materials [12]. 7

Figure 4: An illustration of the wurtzite lattice structure (a) and the zincblende lattice structure (b) of III-nitrides element with N atoms [21]. 9

Figure 5: An illustration of a direct band gap semiconductor diagram. 12

Figure 6: Schematic of quantum confinement effect on the density of states for: (a) a three-dimensional system or bulk, (b) a two-dimensional system or quantum well, (c) a one-dimension system or quantum wire, and (d) a zero-dimension system or quantum dot [39]. 13

Figure 7: Schematic sketch of a three-dimensional quantum box with the dimensions: Lx, Ly, and Lz [40]. 14

Figure 8: A schematic represents the band diagram of (a) the quantum well (b) the QCSE in InGaN/GaN. 16

Figure 9**:** An illustration of the three heteroepitaxial growth modes [37]. 18

Figure 10**:** Schematic of the droplet epitaxy of InN QDs. 19

Figure 11: Schematic of the surface tension in a liquid. 20

Figure 12: Schematic illustration of different liquid formations on a solid substrate. 21

Figure 13: A graphic of the process of depositing vapor atoms on a substrate’s surface [37]. 22

Figure 14: Coalescence of clusters as a result of a) Ostwald ripening, b) Sintering, and c) migration. 25

Figure 15: GEN II Molecular Beam Epitaxy. 27

Figure 16: Schematic illustration of the PAMBE growth chamber [63]. 29

Figure 17: Sketch of the RHEED setup inside the MBE chamber [64]. 30

Figure 18: An illustration of the streaky RHEED pattern of a plane GaN surface and the intensity profile. 31

Figure 19: Schematic illustration of intensity oscillation of a monolayer growth as presented via RHEED [37]. 32

Figure 20: Schematic illustration of the AFM system. 34

Figure 21: (a) A sketch of the Scanning Electron Microscope column, and (b) the interactions among the electrons beam and the sample’s surface [69]. 36

Figure 22: An illustration of Energy Dispersive X-ray Spectroscopy spectrum presenting the chemical composition of each element and an inserted SEM image. 37

Figure 23: Schematic sketch for the Bragg condition. 38

Figure 24: An illustration schematic of the XRD system [73]. 39

Figure 25: An illustration of Stokes, anti-Stokes, and Rayleigh scattering procedures [76]. 41

Figure 26: XRD 2θ/ω XRD pattern of In droplets grown on a c-plane sapphire substrate at different $Tsub$, 200 °C, 300 °C, and 400 °C without employing the nitrogen flow or the plasma power and a reference for the c-plane sapphire substrate. 46

Figure 27: XRD $2\theta/\omega$ XRD pattern of In droplets grown on a c-plane sapphire substrate at different $Tsub$,200 °C, 300 °C, and 400 °C with the RF plasma on and nitrogen shutter closed. 47

Figure 28: XRD $2\theta/\omega$ pattern of In droplets grown on sapphire substrate at different $Tsub$ (g) 200 °C, (h) 300 °C, and (i) 400 °C and crystallized for 15 mins at the same $Tsub$, and (k) is for the In droplets grown at $Tsub$ 400 °C and crystallized for 15 mins at 450 °C. 48

Figure 29: AFM images of (2 × 2) μm of In droplets formed on sapphire substrate at different substrate growth temperatures (a and d) 200 °C (b and e) 300 °C (c-f) 400 °C. Samples (a-c) were grown without plasma or nitrogen flow and samples (d-f) were grown using plasma and nitrogen flow rate, but the nitrogen shutter closed. 50

Figure 30: Cross-sectional line-profiles of In droplets on sapphire at different substrate growth temperatures. 50

Figure 31: AFM images of (2 × 2) μm of InN QDs formed on sapphire substrate at same growth and crystallization substrate temperatures (a) 200 °C, (b) 300 °C to (c) 400 °C, but (d) shows the InN QDs grown at 400 °C crystallized at 450 °C. 51

Figure 32: Cross-sectional line-profiles of InN QDs grown at various substrate growth temperatures, (a) 200, (b) 300 to (c) 400 °C, but (d) shows the InN QDs grown at 400 °C and crystallized at 450 °C. 52

Figure 33: RHEED pattern of (a) sapphire substrate, (b) In DE, and (c) the nitridated QDs at 400 °C. 53

Figure 34: The dot density (a), height (b), and diameter (c) of the In droplets and InN QDs are plotted as a function of substrate temperatures. 54

Figure 35: Arrhenius plot of quantum dot density grown using three different approaches: 1) UHV droplet growth, 2) N2 ambient droplet growth, and 3) N plasma crystallized InN QDs growth. 55

Figure 36: The band structure of GaN/InN/GaN for two different QW thicknesses without strain in (a) and (b) and with strain in (c) and (d). 59

Figure 37: The transition energy in the QDs as a function of different InN thickness. 60

Figure 38: $2\theta/\omega$ XRD pattern of In droplets grown on a GaN buffer layer at different $Tsub$ under high vacuum. 63

Figure 39: AFM images of (5 × 5) μm of In droplets formed on GaN buffer layer at different $Tsub$. 64

Figure 40: Cross-sectional line-profiles of the grown In droplets at different substrate growth temperatures. The white lines in 2D AFM insets indicate the line-profiles. The length of each line profiler is 900 nm for (a-d) images and 3.5 μm for (e-g) images. Each line profile corresponds to each AFM figure. 64

Figure 41: SEM images for the samples grown at 200, 300, and 400 °C. 65

Figure 42: The density (a), diameter (b), and height (c) of the In droplets are plotted as a function of substrate temperatures. 67

Figure 43: Arrhenius plot of quantum dot density as a function of (1/kT) at (a) low (30, 50, 75, and 95 °C) and (b) high (200, 300, and 400 °C) substrate growth temperatures. 68

Figure 44: $2\theta/\omega$ XRD pattern of In droplets grown on a GaN buffer layer at different $Tsub$ under low vacuum. 71

Figure 45: AFM images of (5 × 5) μm of In droplets formed on GaN at different substrate growth temperatures 30, 50, and 100 for 30 sec under ambient nitrogen pressure. 72

Figure 46: Cross-sectional line profiles of In droplets grown at different $Tsub$ under ambient nitrogen pressure. 72

Figure 47: The density (a), diameter (b), and height (c) of the In droplets formed in ambient N2 versus $Tsub$ 73

Figure 48: Arrhenius plot of In droplets density formed in ambient N_2 versus growth temperature (1/kT). 75

Figure 49: An illustrating of two different growth methods utilized to crystalize the In droplet a)) at 500 °C and b) at 380 °C and annealed at 380 °C for 3 min. 76

Figure 50: RHEED patterns detected at each phase of the droplet epitaxy InN QDs growth used in the first case. 79

Figure 51: RHEED patterns detected at each phase of the droplet epitaxy InN QDs growth used in the second case. 80

Figure 52: $2\theta/\omega$ XRD pattern of the droplet epitaxy InN QDs growth on GaN via the second case. 81

Figure 53: a 3D and 2D AFM images of (2 × 2) μm of the droplet epitaxy InN QDs growth on GaN via the second case. 82

Figure 54: An illustrated of the steps of the formation of droplet epitaxial InN QD on GaN. 83

Figure 55: (a) XRD pattern and (b) FWHM of InN QDs at different substrate growth temperatures. 85

Figure 56: an illustration of the RHEED patterns detected at each period of the droplet epitaxy growth of InN QDs for the sample grown at 150 °C. 85

Figure 57: An illustration of RHEED pattern: (a) streaky, (b) spotty, and (c) the intensity profile of data taken from the sample grown at 150 °C and crystallized at 380 °C. 86

Figure 58: AFM of (10 × 10) μm images of the InN QDs formed at various growth temperatures. 87

Figure 59: AFM of (5 × 5) μm of the samples grown at $\leq$ 100 **(°C)** before crystallization and under a nitrogen ambient pressure of ~$10-5$ Torr in (a-c) and after crystallization in (d-f). 88

Figure 60: An illustration of the inner ring (R1) and the outer disk radius (R2) (a) and the mean radius (ΔR) versus the inverse temperatures (b). 89

Figure 61: Cross-sectional line profiles of the droplet epitaxy InN QDs grown at different $Tsub$. 91

Figure 62: The density (a), height (b), and diameter (c) of InN QDs on GaN. 92

Figure 63: Arrhenius plot of InN QDs density formed on GaN at different growth temperatures (1/kT). 93

Figure 64: An illustration of the InN QDs growth procedures at shorter (a) and longer (b) crystallization duration. 94

Figure 65: $2\theta/\omega$ XRD pattern of the droplet epitaxy InN QDs on GaN for two different crystallization durations. 96

Figure 66: RHEED pattern of InN QDs grown on GaN using two different crystallization times. 97

Figure 67: AFM of (10 × 10) μm images of the InN QDs formed using two different crystallization times. 98

Figure 68: Cross-sectional line profiles of the droplet epitaxy InN QDs crystallized for two different time. 99

Figure 69: A graphic illustration of the structure of the capped InN QDs. 100

Figure 70: AFM images of uncapped InN QDs (a-b) and capped InN QDs via various approaches (c-f). 102

Figure 71: XRD measurements of InN QDs capped with GaN layer using three different procedures. 103

Figure 72: SEM images and the EDX mapping results of the grown GaN capped layer on InN QDs of three different samples: a) NL 227 b) NL 231 and c) NL 232, and EDX spectra of the spherical shaped and surrounding surface. 104

Figure 73: Raman spectroscopy measurement for capped InN QDs with GaN grown at different temperatures and thickness. 105

Figure 74: PL spectra of uncapped InN QDs with GaN and InN film at 77 K. 106

Figure 75: PL spectra of uncapped and capped InN QDs with GaN at room temperature. 107

List of Tables

Table 1: The lattice constants of InN and GaN [19], [20]. 9

Table 2: In droplets' height, diameter, and density at different substrate temperatures formed under UHV.. 66

Table 3: In droplets' height, diameter, and density at different substrate temperatures................ 74

Table 4: The values of the radius of the inner ring and outer disk along with the density, diameter, and height of InN QDs in the outer disk.. 90

Table 5: the diameter, height, and density of InN QDs crystallized for two different times........ 97

Chapter 1: Motivation and Organization of the Dissertation

Computers have been developing very rapidly in the last few decades to become much smaller and more efficient. Despite these fast developments, many complicated computing problems still cannot be solved and show no potential to be able to be solved in the future [1]. Additionally, the current transistors, which are the main components of current computers, are exposed to many essential and challenging complications to address the growing request for smaller computers. Researchers have also demonstrated that the existing computers have almost achieved their limitations, according to Moore's Law [2], [3]. Therefore, in order to get smaller and more highly efficient computers to solve very complicated problems, obtaining a radically new approach to computing becomes a requirement.

A quantum computer utilizes the properties of quantum phenomena, including superposition and entanglement, to process data. These new computers can deliver efficient solutions for computationally critical problems, which are considered impossible to solve by standard classical computers [1]. Several quantum systems have been demonstrated as potential quantum bits (qubits) for quantum information or quantum computing. However, these qubit technologies face the challenge of maintaining coherence, which is inherently destroyed by the thermal bath in which they exist. The thermal fluctuations make the qubits susceptible to losing their coherence faster, failing the quantum computing process. One of the procedures utilized in the most widespread implementations of existing quantum computing is to cool the system to surmounted decoherence. This procedure is costly and time consuming. Thus, an implementation of quantum computing, which remainscoherent at room temperature, can be a substantial advancement [4]. At the very least, a system that could maintain its coherence at liquid nitrogen temperatures would provide a considerable advantage. Topological insulators provide a mechanism in which spins can be “forced” to remain in their state, which is called protected states. The spins of confined charges can then be used as qubits, with their spin “protected” by the topological phase from the environment.

The internal field present in thin InN quantum wells (QWs) due to internal polarization effects was predicted to drive the system to the topological insulating state as a result of the band edge inversion due to strain [5]. This idea was the primary motivation to do this research. However, instead of growing QWs with more than three monolayers of InN, which is challenging due to strain-relaxation, the quantum dots (QDs) were grown with the intention of reaching the same height that topolocical properties are found. The QDs have a high potential for scalability, either from self-assembly or from novel “top-down” approaches, but most QD systems have very small confinements on the order of a few tenths of an electron volt. However, indium nitride (InN) can form QDs in a gallium nitride (GaN) matrix where the bulk band offset between the two materials creates confinement energy of approximately 2.5 eV. This InN/GaN system may offer advantages of not only large confinements and scalability but also long recombination lifetimes [6] and theoretically predicted topologically protected spin states [5] both resulting from the large polarization fields, which are inherent in the III-nitride semiconductor system. Additionally, it is possible to grow InN in an aluminum nitride (AlN) matrix where the confining energy barrier could exceed 4 eV. This research is a very early step towards linking this material to quantum computing applications. It focused on the development of self-assembled strain-free growth of InN QDs via droplet epitaxy technique.

The aim here was to use a zero-dimensional quantum dot to reach larger thicknesses without plastic relaxation The initial approach was to investigate the growth of the In droplets and InN QDs. As it is well known that InN grows better at relatively lower temperatures while GaN grows better at a relatively higher temperature. Consequently, the main challenge here was to grow a high quality GaN on a high quality InN QDs without destroying the QDs.

Organization of dissertation

In this dissertation, the challenges faced in developing self-assembled strain-free formation of InN QDs via the droplet epitaxy technique in the MBE were addressed.

Chapter 2 introduces the fundamental concepts of III-nitride materials including crystalline structure, materials limitation, and quantum dot of III-nitride materials. Also, the basic principle of nanomaterial growth is reviewed, and the growth of quantum dots is covered.

Chapter 3 reviews the experimental techniques utilized to grow and investigate the InN QDs. These experimental techniques include the growth process, structure analysis, and optical analysis.

Chapter 4 discusses the control of density and size of InN QDs grown sapphire substrate by the DE approach. Nanostructures were formed under three different conditions for comparison: UHV with no exposure to nitrogen; ambient of nitrogen equivalent having the plasma on but shuttered; and nitridated with the direct nitrogen plasma following droplet formation with the plasma on but shuttered. The size, density, and shape of In droplets and InN QDs were studied via controlling the substrate growth temperature throughout the In droplets growth and the crystallization process and were explained via the In atom surface diffusion. The droplet formation was determined to follow well known principles of nucleation theory with ripening. The resulting activation energy for In surface diffusion on sapphire was found to be 0.62 ± 0.07 eV in ultra-high vacuum, ~10^{-10} Torr, and 0.57 ± 0.08 eV in ambient N2, ~10^{-5} Torr. These results should aid in the future development and understanding of InN QDs and QD based devices.

Chapter 5 covers the InN QDs formation on GaN via the droplet epitaxy technique. In order to control the height of InN QDs, the conditions for growing In droplets was first studied at different growth temperatures and under ultra-high vacuum of less than 10^{-9} Torr and under a nitrogen ambient pressure of ~10^{-5} Torr. Then, studying the crystallization conditions of the In droplets with nitrogen-plasma in the MBE growth chamber was accomplished. In addition to forming the QDs, a low temperature GaN cap film was formed on the InN QDs.

Chapter 6 summarizes the key results of this dissertation and suggested the future works.

Chapter 2: Background and the future application

2.1 Quantum Computing

Quantum phenomena, including entanglement and superposition, can be harnessed to process information to solve more complex problems than are possible with standard classical computers [1]. Quantum computers can provide a significant potential for many practical applications due to their ability to provide an effective solution for computationally critical problems. For example, the ability to factorize a large number in a short time leads to the ability to break standard encryption algorithms [7]. Also, the simulation of quantum systems enhances the analytical powers of simulating materials and their chemical reactions for a wide range of areas [8].

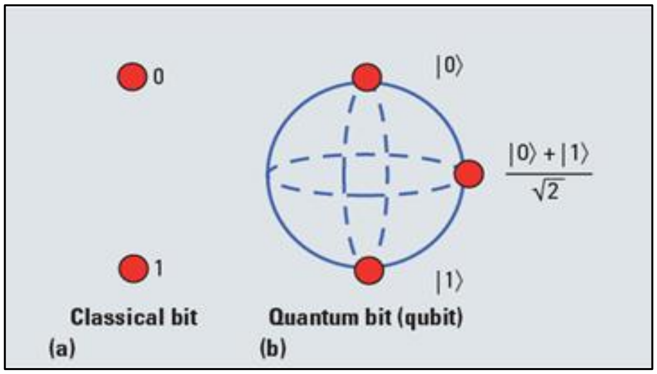

Figure 1: A comparison between (a) a bit in the classical computer and (b) qubit in the quantum computer [9].

The quantum computers utilize quantum-bits or “qubits” to process data instead of bits in standard computers. The bit can be represented either as 0 or 1, while qubits exist as “0” and “1” at the same time, which is named a superposition, as shown in figure 1 [9]. This superposition state can be controlled, manipulated, and allowed to interact quantum-mechanically with other qubits [4], [8]. These qubits will stay in the superposition states for only a short time. During this time, when they are allowed to interact with each other, they could unintentionally interact with their environment leading to the decoherence of the system. Thus, quantum error correction has been recommended to minimize the problems resulting from decoherence. This, however, is still noisy, and in-fact introduces more errors during the correction process. Therefore, this error correction cannot overcome decoherence unless the error rate is particularly low. A standard benchmark for this is at least 10,000 operations before recording any errors, which is very difficult to achieve through current quantum error correction techniques [8].

2.2 Topological Insulators

In general, materials are divided into three categories based on their energy bandgap, which is located between valence bands and conduction bands according to the band theory of solids. The three categories of materials are conductors, semiconductors, and insulators.

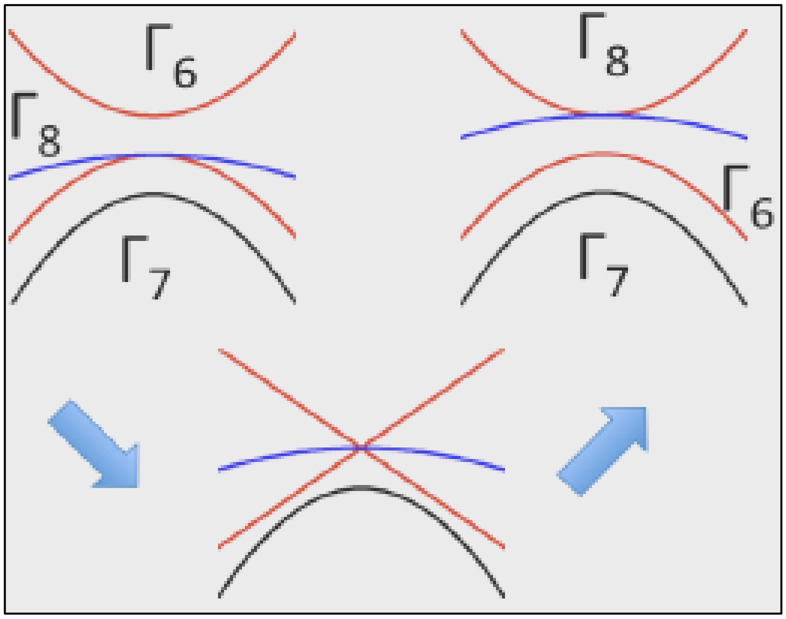

Figure 2: Semiconductors electronic band showing the bands at zero gap transition and the inverted [5].

Nevertheless, a new phase of a quantum matter, which performs as an electrical insulator in its bulk with conducting electronic states on its surface, has been recently discovered. This new state of quantum matter, which is identified as a topological insulator (TI) (figure 2), exhibits useful properties because of its sturdy spin orbit coupling effects and its inherent time reversal symmetry. This can suppress the effects of impurity scattering. The quantum state of a topological insulator is very stable, which could increase the possibility of using it for quantum computation.

Moreover, this TI state could potentially be obtained in semiconductor materials through band inversion along with a strong spin-orbit interaction (SOI) resulting from “heavy atoms.” Additionally, utilizing an external electric field or changing the strain, have been proposed to force a system into the TI state [10], [11], [5].

2.3 III-Nitride Semiconductor Materials

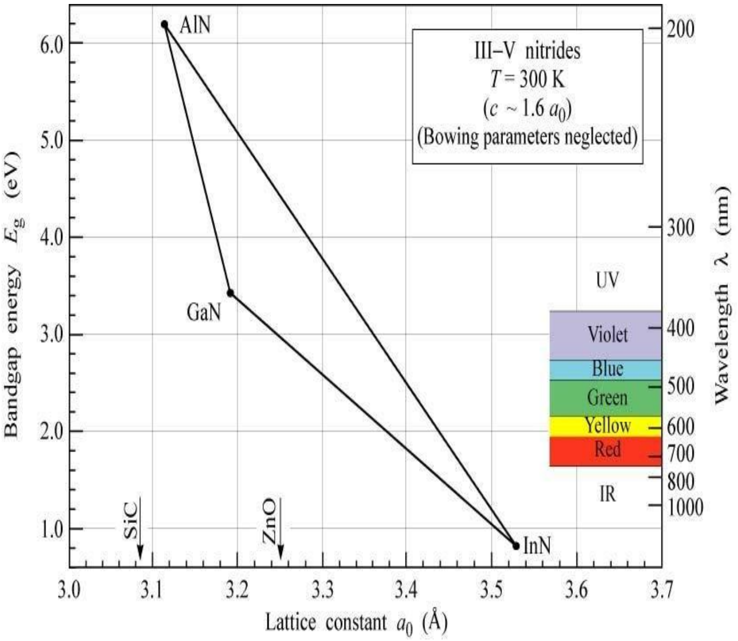

Figure 3: Diagram of bandgap versus lattice constants for III-nitride materials [12].

III-nitride semiconductor material systems offer a potential candidate for next-generation nanodevices because of their direct bandgaps, which vary from 0.7 eV (InN) to 6.2 eV (AlN), figure 3 [12], as well as their other unique properties such as strong excitonic effects, significant absorption coefficients, radiation tolerance, and high-saturation velocities [13]. InN has gained much less attention than GaN and AlN within this family of semiconductors due to its complicated low-temperature growth. However, the prediction that an InN quantum well in GaN can become a two dimensional (2D) topological insulator [5] has resulted in expanding the research interest of InN. At the same time, this renewed interest has begun to reveal that InN may have some growth limitations which might prevent reaching this topological state in this material.

2.3.1 Crystalline Structure

The crystal structure of the III-nitride semiconductor materials can be zincblende (zb), rock-salt, and wurtzite (wz) structures [14]–[16]. The wz structure is more thermodynamically stable than the other two structures. The zinc blende is a metastable structure, while the rock-salt structure can be grown only under high pressures and cannot be developed as an epitaxial film. The zinc blende structure of InN possesses a cubic lattice symmetry, but the wurtzite structure of InN has hexagonal lattice symmetry [16].

The indium atom possesses three valence electrons, while the nitrogen atom has five. This results in InN having four covalent bonds to form tetrahedral structures [17]. Each covalent bond is created when a nitrogen atom shares an electron pair with an indium atom. Therefore, four nitrogen neighbors surround one central indium atom generating a tetrahedron.

In the wz structure, the hexagonal unit cell has two indium atoms and two nitrogen atoms, as presented in figure 4a, and possesses a- and c-lattice constants. A summary of the structural parameters of InN and GaN is presented in table 1.

The direction of the c-lattice constant, which defines the height of the unit cell, is along the [0001]. There are two interpenetrating hexagonal close-packed (HCP) sublattices in the wz structure. The HCP has the same species of atoms. The optimum wz structure possesses a c/a =

1.633 lattice ratios and u = 3/8 = 0.375 of a lattice distortion [15], [16], [18] The lattice ratio is associated with spontaneous polarization, and the lattice distortions are linked to the anisotropic nature of the wz structure.

Table 1: The lattice constants of InN and GaN [19], [20].

Lattice Parameter	InN	GaN
a (Å)	3.5377	3.1893
c (Å)	5.7037	5.1851

In the zincblende structure, a cubic unit cell has two atoms of indium and nitrogen as presented in figure 4b. The ZB structure unit cell holds only the a-lattice constant and contains two interpenetrating Face Centered Cubic (FCC) sublattices.

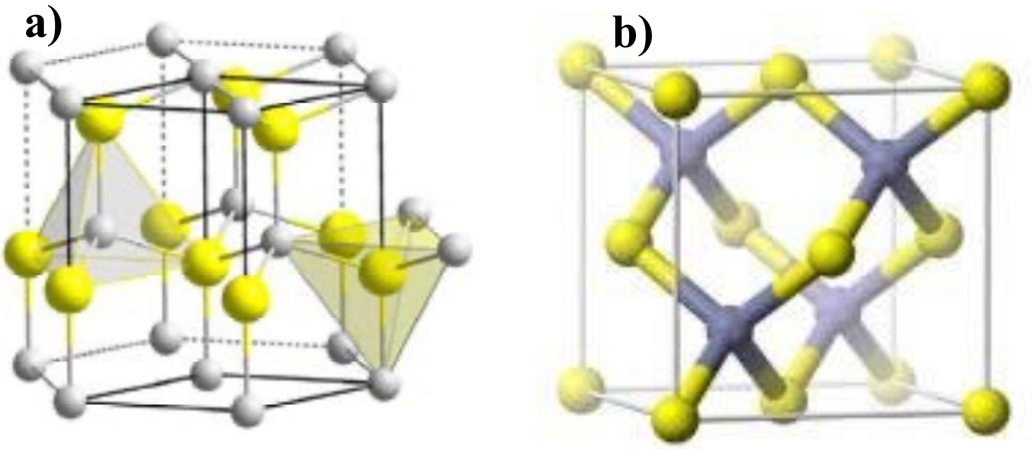

Figure 4: An illustration of the wurtzite lattice structure (a) and the zincblende lattice structure (b) of III-nitrides element with N atoms [21].

The hexagonal and cubic unit cells vary merely by the basal planes' stacking sequence, meaning that the bond angle of the second closest atoms and the number of atoms is different. The stacking classification for each wz structure unit cell is an ABABAB along the [0001] direction with a space group of P6mc (C4) [22]. However, the stacking sequence of each zb structure unit cell has an ABCABC of {111} close-packed planes with a space group of Td2

(F43m). The bond angle of the second closest atoms is 0° in a wz structure, so there is no in-plane variation along the [0001] direction. However, the bond angle of the second nearest neighbor in the zb structure is 60° in-plane rotation which causes a c-staking plane along the [111] direction [22]. The intrinsic asymmetry in the wz structure results in spontaneous polarization [23]. In addition, introducing external mechanical stress on the wz structure leads to piezoelectric polarization.

2.3.2 Growth Limitations

Generally, the wurtzite structure is opposed to most common III-V semiconductors, which are zinc blends like GaAs or diamond like Si. Obtaining suitable substrates that are lattice-matched with wurtzite GaN growth is one of the main challenges of growth. Currently, sapphire substrates are employed for growing wurtzite GaN. The substantial lattice and thermal mismatch found among GaN and sapphire and between InN and sapphire create several defects, which produce very high densities of dislocations. Alternative substrates used to grow wurtzite GaN are ZnO and SiC. These substrates provide enhanced lattice matching; however, they are significantly more expensive compared to the sapphire substrate [24], [25]. Forming a thick, relaxed GaN film on sapphire is usually performed in order to decrease the lattice mismatch among InN and sapphire. Even though InN has a much lower lattice mismatch, ~11%, with GaN than with sapphire, it is still sufficient to produce very high densities of dislocations in the growth of InN on GaN [25]. The device performance would be deteriorated due to these dislocations. Utilizing quantum dots can remarkably decrease the density of defects.

2.3.3 Quantum Dots of III-Nitride Materials

Semiconductor QDs have been widely investigated because of their potential for numerous optoelectronic device applications [26], [27]. QDs also have a high potential for scalability, either from self-assembly or novel top-down approaches. QDs of III-nitride materials have attracted much interest due to their unique electrical and optical properties arising from their zero-dimension quantum confinement effect and wide-bandgap ranging from 0.7 eV to 6.2 eV for InN and AlN, respectivlly [28], as well as their other unique properties such as strong exciton emission, high absorption coefficients, high-saturation velocities, and high radiation tolerance [29]. QDs in InGaN devices have resulted in high-efficiency luminescence even with a high density of dislocations [30]. They have also demonstrated utility in single-photon emitters or single-electron devices for quantum information applications [31]. Indium nitride (InN) can form QDs in a gallium nitride (GaN) matrix where the bulk band offset between the two materials creates a confinement energy of approximately 2.5 eV. This InN/GaN system may offer advantages of large confinements and scalability and long recombination lifetimes [32], as well as theoretically predicted topologically protected spin states [33] resulting from the large polarization fields inherent in the III-nitride semiconductor system.

2.4 The Basic Principle of Nanomaterial growth

2.4.1 Quantum Confinement Effects

For a better understanding of quantum confinement, it is critical to understand the bulk semiconductor materials. Bulk semiconductors are characterized via their band gap energy (E_g, as shown in figure 5. The band gap energy is the energy difference between the bottom of the conduction band and top of the valence bands. Fundamentally, it is the least energy needed to excite an electron from the ground state in a valence band into the conduction band [34]–[36] If an electron in the valence band gains sufficient energy to overcome the energy gap via absorption of a photon or thermal excitation, subsequently, the electrons leave a *hole* in the valence band. The attraction between the electron and hole and via the Coulomb force causes the creation of a bound state, called an “exciton” [35]. The Exciton has a typical physical separation between the electron and hole, identified as the exciton Bohr radius, which is different in each material. The Bohr radius can be in a range between 1 nm to more than 100 nm based on the material. In the bulk semiconductor materials, the energy levels of electrons remain continuous. If the exciton size is bigger than the dimension of a semiconductor nanocrystal, the electron becomes confined in all three spatial dimensions. It can be calculated by [37]:

$$a_0 = \frac{4\pi\varepsilon\varepsilon_0\hbar^2}{m^* q^2} \qquad \textit{Equation 1}$$

where ε is permittivity, and m^* reduced effective mass. These two parameters are related to the semiconductor materials. The ε_0 is relative permittivity, and $\hbar$ is Planck’s constant. In the bulk semiconductor materials, electrons and holes transfer freely in all directions and their energy levels remain continuous.

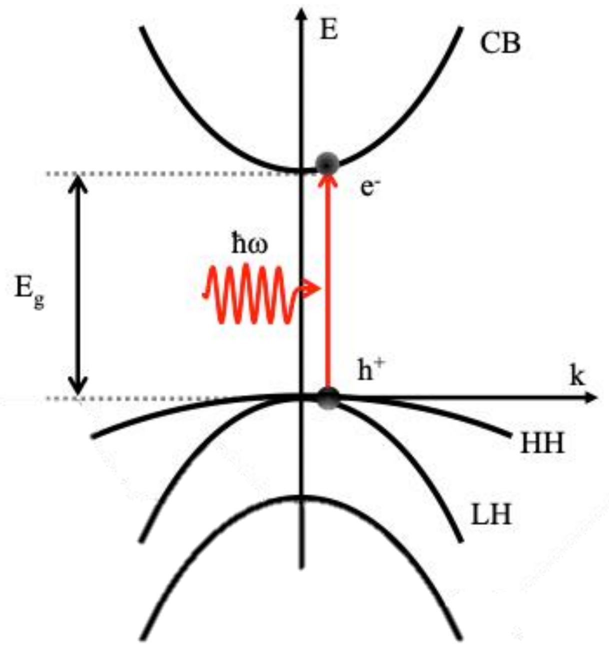

Figure 5: An illustration of a direct band gap semiconductor diagram.

When dimensions of the semiconductors are reduced to on the order of the Bohr radius, the electron wave functions become confined leading to discrete the energy levels. As a result, the local effective bandgap increases. This effect appears when the dimensions of the confining potential are decreased in one, two, or three directions of space to become equivalent or lower than the electrons or holes' Bohr radius [37], [38]. This effect is identified as *quantum confinement*. The quantum confinement effect has an impact on the optical, electrical, and mechanical properties of the nanomaterials.

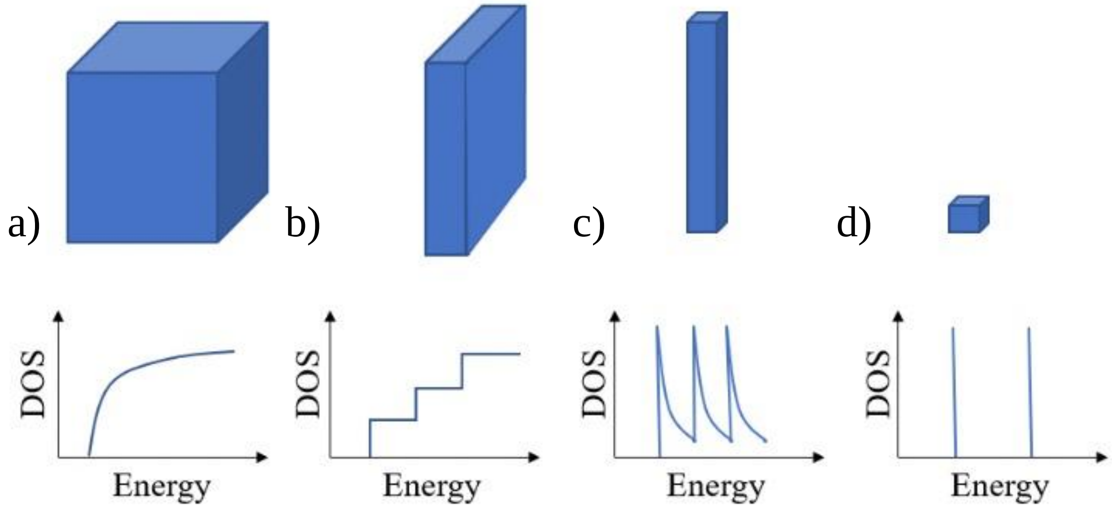

Figure 6: Schematic of quantum confinement effect on the density of states for: (a) a three-dimensional system or bulk, (b) a two-dimensional system or quantum well, (c) a one-dimension system or quantum wire, and (d) a zero-dimension system or quantum dot [39].

To understand how the small dimensional systems are classified, the charge carriers will be explained in term of confinement directions and the degree of freedom. In bulk semiconductor materials, the charge carriers are free to move in all three directions and have zero confinement. Thus, the bulk semiconductor materials are defined as *three-dimensional systems*. However, when reducing the size of the semiconductor in only one direction to a few nanometers, the charge carriers can still move freely in the other two direction. This kind of confinement is referee to as *a two-dimensional system or a quantum well*. When reducing the size of the materials in two directions, the charge carriers transfer freely merely in a single direction, which is called *a one-dimension system or quantum wire*. Finally, when the charge carriers are restricted in three-dimensions and have zero degree of freedom, the structure is termed as *a zero-dimension system or quantum dot* [34], [37]–[39]. Figure 6 presents the influence of the quantum confinement on the density of states. The focus here is mainly on the quantum dots.

Quantization of the charge carrier in all three dimensions changes the density of states. The density of states is defined by the quantity of confined states for charge carries to occupy at a given energy. Therefore, the charge carriers in low dimension systems can only occupy the separate energy levels. As mentioned earlier, the charge carrier in the quantum dot system is confined in all three dimensions and has zero degree of freedom in the particle's momentum. Therefore, this system can be defined as a particle in a three-dimensional (3D) potential quantum box (figure 7). Hence, the energy levels in a quantum dot are referred to as *sublevels*.

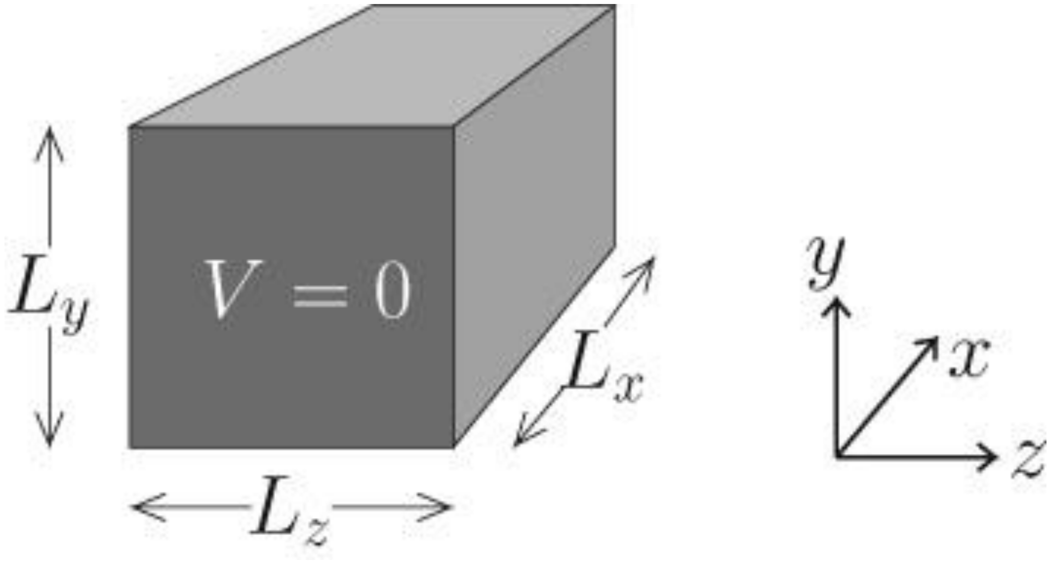

Figure 7: Schematic sketch of a three-dimensional quantum box with the dimensions: L_x, L_y, and L_z [40].

The three-dimensional Schrödinger equation in the box is defined [40]as:

$$-\frac{\hbar^2}{2m^*}\left(\frac{\partial^2}{\partial x^2}+\frac{\partial^2}{\partial y^2}+\frac{\partial^2}{\partial z^2}\right)\psi(x,y,z)=E_{x,y,z}\psi(x,y,z) \qquad \textit{Equation 2}$$

Writing the three-dimensional Schrödinger equation ($E_{x,y,z}$) as three one-dimensional equations E_x, E_y, and E_z.

$$-\frac{\hbar^2}{2m^*}\frac{\partial^2}{\partial x^2}\psi(x)=E_x\psi(x) \qquad \textit{Equation 3}$$

$$-\frac{\hbar^2}{2m^*}\frac{\partial^2}{\partial y^2}\psi(y)=E_y\psi(y) \qquad \textit{Equation 4}$$

$$-\frac{\hbar^2}{2m^*}\frac{\partial^2}{\partial z^2}\psi(z)=E_z\psi(z) \qquad \textit{Equation 5}$$

Considering the infinite barrier condition, the solutions to the Schrödinger equation are the same as in an infinite quantum potential well of widths: L_x, L_y, and L_z[37], [40]. When the energy interval is close to zero, the density of states defined as a sequence of gamma-functions positioned in the center of the confined energy levels [21] [37]. This energy levels are completely separate and are assumed to be [37]:

$$E_{n_x,n_y,n_z}=\frac{\pi\hbar^2}{2m^*}\left(\frac{n_x^2}{L_x^2}+\frac{n_y^2}{L_y^2}+\frac{n_z^2}{L_z^2}\right) \qquad \textit{Equation 6}$$

where m^* is reduced effective mass. (L_x, L_y, L_z) and (n_x, n_y, n_z) are the quantum dot's dimensions and positive integers, respectively [37].

2.4.2 Quantum Confined Stark Effect (QCSE)

Several aspects can affect the bulk semiconductors' bang gap. The band gap can be changed by applying a mechanical force such as temperature or stress on the semiconductor's materials. The most obvious effect in the III-nitride materials is the Stark effect. In this effect, when applying an electric field, the energy band structure is altered, leading to a variation in the optical and electrical properties. The III-nitride wurtzite materials possess both intrinsic and piezoelectric polarization fields, which can be produced by strain as a result of the lattice-mismatched growth of a thin InN layer on GaN [13].

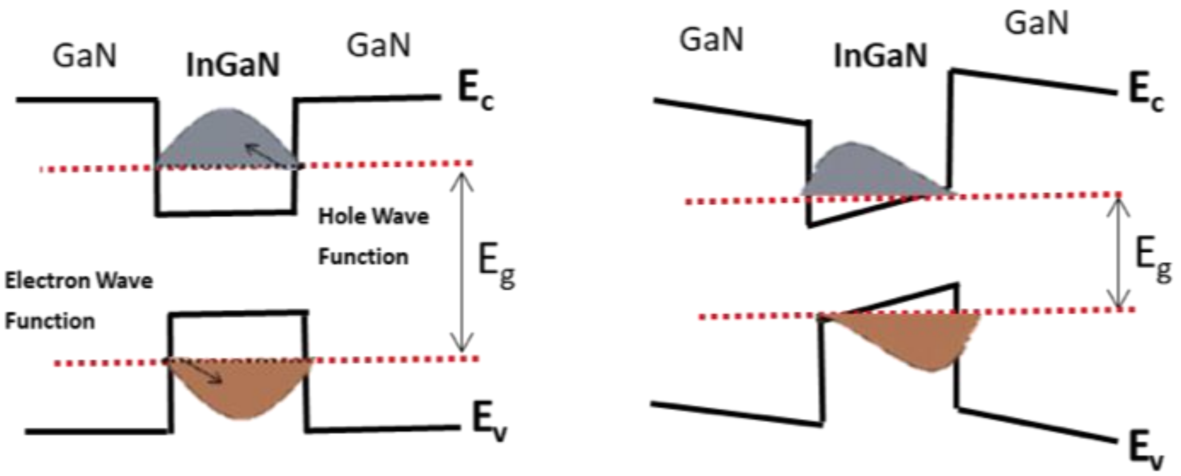

Figure 8: A schematic represents the band diagram of (a) the quantum well (b) the QCSE in InGaN/GaN.

The electric field in the III-nitride nanostructure causes the band edges to tilt, resulting in a separation of the electron and hole of the confined excitons, effectively extending their lifetimes owing to the Quantum Confined Stark Effect (QCSE), as presented in figure 8. This effect degrades optoelectrical devices such as LEDs. Nonetheless, this is considered an advantage to make this material promising for quantum computing applications since it extends the time to interact with the system. This internal polarization field in the materials is considered one aspect that can lead to a topological state. Generally, an extreme QCSE is required to achieve a topological state whereby the valence band maximum rises to meet the conduction band minimum leading to a band inversion. Besides the quite sizeable spin-orbit coupling in the indium nitride, this band inversion results in the topological states [5].

2.4.3 Growth of Quantum Dots

Since the first QD structures were achieved in the 1980s [41], several techniques for growing QD have been established. There exist top-down and bottom-up approaches for forming QDs. The top-down methods, including lithography [1], split-gate [2], colloidal chemical [3], and etching [4], can create QDs with the required size and location, but these methods are time-consuming and expensive. On the other hand, bottom-up techniques such as self-assembly epitaxial growth [5] can form QDs naturally, leading to high densities of QDs.

An epitaxial thin film's formation starts with semiconductor atoms in a vapor form impinging on the substrate, known as *nucleation.* When the growth continues, a group of atoms or clusters is formed, which is the basis of the quantum dots. This stage is called nucleus growth. Basically, the epitaxial growth begins by exposing the substrate to molecular beams in a vapor form leading to a uniform formation of small and extremely mobile clusters or 3D structures. During the nucleation stage, the incorporation of clusters leads to increase its size. Then, after some time of growth, the islands or clusters combine, creating liquid-like materials, known as wetting layer, mainly at high substrate temperatures leading to a lower density of islands. Continuing to grow or deposit more materials along with coalescence leads to connecting the cluster, generating unfilled channels which are filled by depositing more materials. As a result, thin films or two-dimensional structures are formed. A quantum dot growth can be made by stopping the deposition before completing the formation of the thin films to create clusters or 3D structures. The quantum dots in general have three degrees of confinement and a zero degree of freedom, meaning that the charge carriers are restricted in all directions [37]. The self-assembly technique can grow three modes of heteroepitaxial growth, shown in Figure 9, and they are:

1. Volmer-Weber growth mode (*Islands*)
2. Frank-van de Merwe mode (*Layered*)
3. Stranski–Krastanov (SK) mode (*layer plus island)*

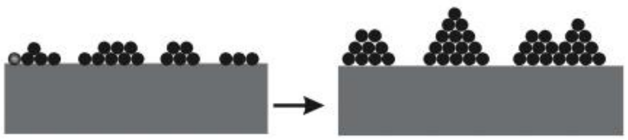

(a) Island (Volmer-Weber)

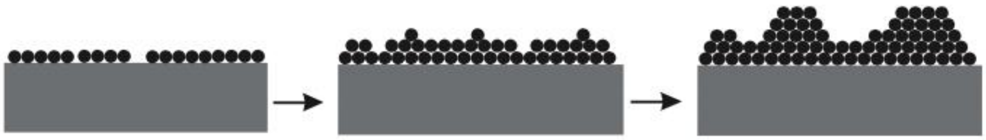

(b) Layer (Frank-van der Merwe)

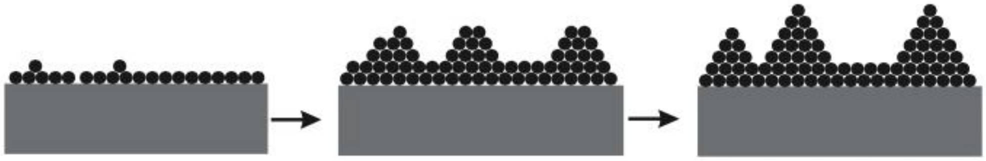

(c) Stranski – Krastanov

Figure 9**:** An illustration of the three heteroepitaxial growth modes [37].

Volmer-Weber growth mode is formed the island growth (quantum dots). In this mode, the islands' formations start by depositing tiny clusters which are nucleated on the surface of the substrate forming 3D structures. This mode occurs when bonding between the molecules are stronger than to the substrate. Frank-van de Merwe mode creates a two dimensions layer (thin films). The formation of the thin films occurs when the small clusters grow mainly in two dimensions. The bonding between the molecules and the substrate are more substantial than the bonding between the molecules. Stranski–Krastanov (SK) mode is identified as (*layer plus island)*, which is a mixing of the layer and island growth modes. Once a few monolayers were grown, the following layer growth gets unfavorable leading to island formation. The initial two or three monolayers deposition on the substrate's surface or the buffer layer's surface is known as the "*wetting layer*." The quantum dots in this mode are formed through strain build-up and relaxation resulting from the lattice mismatch [5] [6]. InN QDs have been successfully formed on GaN substrates with around ~11% of lattice mismatch using classical S-K growth [6], [7].

Moreover, many current researchers have reported InN QDs/GaN growth using molecular beam epitaxy (MBE) [47], [11], [49], [50]. Essentially, the quantum dots formed by S-K growth mode is possible to control to some degree via closely controlling the growth conditions such as growth rate and temperature [51]. However, the QDs resulting from this S-K growth mode has a relatively limited size range, forming naturally from the strain.

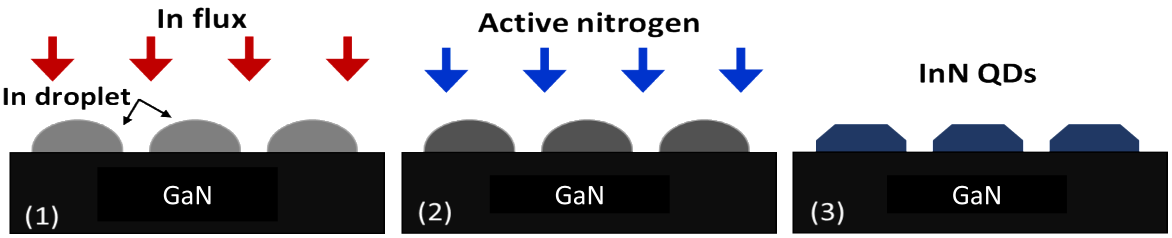

Figure 10**:** Schematic of the droplet epitaxy of InN QDs.

The droplet epitaxy (DE) growth technique, as presented in figure 10, has gained much attention for growing quantum dots and nanostructures of nitrides [48], [52], [53]. This approach starts by exposing the substrate to the group-III atoms, forming liquid droplets invoked on the Volmer–Weber growth model [54]. The droplets are then exposed to a group-V molecular beam to crystallize the droplets into QDs. The transition from droplets into QDs is known as "crystallization" or "nitridation" in the case of the III-nitride semiconductors. The DE method has many advantages over the S-K technique. One is that the crystallization of the QDs in the DE technique does not require the strain generated via the lattice mismatch as in the S-K method. Therefore, the growth of QDs in the DE technique can be done on either lattice-matched or mismatched substrates. In addition, in this method, a wide range of QD shapes and sizes can be controllably formed [55], [56], [57] as opposed to the strain-driven S-K method of forming self-assembled QDs. There is very little information on the growth of InN QDs by DE in the literature [58]. Therefore, more study is needed in order to begin to see a complete picture of the range of possibilities.

2.4.4 Nucleation

2.4.4.1 Surface Energy

A solid nucleates created from a previous unsteady vapor or liquid phase creating a solid-vapor or solid-liquid interface, respectively [59]. The energy at the interface between two phases and associated with the intermolecular forces is referred to as surface free energy. The atoms at free surfaces have a higher energy in comparison with atoms in a bulk. These variance in interatomic energy of atoms is the main source of the surface energy [59], [60].

The surface energy of a liquid is defined as surface tension which is the intermolecular attractive forces performed via liquid molecular to minimize its surface area [60] as figure 11. A liquid molecule at the surface makes less bond with the neighboring atoms than a molecule in the bulk of a liquid. This instability of intermolecular attractive forces or free bonds causes the surface tension of a liquid [59].

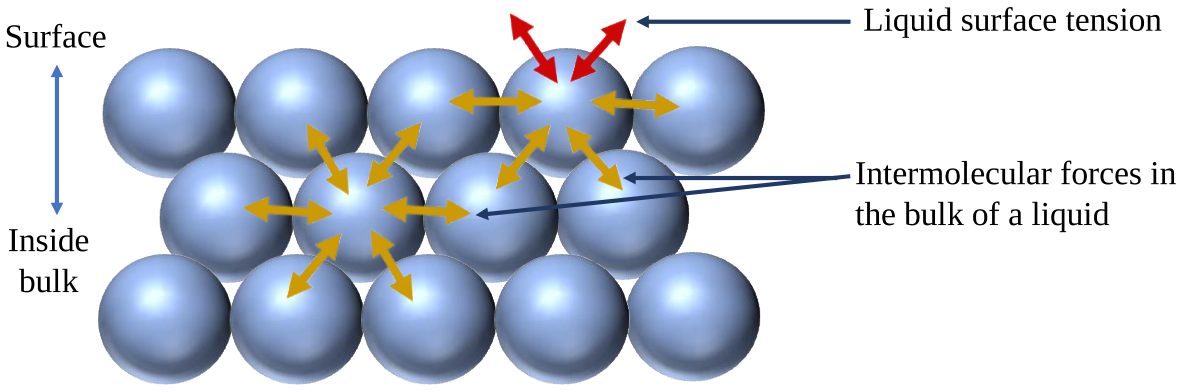

Figure 11: Schematic of the surface tension in a liquid.

The *interfacial surface energies* among a liquid and a solid surface can be described by the “*Young equation*” at equilibrium which is given by [37].

$$\gamma_{sv} = \gamma_{fs} + \gamma_{vf} \cos\theta, \qquad \text{Equation 7}$$

where θ is the contact angle, which is contingent on the surface characteristics of the semiconductor materials [37]. The γ_{sv}, γ_{fs}, and γ_{vf} are an interfacial tension among the substrate and the vapor, among the film and the substrate, and among the vapor and the film, respectively [37]. Depending on the surface energy of a solid and liquid, the liquid form as a sphere, droplet, or spread out as thin film on the solid surface, as presented in figure 12 [59]. When the surface energy of a liquid is higher than the surface energy of a solid substrate, the liquid tends to minimize its surface area leading to the formation of a spherical shape with around 180° contact angle with a solid surface [59]. Instead, if the surface energy of a liquid is low, the liquid tends to expand its surface area, and the contact angle between a liquid and a solid becomes close to zero. Therefore, the liquid is spread out on the surface, forming a thin film known as wetting [59]. The liquid droplet form once the contact angle is bigger than zero. In general, the contact angle value will differ for different liquids. As the surface energy of the solid reduces, the contact angle between a liquid and a solid goes up, leading to decrease wettability [60]. Apparently, the chemical nature of the solid and liquid as well as the substrate temperatures significantly influence a liquid wetting the solid substrate [59].

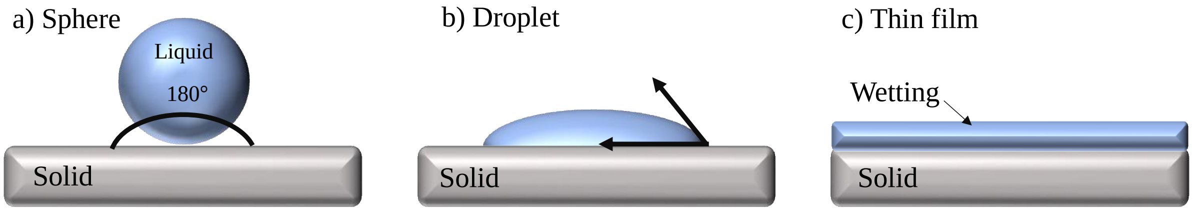

Figure 12: Schematic illustration of different liquid formations on a solid substrate.

2.4.4.2 Capillarity Theory of Nucleation

Capillarity theory is based on heterogeneous nucleation of an intensive layer on a substrate. It is very beneficial model to describe the semiconductor growth using the influences of variables including deposition rate, substrate temperature, and nucleus size [59]. It is assumed that the semiconductor atoms in a vapor phase impinge on the substrate generating nuclei. The change of the free energy associated with the generated nucleus of mean dimension r is given by [37]

$$\Delta G = a_3 r^3\, \Delta G_V + a_1 r^2 \gamma_{vf} + a_2 r^2 \gamma_{fs} - a_2 r^2 \gamma_{sv}, \qquad \textit{Equation 8}$$

where ΔG_V is the chemical free energy change per unit volume which drives the condensation reaction. The $a_3 r^3$ and $a_1 r^2$ are the volume and the curved surface area of the nucleus, respectively. The $a_2 r^2$ is the circular area of the nucleus on the substrate. The shape of the cluster or nucleus is presented in figure 13. The a_1, a_2, & a_3 are geometric constants [37].

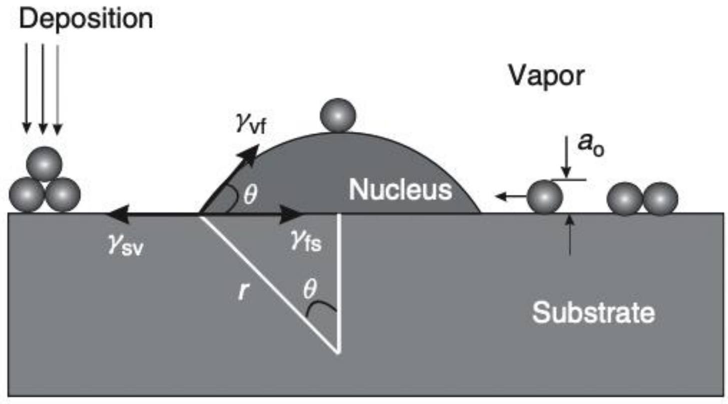

Figure 13: A graphic of the process of depositing vapor atoms on a substrate's surface [37].

Young's equation (equation 7) can be used to distinguish between the Volmer-Weber, Frank-van de Merwe, Stranski–Krastanov (SK) growth modes. First, Volmer-Weber growth mode in which the deposition of atoms on the surface forms an island, the contact angle with a surface (θ) is greater than zero, which can be written as [37].

$$\gamma_{sv} < \gamma_{fs} + \gamma_{vf}, \qquad \textit{Equation 9}$$

In case of Frank-van der Merwe growth mode or layer, the deposition of the vaper atoms wets the substrate. Therefore, the contact angle (θ) equals zero [37].

$$\gamma_{sv} = \gamma_{fs} + \gamma_{vf}, \qquad \textit{Equation 10}$$

In the Stranski–Krastanov (SK) growth mode, the strain energy per unit area of grown film is larger than the interfacial tension between film and vapor. This mode causes the quantum dots to form on the top of the wetting layer and this mode fulfills the inequality [37]

$$\gamma_{sv} > \gamma_{fs} + \gamma_{vf}, \qquad \textit{Equation 11}$$

When depositing vapor atoms on a solid substrate's surface, a new interface appears. As a result, the surface free energy increases, and the system energy is reduced, which appears as a damage of the solid and vapor interface below the nucleus formation. At thermodynamic equilibrium, the $\frac{d\Delta G}{dr} = 0$, which appears at critical radius $r^*$of a nucleus given by [59], [60]

$$r^* = \frac{-2\left(a_1\gamma_{vf} + a_2\gamma_{fs} - a_2\gamma_{sv}\right)}{3a_3\Delta G_V} \qquad \textit{Equation 12}$$

The difference in the energy barrier to nucleation ΔG^*, can be found at $r = r^*$ by [59]

$$\Delta G^* = \frac{4\left(a_1\gamma_{vf} + a_2\gamma_{fs} - a_2\gamma_{sv}\right)^3}{27a_3^2\Delta G_V^2} \qquad \textit{Equation 13}$$

An island with size smaller than r^* disappears through shrinking leading to reducing in the change of the free energy ΔG in the process. As depositing further vapor atoms, ΔG reduces even more. Through substituting the geometric constants in the equation 10, the change in the energy barrier ΔG^* becomes [59]

$$\Delta G^* = \left(\frac{16\pi\gamma_{vf}^3}{3\Delta G_V^2}\right)\left(\frac{2 - 3\cos\theta + \cos^3\theta}{4}\right) \qquad \textit{Equation 14}$$

The first factor of the equation is derived for homogeneous nucleation, and a second term is called a wetting factor which depends on the contact angle, θ [37]. Additionally, the change in the energy barrier (ΔG^*) has a strong impact on the density (N^*) of stable nuclei, which are expected to survive. At equilibrium, the number of nuclei of critical size per unit area on the substrate is assumed to be [59]

$$N^* = n_s e^{-\frac{\Delta G^*}{k_B T}} \qquad \textit{Equation 15}$$

where n_s is the total nucleation site density, and $k_B T$ is the Boltzmann constant and the temperature, respectively. In order to understand the influence of the substrate temperature and deposition rate on the energy barrier ΔG^*, the chemical free-energy change per unit volume, ΔG_V, can be written as [59]

$$\Delta G_V = -\frac{k_B T}{\Omega} ln\left(\frac{\dot{R}}{\dot{R}_e}\right) \qquad \textit{Equation 16}$$

where $\dot{R}$ is the deposition rate, and $\dot{R}_e$ is the equilibrium evaporation rate from the film nucleus at the substrate temperature [59]. By a direct differentiation of r^* equation 12 and assuming typical values for the interfacial tension between the vapor and the film and an entropy change for vaporization, four inequalities can be given by[59]

$$\left(\frac{\partial r^*}{\partial T}\right)_{\dot{R}} > 0 \qquad \textit{Equation 17}$$

$$\left(\frac{\partial \Delta G^*}{\partial T}\right)_{\dot{R}} > 0 \qquad \textit{Equation 18}$$

$$\left(\frac{\partial r^*}{\partial \dot{R}}\right)_{T} < 0 \qquad \textit{Equation 19}$$

$$\left(\frac{\partial \Delta G^*}{\partial \dot{R}}\right)_{T} < 0 \qquad \textit{Equation 20}$$

These four inequalities summarize several common influences observed during film deposition. Equations 17 and 18 show that a superior substrate temperature causes a rise in the critical radius of a nucleus and a nucleation barrier at a fixed deposition rate. Additionally, Equations 19 and 20 present that a high deposition rate reduces the critical radius of the nucleus (smaller islands) and a nucleation barrier at a constant substrate temperature. Finally, the number of nuclei declines rapidly with temperature since it is exponentially dependent on the nucleation barrier [59].

2.4.4.3 Cluster Coalescence

As mentioned in the prior section, the density of stable nuclei decreases with temperature. Additionally, depending on the kinetic models, coalescence phenomena cause the density of stabilized clusters to increase with the growth time up to some extreme level before decreasing. The main features defining the coalescence process include that reducing the sum of the clusters' number and rising the height of remaining clusters.

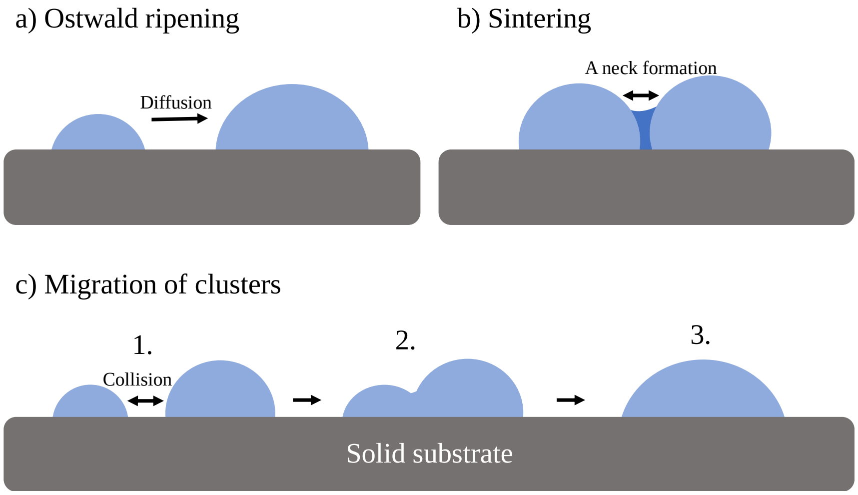

Figure 14: Coalescence of clusters as a result of a) Ostwald ripening, b) Sintering, and c) migration.

As vapor atoms are deposited on the surface of the substrate, the cluster forms in various sizes. With time, the cluster with a larger size tends to grow or ripen using the smaller dots in a process known as the "ripening effect." The desire of an island structure to minimize its surface-free energy leads to a coalescence of clusters. The coalescence of clusters occurs due to three different mechanisms.

The first one is called *Ostwald ripening*, figure 14 (a), where the atoms in a smaller cluster diffuse to a larger cluster causing the small cluster to shrink until they disappear. This diffusion takes place without having direct contact between the clusters. *Sintering* is the second mechanism of the coalescence process, as presented in figure 14 (b). Here, the clusters or islands are connected where a neck is created among clusters, and this neck or channel thickens when atoms are transferred to the channel connecting the two clusters. The final mechanism is *a migration of clusters* on a solid substrate’s surface, figure 14 (c). The collisions between individual clusters or islands (droplets) when they perform a random motion result in the appearance of coalescence.

Chapter 3: Indium Nitride Quantum Dots Growth and Characterizations Techniques

This chapter describes the experimental techniques utilized in this work. First, the principles of molecular beam epitaxy (MBE) which is the epitaxial procedure used for In droplets and InN QD growth will be described. Subsequently, a brief explanation of the material characterization techniques used to characterize uniformity, size distribution, surface morphology, and density of the droplets and QDs. The sample growth and characterization of this research were accomplished by the author.

3.1 Molecular Beam Epitaxy

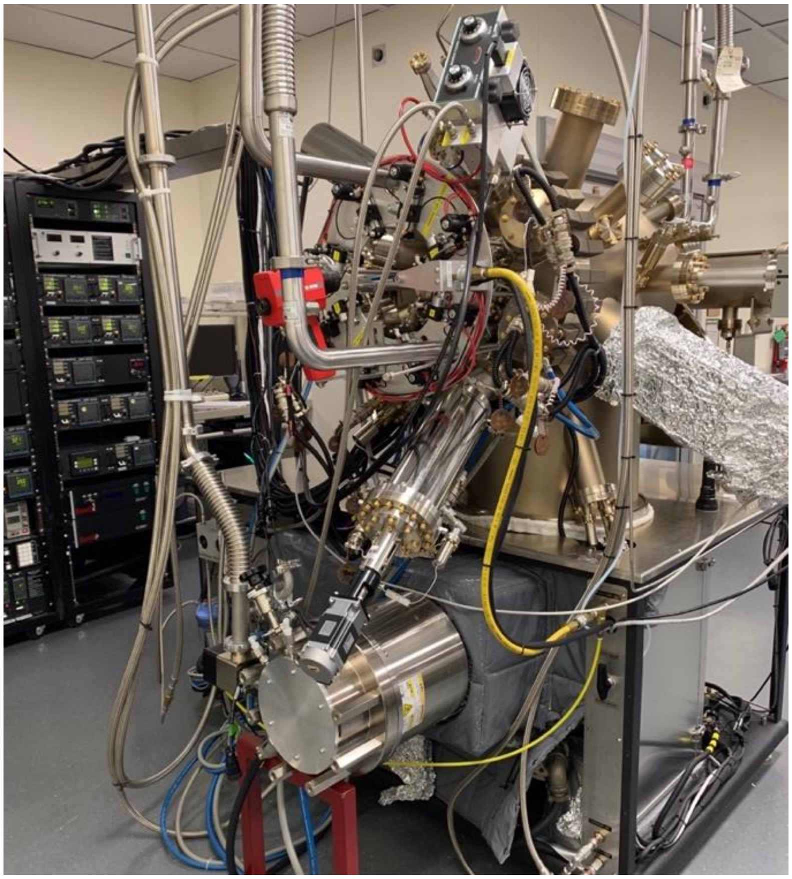

Figure 15: GEN II Molecular Beam Epitaxy.

(MBE) is one of the most extensively utilized systems for growing high-quality crystalline semiconductor materials with various structures ranging from thin film to quantum dots and nanomaterials [61], [62]. All samples in this work were formed using a GEN II plasma-assisted Molecular Beam Epitaxy (PAMBE) system. This is presented in figure 15. The GEN II MBE contains three connected vacuum chambers: growth chamber, Load-Lock (LL) chamber, and buffer chamber. Each chamber is isolated from the adjacent chamber via a gate valve and has each its own pumping system. The LL and buffer chambers are sequentially connected for wafer preparation and prevent any possible contaminants from entering the growth chamber.

The wafer is first loaded or unloaded onto the LL or entry chamber. This LL chamber will pump to high-vacuum levels and preform the initial outgas, which uses thermal energy to heat the chamber background to a temperature of 100-150 ℃. The purpose of the initial outgas is to remove water vapors and other volatile contaminants that might have entered the chamber when the chamber was subjected to the atmosphere. The heated station in the buffer chamber performs a pre-growth outgassing of an individual wafer up to 600-650 ℃ to remove any oxidation from the substrate. The wafer transferred between the LL chamber and the prep or buffer chamber via a trolley manually controlled with an exterior magnet, and it can be transferred from the trolley to heater station in the buffer chamber or to substrate heater in the growth chamber with magnetic-coupled transfer rods.

The growth chamber contains different Veeco effusion cells. The solid material sources are indium, gallium, silicon, magnesium, and aluminum. Active nitrogen is introduced via a Veeco UNI-Bulb radio frequency (RF) plasma source, which is utilized as “an atomic nitrogen source.” The nitrogen molecules are resonantly excited and separated through RF electromagnetic wave. The effusion cells in the GEN II MBE are oriented downward or upward regarding the substrate in the growth chamber. The growth of an epitaxial film is performed in the growth chamber by depositing thermal energy molecular or atom beams produced via heating a solid source effusion cells to the point of evaporation forming an evaporative flux directed to a heated surface of the substrate under Ultra-High Vacuum (UHV) (~$10^{-10} - 10^{-11}$ Torr) conditions[61]. Figure 16 shows an illustration of the PAMBE system. This UHV is accomplished through using several pumps and cooling systems. The growth chamber has turbo pump, roughing pump, cryo pump, and titanium sublimation pump, which all operate simultaneously.

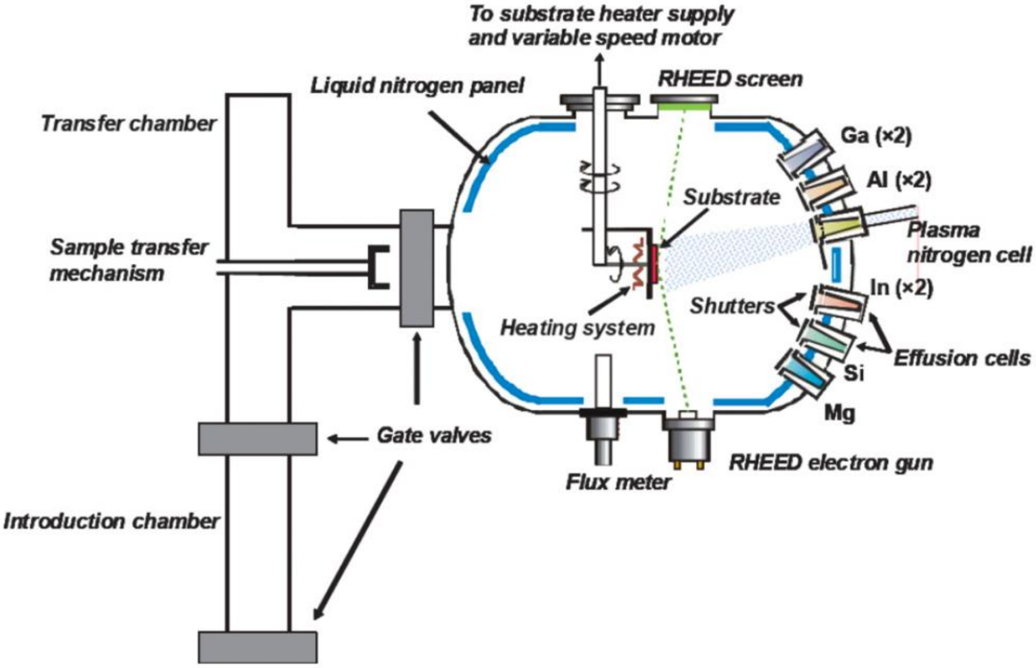

Figure 16: Schematic illustration of the PAMBE growth chamber [63].

Additionally, the cooling system is represented by a shroud around the growth chamber filled with liquid nitrogen. Therefore, the interior walls of the growth chamber are cooled down via the liquid nitrogen leading to attaching the molecules to the wall and decreasing the vacuum. This UHV is the main advantage to the MBE due to the extremely low contamination environment and ability to insert *in situ* tools into the system, including Reflection high-energy electron diffraction (RHEED) in order to monitoring the growth of the epitaxial film. The control of composition and thickness of the grown film is accomplished through the pause of the atoms beams via shutters placed between the materials' source and the substrate. The beam flux, a function of the vapor pressure, could be manipulated via programming the furnace temperature of the source [61]. The growth rate is usually around a monolayer formation per second. For the experiments, the growth rate is ≈ 1.5 ML/s (177 nm/h). Thus, 1 ML corresponds to ≈ 0.25 nm.

3.2 In situ real-time material characterization RHEED

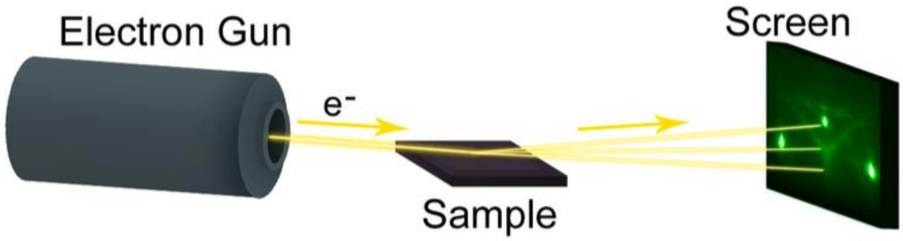

Figure 17: Sketch of the RHEED setup inside the MBE chamber [64].

One of the primary *in situ* real-time material characterizations in an MBE system is reflection high energy electron diffraction (RHEED), which is utilized to examine surface morphology, crystal structure, growth rate, and growth mode [64]. The RHEED system contains an electron gun and a phosphorous or fluorescent screen, which are installed in the growth chamber 180° distant from each other and aligned with the substrate [61]. A schematic of the RHEED design is presented in Figure 17. The RHEED utilized an electron gun to emit an electron beam with energy of 10-50 keV on substrate's surface at a grazing angle of ~1°, so it is merely diffracted via the initial atomic planes under the surface of the growing surface on the sample [61][64]. The scattering beam from the crystalline surface leads to the manifestation of intensity-modulated streaks in the case of 2D growth on a phosphorous or fluorescent screen, so the image exhibited on the screen is the Fourier transform of the interacting between the lattice of grown material with the beam.

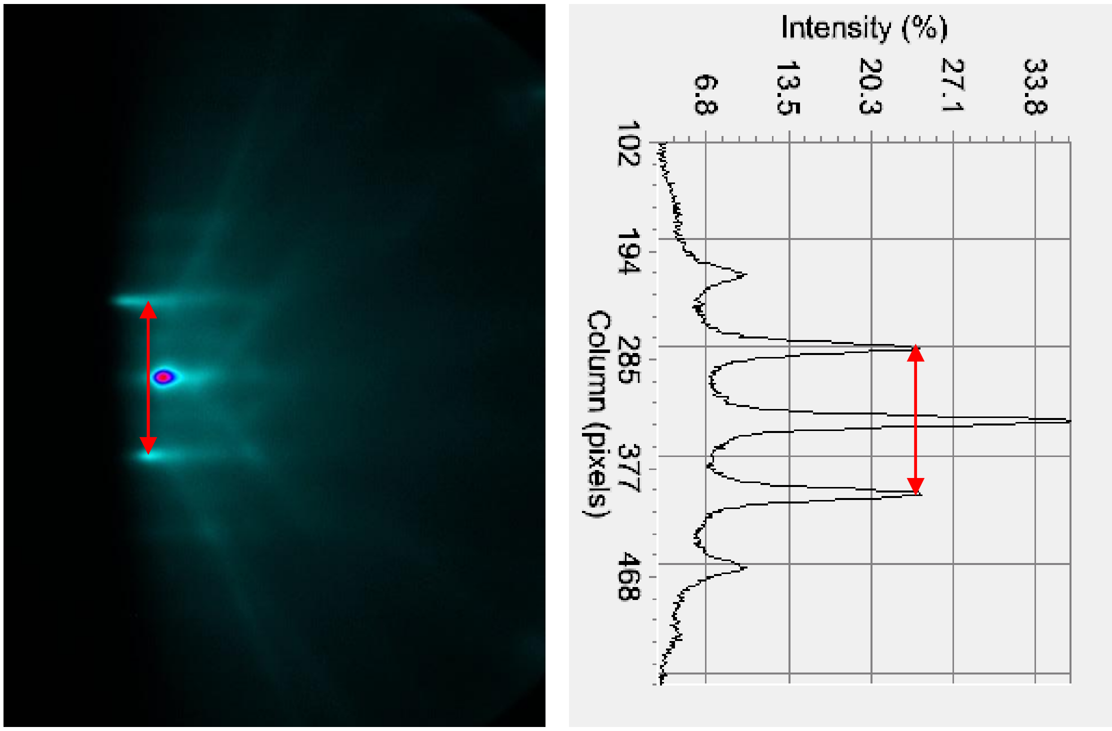

Figure 18: An illustration of the streaky RHEED pattern of a plane GaN surface and the intensity profile.

The basic principle of RHEED is the diffraction of electrons through a lattice plane. If an incoming electron beam defined by a wave vector $\overrightarrow{k_i}$ and the outgoing diffracted electron bean is described by wave vector $\overrightarrow{k_0}$. The diffraction condition can be given by [65][64]:

$$\overrightarrow{k_i} - \overrightarrow{k_0} = \overrightarrow{r^*}$$

Equation 21

where $\overrightarrow{r^*}$ is a surface's reciprocal vector. The diffraction conditions can also be visualized by Ewald construction. The Ewald sphere is the sphere with radius k_0. As this sphere crosses through the reciprocal lattice, the variance between the incident vector and outgoing diffracted vector is a reciprocal vector. As a result of this constructive interference, a pattern will be produced on the fluorescent screen. As the RHEED pattern represents the mutual space of a lattice plane, the distance among the rods, produced from the actual surface's roughness, is inversely proportional to the spacing among the atoms [65]. Therefore, the diffraction lines in reciprocal space are observed instead of diffraction spots. The in-plane lattice parameter can be obtained using the RHEED pattern via using the intensity profile to measure the distance between outside streaks, as seen in figure 18. In the case of 3D structures, the electron beam is transmitted through the QDs because the angle among the electron beam and the surface is quite small. Therefore, the electron beam becomes a transmission pattern resulting in a diffraction pattern which contains of a range of the transmission spots [64].

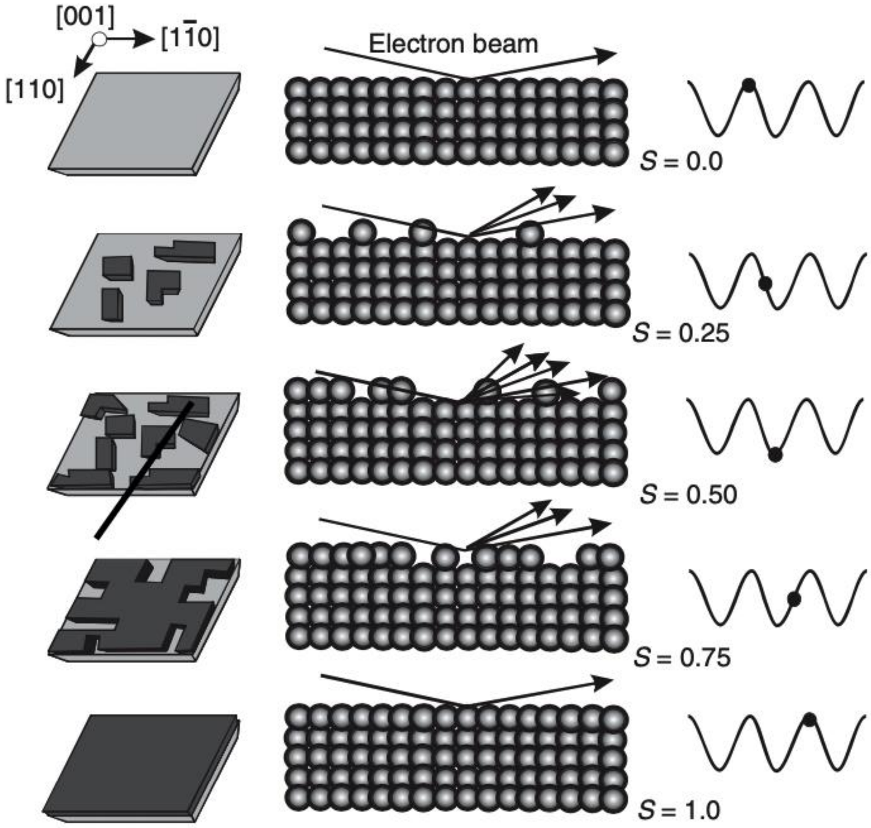

Figure 19: Schematic illustration of intensity oscillation of a monolayer growth as presented via RHEED [37].

RHEED can be used to monitor epitaxial growth and to measure the growth rate through intensity oscillations. Additionally, dynamic, or static mode can describe the patterns on the phosphorous screen [64]. The dynamic mode is depending on a variation in the intensity of the diffracted patterns resulting from the surface roughness variation over time during growth. When an atomic film is deposited on the surface, the surface roughness increases causing a variation in the intensity of the diffracted patterns. During a continuous growth, the surface roughness changes resulting in a transformation of the intensity of the diffraction streak. The growth of one monolayer is exhibited in Figure 19. Fractional coverage of a monolayer is referred to by (S). The surface roughness increases upon depositing atoms on an atomically smooth surface. When the atomic layer covers 50% of the surface, S = 0.5, the roughness of the surface achieves its maximum, and then it reduces until the growth of a monolayer is finished, which is again considered the minimum surface roughness at S = 1.0. The period of the intensity oscillations is equivalent to the time required to deposit a completed monolayer, and the maximum intensity indicates the minimum roughness [37].

In a static mode, the surface's atomic structure can be defined from the diffraction patterns of RHEED, which provide data on the surface's atomic structure. Therefore, if the RHEED patterns are streaky, it indicates a 2D growth, while a spotty pattern shows a 3D growth. This atomic structure is affected by the electron beam flux, the substrate temperature, and the strain of the formed film [64].

3.3 Structural Characterization Techniques

A brief explanation of the materials characterization techniques used to characterize uniformity, size distribution, density, and surface morphology of the droplets and InN QDs, including Atomic Force Microscope (AFM) and Scanning Electron Microscope (SEM) procedures, will be covered. Energy Dispersive X-Ray (EDX) will also be applied for the InN QDs material classification. Further, X-Ray Diffraction will be described to optimize the material imperfections and ensure high-quality crystal structures of the self-assembled In droplets and InN QDs.

3.3.1 Atomic Force Microscopy

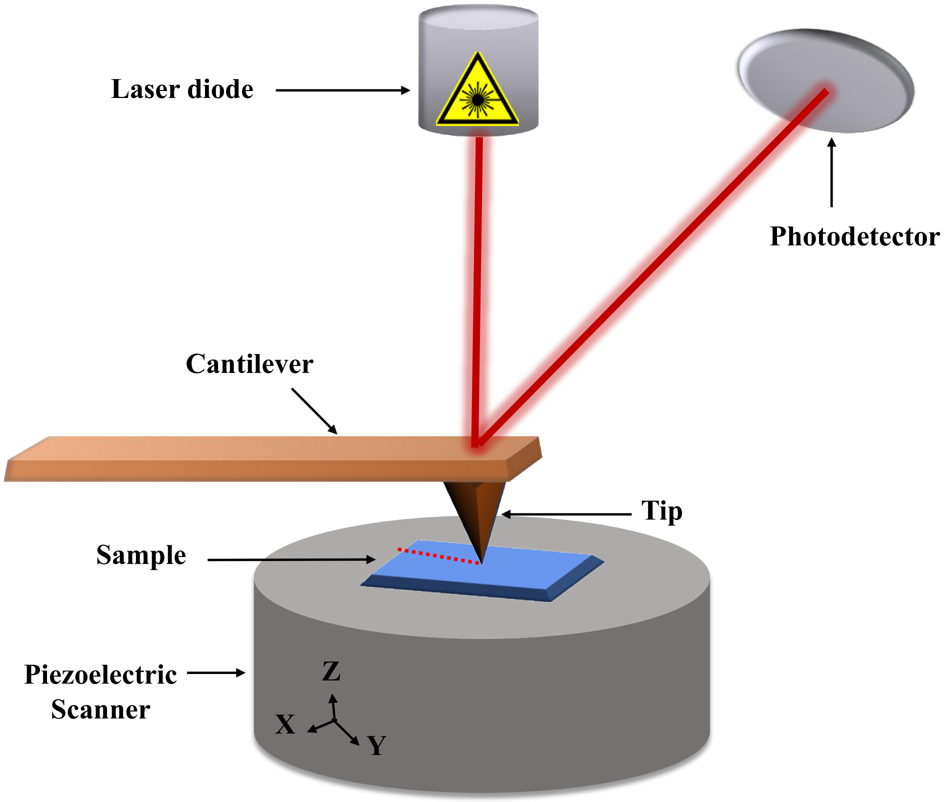

Figure 20: Schematic illustration of the AFM system.

Atomic force microscopy (AFM) is an imaging system mainly utilized to investigate any surface structure for various materials at the nanoscale. Still, it also can be applied to measure electrical and physical properties [66]. The working principle of AFM measures the interaction force among the surface of the sample and a tip. A very sharp tip with ~100 to 200 microns length is placed on a cantilever to scan an area of interest on the surface [67]. A piezoelectric tube scanner is utilized to control its motion. When this tip comes in contact with the surface of the sample, the interaction forces between the sample’s surface and the tip cause a deflection of the cantilever, which is sensed via an optical system in which a laser beam is directed toward the backside of the cantilever. When the cantilever is deflected, the laser beam is reflected and hits the center of the photodiode. A laser beam and a photodetector detect the cantilever's bending.

The photodetector detects a reflected laser beam from the cantilever. As a result, an ultra-high-resolution image of the scanned area is produced [67]. An illustration of the AFM work principle is presented in Figure 20.

The AFM has several imaging modes, including non-contact, contact, and tapping modes [66]. The tip is forced into the surface in the contact mode. As surface topography changes, the tip and the sample interaction result in cantilever deflection. The tip-sample surface interaction force is monitored via an electronic feedback loop to maintain the deflection constant during the scan. The contact mode is applied to measure a flat and not easily damaged surface morphology by dipole-dipole, van der Waals, and electrostatic interactions [66], [67]. In addition, the non-contact mode has some restrictions when dealing with a liquid film. Tapping mode is the most common mode used to examine the surface's topography. It involves an oscillating cantilever. This oscillation is near the resonant frequency of the cantilever. Here, the tip is in intermittent contact with the sample's surface, leading to substantially less damage to the surface, and a piezoelectric actuator maintains the tip and surface contact through its oscillation. The tapping mode has been employed to study the quantum dot's size, density, shape, and volume [66], [67], and it is the primary mode utilized in this work.

3.3.2 Scanning Electron Microscopy

Scanning electron microscopy (SEM) is another structural characterization procedure used to investigate physical dimensions of nanostructures, such as uniformity, size distribution, and surface morphology. SEM usages high-energy electrons beams to create high-resolution images of the surface of a sample, with 100.000 times magnification and detecting details in the range of nanometers [67], [68].

Here, the working principle of the SEM system is explained. Electrons in the SEM produced through a thermionic or field emission at the top of the microscopic column. Figure 21 demonstrates a sketch of the Scanning Electron Microscope column. A positively charged anode plate attracts generated electrons from the hot cathode. Therefore, the electrons accelerate to an anode. These electrons are then focused into a very narrow beam through a series of magnetic condenser lenses, which determine the beam size and the number of electrons in the beam. The size of the beam is possible to be controlled via apertures, and the beam size can control the resolution of the final image. The beam operates under a vacuum to avoid the interaction between the molecules already in the system and the electron beam. Then, coils deflect the beam over the sample surface. Once this high energy electron beam hits the atoms on the surface, the interactions between the beam and surface produce auger electrons, secondary electrons, back-scattered electrons, heat and x-rays [68]. A detector then detects these various emissions, generating a high-resolution image demonstrated on a computer screen. SEM can also be used to determine different layer thicknesses in a sample via tilting the sample.

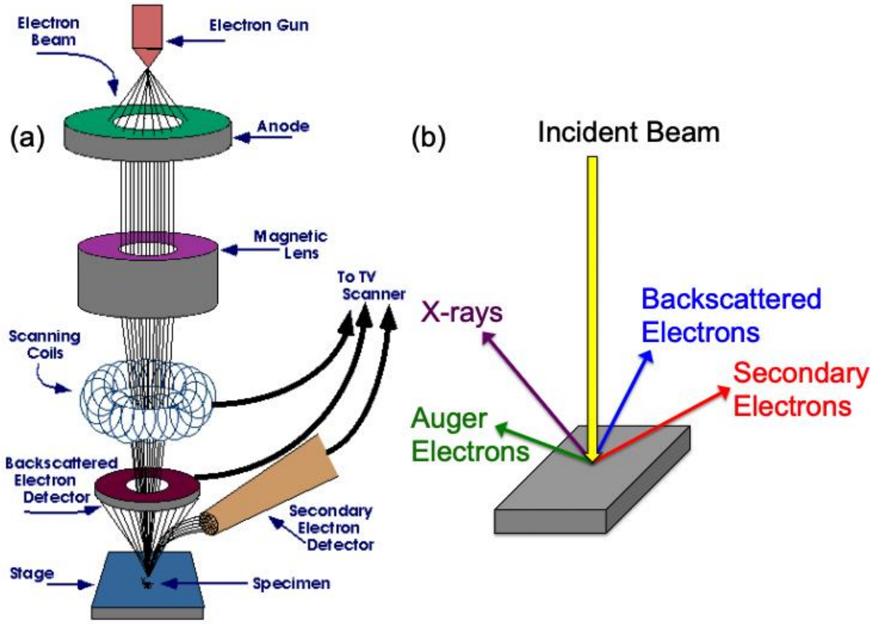

Figure 21: (a) A sketch of the Scanning Electron Microscope column, and (b) the interactions among the electrons beam and the sample’s surface [69].

Energy Dispersive X-ray Spectroscopy (EDX) is associated with a computer-based multi-channel analyzer (MCA) and delivers a valuable analytical facility in the SEM [68]. EDX has utilized the X-ray to define the chemical composition of each element that occurs on the surface as well as its concentration. As mentioned above in the SEM, as a high-energy electron beam reached the surface, it ejects an electron from an atom. The atom becomes ionized and captures a high-energy electron in the outer shell to return to its ground state. The energy difference resulting from the shell transition is emitted as an X-ray. Each semiconductor element produces a unique energy of X-ray. The detector will sense the emitted X-ray and use it to identify the chemical composition of each semiconductor element. An illustration of the EDX wavelength spectrum data is presented in figure 22.

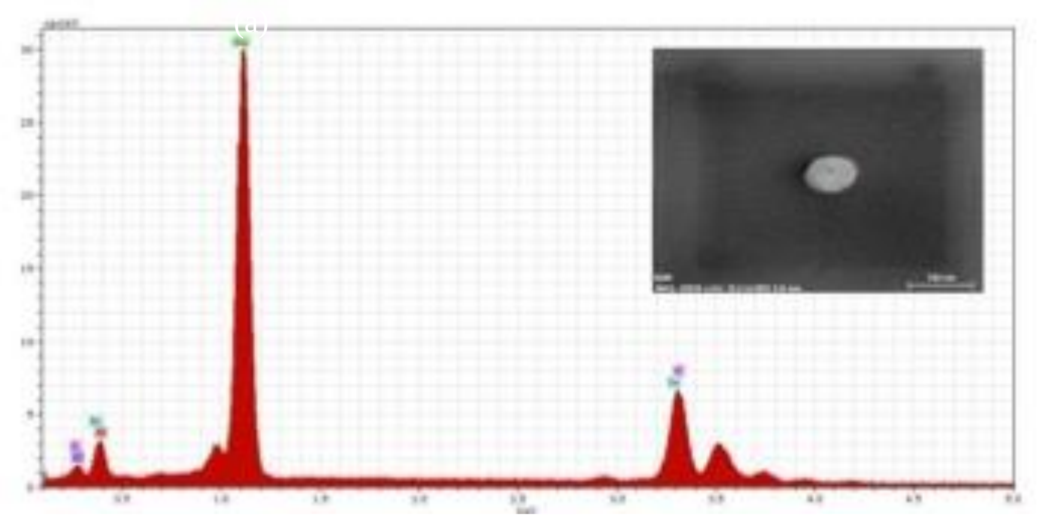

Figure 22: An illustration of Energy Dispersive X-ray Spectroscopy spectrum presenting the chemical composition of each element and an inserted SEM image.

3.3.3 X-ray Diffraction

X-ray diffraction (XRD) is a very effective instrument for characterizing the material’s crystalline structure. The x-ray was discovered in 1895, and the first XRD data acquired was of rock salt in 1911 [70]. There are two types of diffraction procedures: powder and single-crystal diffractions. The powder diffraction technique is utilized to investigate the scattered intensity of a sample with several phases and define the crystal orientation. On the other hand, the single-crystal diffraction process is applied to explore the crystal structure of organic and inorganic lattice plans and even biological compounds [70].

The central concept of XRD is diffractive scattering, which results from the interaction between incoming waves with non-uniformities in a medium [70]. An obvious illustration of scattering is the rainbow generated due to the interaction between light with water droplets after rain. Scattering can be elastic and inelastic. In elastic scattering, the kinetic energy of both particles does not change when they collide. However, in inelastic scattering, during the collision, some of the kinetic energy might get lost or gained by another particle resulting in a change in the kinetic energy of both particles.

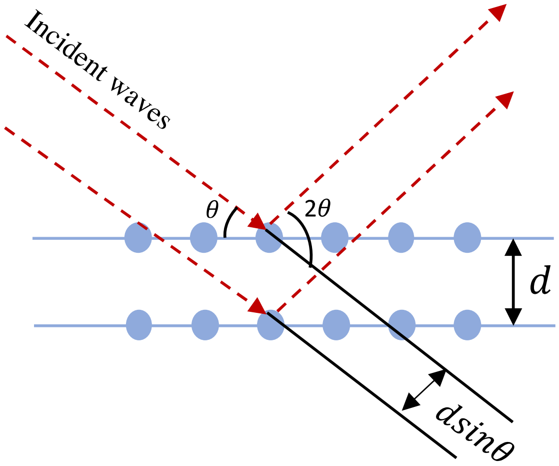

Figure 23: Schematic sketch for the Bragg condition.

Generally, X-rays are defined as electromagnetic waves with short wavelengths. The x-rays with wavelengths ranging from 0.5 ~ 2.5 nm, equivalent to the distance between atoms in crystals, are utilized in the diffraction procedure [71]–[73]. Basically, the interaction between the incoming x-rays with an electron in the crystal causes a re-emission of the x-ray with the identical energy, which interferes with each other when leaving the crystal. When x-rays are coherently scattered through the atoms, the interference of the x-rays results in peaks at particular positions, which can be described through Bragg's Law [70],

$$n\lambda = 2d\ sin\theta \qquad \textit{Equation 22}$$

where n is an integer indicating the diffraction order, λ, θ, and d, are the x-ray wavelength, angle between the incident x-ray and the surface, and the distances of the diffracting planes, respectively. The condition for Bragg's Law is presented in Figure 23.

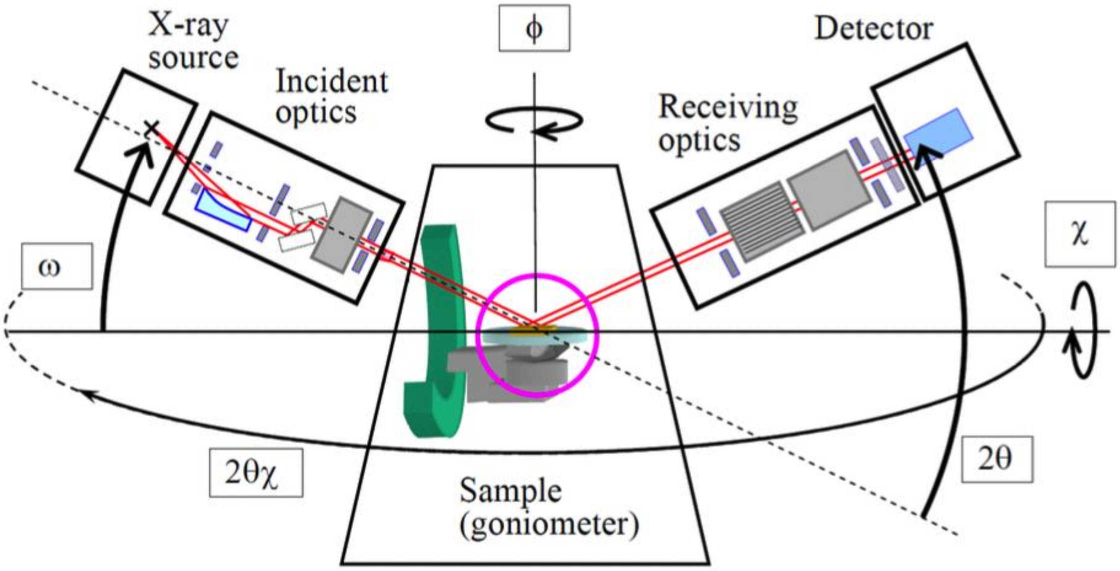

Figure 24: An illustration schematic of the XRD system [73].

This research uses a Philips X'pert MRD system to investigate the In droplets and the crystalized InN quantum dots. Figure 24 illustrates the typical schematic sketch of an XRD system. The X-rays are produced in an x-ray tube through bombarding a metal anode with a high-energy electron beam. The generated x-ray beam is emitted toward the conditioner in order to monochromate and collimate the beam. Subsequently, the beam is emitted toward the sample on the holder. The orientation of the sample holder can be changed, and it can be rotated along four angles $(\omega, 2\theta, \chi\ \phi,)$ [73]. The ω is the angle between the incident beam and the sample, and

2θ is the angle between the incident beam and outgoing beam. The angle χ is for the rotation around the x-axis, and ϕ is the angle used to rotate around the y-axis. This goniometer assists in choosing the plane family of materials. Using this goniometer, 2θ, ω, and $\omega - 2\theta$ scans can be measured for individual reflection. Furthermore, through changing both 2θ and ω, a two-dimensional scan around the reflection can be taken. Finally, a detector is utilized to detect of the x-rays. The sensor also has the ability to rotate while scanning.

3.4 Opticale Characterization Techniques

3.4.1 Raman spectroscopy

Raman spectroscopy delivers essential information about the material's crystal lattice, phonon frequencies, the energy of vibrational transitions, defects, and strain [74]. The interaction of incident monochromatic light with electrons in a material results in scattering radiation either elastically or inelastically [75]. When a photon of the incident light interacts with an electron in a material, the electron gains sufficient energy to rise to the upper vibrational energy state. When this electron falls back to its initial ground energy state, the electron releases its energy as a photon. In the case of elastic scattering, the energy of incident and released photons are equal, also named Rayleigh scattering. However, Raman spectroscopy is inelastic scattering where the energy of an incident and scattered photon differs. Raman scattering can be Stokes and anti-Stokes scattering, relying on the molecule's vibrational energy in the ground state [75]. In the Stokes scattering, the electron drops to an energy level higher than its ground state, resulting in a scattering photon with a longer wavelength and lower energy than the incident photon. However, when an electron falls to an energy level lower than its ground state, the scattered electron will have a shorter wavelength and higher energy than the incident photon in an anti-stokes scattering.

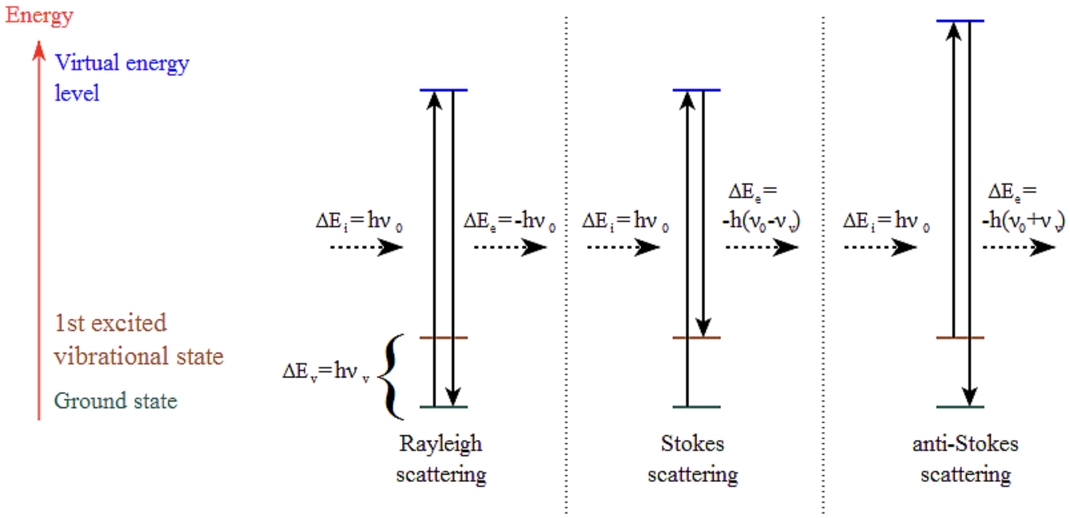

Figure 25: An illustration of Stokes, anti-Stokes, and Rayleigh scattering procedures [76].

Figure 25 shows the scattering procedures of Stokes, anti-Stokes, and Rayleigh scattering procedures. The different scattering energy from the incident photon energy is related to the vibration between ground states. Thus, the Raman spectra response of the Stokes and anti-Stokes occur during the vibrational energies, and it mostly appears as a shift from the Rayleigh scattering. The Raman transition possesses selection rules in which molecular polarizability must vary through the vibration, which is also matched with symmetry [77]. The most significant components of Raman spectroscopy are a light source with energy more considerable than the bandgap, an optical filter to exclude the elastic scattering photons, and a spectrometer to collect the scattered photons. Raman can be accomplished at atmospheric pressure and room temperature.

3.4.2 Photoluminescence

The fundamental idea of luminescence occurs if an electron in the valence band gains adequate energy to overcome the bandgap via many mechanisms, including a current injection, thermal excitation, or optical excitation, and transfers into the conduction band, leaving an orbital hole in the valence band. Once this excited electron returns to equilibrium, it will release its extra energy either as a photon if radiatively recombined with a hole or as phonons if non-radiatively recombined [78]. Based on the used excitation sources, there are several types of luminescence, such as cathodoluminescence, electroluminescence, and photoluminescence. Photoluminescence spectroscopy is the most widely utilized technique to investigate optical properties of semiconductors.

In photoluminescence (PL), a laser of photons with energy higher than the bandgap of the semiconductor is utilized as an excitation source. The absorption of photons results in exciting electrons to an upper energy state in a process called photoexcitation. When the excited electrons return to a lower energy state, it causes an emission of photons with energy equivalent to bandgap energy [78].

Chapter 4: Controlling the Density and Size of InN QDs formed on Sapphire Substrate via Droplet Epitaxy

4.1 Introduction

Due to the complicated growth parameters required for most III-nitride semiconductor materials, there has been great emphasis on achieving high crystal quality material in recent years. The crystal structure of the more commonly used III-nitride semiconductors is wurtzite instead of zinc blend and diamond like the most common III-V semiconductors like GaAs or Si. One of the main challenges is obtaining suitable substrates that are lattice-matched with wurtzite III-nitride growth. Currently, sapphire substrates are widely employed for growing wurtzite GaN, employing long complicated buffer growths in order to accomplish a high-quality surface for growth [79]. The substantial lattice and thermal mismatch between GaN and sapphire as well as between InN and sapphire create severe defects and high densities of dislocations. Alternative substrates used to grow wurtzite GaN are ZnO and SiC. These substrates provide enhanced lattice matching; however, they are significantly more expensive compared to sapphire [47],[48].

One way to aid and potentially avoid the substrate problem is to utilize nanostructures like QDs as the optically active layer in a device, for example, replacing a highly lattice mismatched and strained InGaN quantum well with QDs of comparable optical response can avoid problems associated with the resulting dislocations [48]. In general, QDs have succeeded in enhancing the performance of several devices. Using InAs QDs in laser diodes helps stabilize the temperature and enhance the device's performance [80]. QDs have also resulted in high-efficiency luminescence, even with a high density of dislocations in InGaN devices [30]. In addition, they can be used in single-electron devices for quantum information applications [31].

Alternatively, there exist both bottom-up or top-down methods for forming QDs. The top-down techniques, including lithography [42], split-gate [43], colloidal chemical [44], and etching [45], can create QDs with the required size and location, but these methods are time-consuming and expensive. On the other hand, bottom-up techniques such as self-assembly [46] can form QDs naturally, leading to high densities of QDs easily and quickly. In this self-assembly technique, the quantum dots are formed through strain build-up and relaxation resulting from the lattice mismatch, which is generally identified as the Stranski-Krastanov (S-K) growth mode [46],[47]. InN QDs have been successfully formed on GaN substrates with around ~11% of lattice mismatch using classical S-K growth [11], [51], [81]. Here, the size and density of the QDs are possible to control to some degree via closely controlling growth conditions such as temperature and growth rate [51]. However, the QDs, resulting from this S-K growth mode, have a relatively limited size range, forming naturally from the strain.

Droplet epitaxy (DE) is another growth method for forming semiconductor nanostructures and quantum dots [48], [81]. The substrate is subjected to the group-III atoms, forming liquid droplets following a Volmer-Weber-type growth mechanism [54]. These droplets are then subjected to a group-V molecular beam, which converts them into III-V semiconductor nanocrystals. This is considered the "crystallization" or "nitridation" step in the case of the III-nitride semiconductors. Compared to strain mediated self-assembly growth of QDs, the DE procedure enables the formation of QDs on dissimilar substrates and provides a wide control of the QD shape, size, and density [82]–[84]. However, there is very little information on the growth of InN QDs by DE in the literature [58]. Therefore, more study is necessary in order to practically take advantage of the method in this system.

In the present work, it was demonstrated the growth of InN QDs on c-plane sapphire substrates via droplet epitaxy utilizing molecular beam epitaxy (MBE). In order to separate the fundamental kinetic properties of the liquid In on the surface from the effects due to elevated ambient pressure of nitrogen in the growth chamber [51],[82], the droplet formation was first studied as a function of temperature under ultra-high vacuum conditions, with no nitrogen flow. Then, separately, in order to more closely simulate the environment under which the droplets would finally be crystalized, their formation under a nitrogen ambient pressure which resulted from the nitrogen plasma cell being run under growth conditions but shuttered was investigated. Finally, the droplets formed under these conditions are crystalized for comparison. This process and the statistical results of each step will be discussed below.

4.2 Experimental Methods

Radio frequency (RF) plasma-assisted MBE was used to grow the samples on sapphire substrates. All substrates were loaded, as received into the vacuum chamber load-lock, and outgassed in several steps until the pressure reached below ~10^{-8} Torr. Subsequently, they were transferred to the growth chamber with a base pressure of better than 10^{-10} Torr, where they were heat cleaned for one hour at 850°C. Following the heat clean, the substrate temperature (T_{sub}) was lowered to the droplet growth temperature and held constant throughout the deposition. Droplets were formed by exposing the substrate to an In flux with a beam equivalent pressure of 1.62×10^{-7} Torr for 30 seconds. Three different series of samples were investigated: 1) droplets formed under ultrahigh vacuum (UHV) with the chamber pressure on the order of 10^{-10} Torr; 2) droplets formed under a nitrogen ambient pressure of ~10^{-5} Torr with the plasma struck but shuttered closed, and 3) droplets formed under the same condition as in 2), then subsequently crystallized by exposure to the nitrogen plasma molecular beam at the growth temperature for 15 minutes. The nitrogen flow rate and plasma power were kept at 0.5 sccm and 350 W whenever active.

During the growths, the surface was monitored by an in-situ reflection high-energy electron diffraction (RHEED) system. Atomic force microscopy (AFM) was used to investigate the growth quality, dot's size, and density of the QDs. Finally, x-ray diffraction (XRD) was employed to confirm the presence of crystalized In droplets as well as crystallized InN QDs.

4.3 Results and Discussion

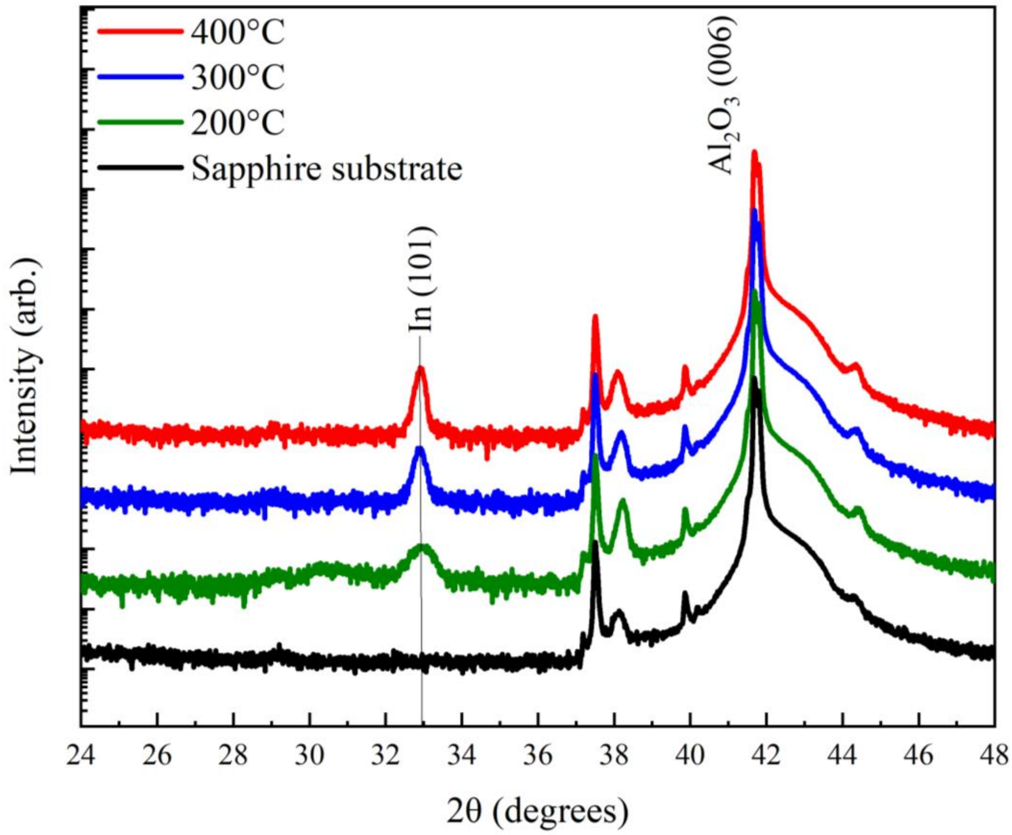

Figure 26: XRD 2θ/ω XRD pattern of In droplets grown on a c-plane sapphire substrate at different T_{sub}, 200 °C, 300 °C, and 400 °C without employing the nitrogen flow or the plasma power and a reference for the c-plane sapphire substrate.

Figure 25 shows the $2\theta/\omega$ XRD measurements of the In droplets grown with no nitrogen exposure and T_{sub} of 200 °C, 300 °C, and 400 °C. Also, it is shown a scan of a clean c-plane sapphire substrate for reference. The diffraction peak at 32.93° is assigned to the metal In (101) diffraction plane, which has been shown to crystallize into its relaxed tetragonal form upon cooling from the growth temperatures for smaller droplets [85]. Further comparison with the sapphire reference, reveals that all features above ~36° in these scans can be assigned to the substrate, with the possible exception of the peak at ~38.1°. This peak is definitely present in the substrate with a possible slight shift; however, it cannot be identified under the current conditions and will not be considered further. Also, it can be observed that the intensity of the In (101) peak strengthens with increasing the substrate growth temperatures. As it is shown below, the higher temperatures resulted in larger In droplets, which resulted in stronger XRD reflections.

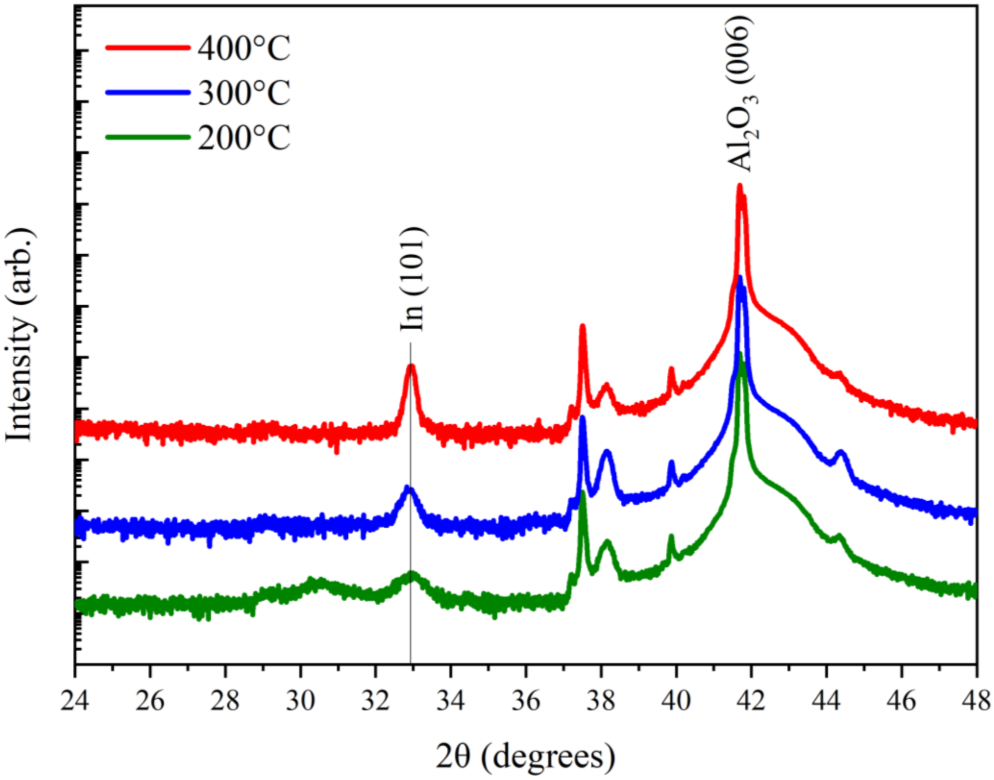

Figure 27: XRD $2\theta/\omega$ XRD pattern of In droplets grown on a c-plane sapphire substrate at different T_{sub} ,200 °C, 300 °C, and 400 °C with the RF plasma on and nitrogen shutter closed.

Figure 27 shows the $2\theta/\omega$ XRD measurements of the In droplets grown under a nitrogen atmosphere with the plasma on at 350 W of RF power and a flow rate of 0.5 sccm, but with the shutter in front of the nitrogen cell closed. In other words, there is no direct line-of-site between the nitrogen plasma source and the substrate. The assumption here is that any activated nitrogen created in the source, either stays in the source or becomes inactive upon scattering off of any surface or another molecule. This is in order to simulate more closely the environment under which the droplets would be formed if they were to be subsequently crystalized in the normal droplet epitaxy fashion. Here, it was seen that qualitatively the In (101) peaks follow the same trend in intensity as for the droplet formation under UHV conditions, however it appears that the droplets formed at 400 °C under a nitrogen ambient have a slightly stronger signal.

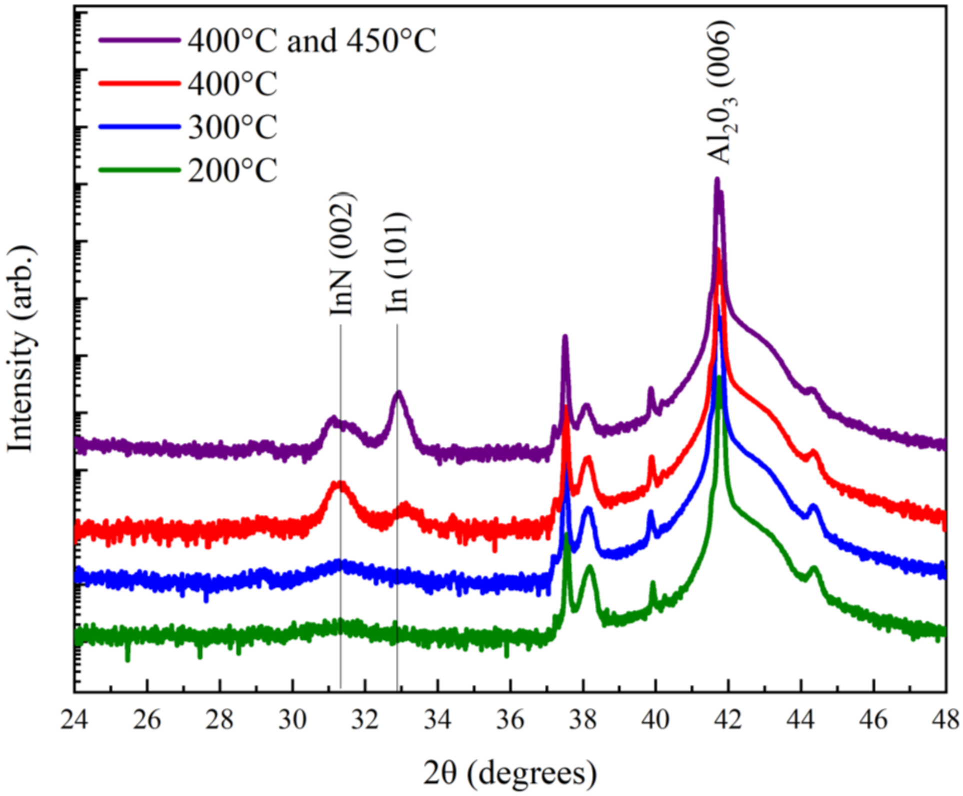

Figure 28: XRD $2\theta/\omega$ pattern of In droplets grown on sapphire substrate at different T_{sub} (g) 200 °C, (h) 300 °C, and (i) 400 °C and crystallized for 15 mins at the same T_{sub}, and (k) is for the In droplets grown at T_{sub} 400 °C and crystallized for 15 mins at 450 °C.

Figure 28 shows the $2\theta/\omega$ XRD measurements of the nitridated In droplets, which were grown at different T_{sub} = 200 °C, 300 °C, and 400 °C and subsequently exposed to the direct beam of the nitrogen plasma for 15 minutes at the growth temperatures to form InN QDs. In addition, there is also shown a sample with droplets grown again at 400 °C, but subsequently crystalized after a fast temperature ramp to 450 °C at a rate of 15 °C /min, then nitridated for 15 min. Finally, we see the InN (002) diffraction peak appearing at 31.38˚ [84]. The position and width of this peak indicate that the wurtzite InN has a bulk relaxed lattice constant and is contained in small nanocrystals or QDs [86]. It can be seen that for the 200 and 300 °C growths the In (101) peak has completely vanished, while the InN (002) peak can be seen very weak and broad. For the 400 °C growth, however, the InN peak becomes well pronounced. Surprisingly, though at this same temperature the In (101) returns. For the sample growth at 400 °C and crystalized at 450 °C it can be seen that the previously intense InN peak starts to degrade, while the In (101) peak returns to nearly its pre-nitridation intensity. The lower temperature results likely indicate that all of the metallic In is consumed in the crystallization process at the lower temperatures, but that the InN QDs that form as a result are either too small or not of sufficient areal density to cause a strong diffraction peak. While the high temperature results indicate that there is a small window of temperature and time (duration of the crystallization) in which to form InN, before decomposition becomes dominant, and the crystalized InN begins to form In again.

In order to investigate the size and density of the formed nanostructures, AFM was performed on all samples. Figure 29 presents the AFM of the set of samples grown under UHV conditions, (a-c) and the set of samples grown under nitrogen ambient conditions, (d-f). Here, it is obvious that for both sets of samples the average size of the resulting droplets increases with increasing the substrate growth temperature, while the areal density decreases. This is expected because the surface diffusion of In atoms rises with temperature [82][87] resulting in classical Volmer-Weber type growth of nanostructures [88] with ripening.

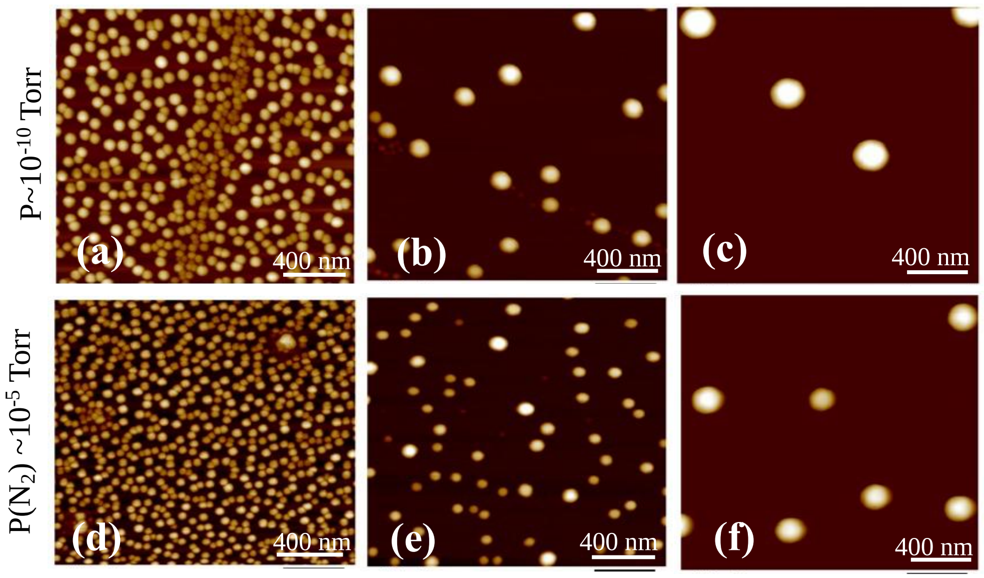

Figure 29: AFM images of (2 × 2) μm of In droplets formed on sapphire substrate at different substrate growth temperatures (a and d) 200 °C (b and e) 300 °C (c-f) 400 °C. Samples (a-c) were grown without plasma or nitrogen flow and samples (d-f) were grown using plasma and nitrogen flow rate, but the nitrogen shutter closed.

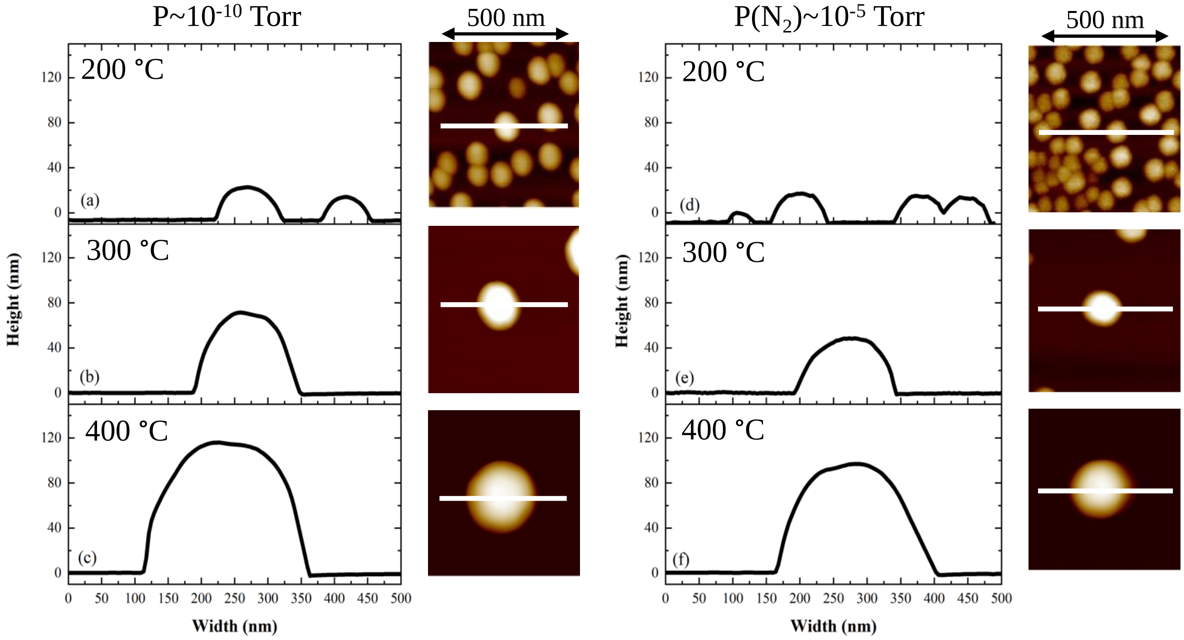

Figure 30: Cross-sectional line-profiles of In droplets on sapphire at different substrate growth temperatures.

Figure 30 shows individual droplet profiles from AFM, and clearly exhibits the increasing dimensions of the droplets with higher substrate temperature which shows how sensitive the In atoms are to the substrate temperature during the formation of droplets. Additionally, it was seen that for samples grown at the same T_{sub} with nitrogen the In droplets are on average smaller and denser than when grown under UHV conditions. This is also as expected from the kinetic nucleation theory of growth [89]–[91], where increased ambient pressure should reduce the mobility of adatoms, resulting in higher density nucleation points and therefore smaller droplets.

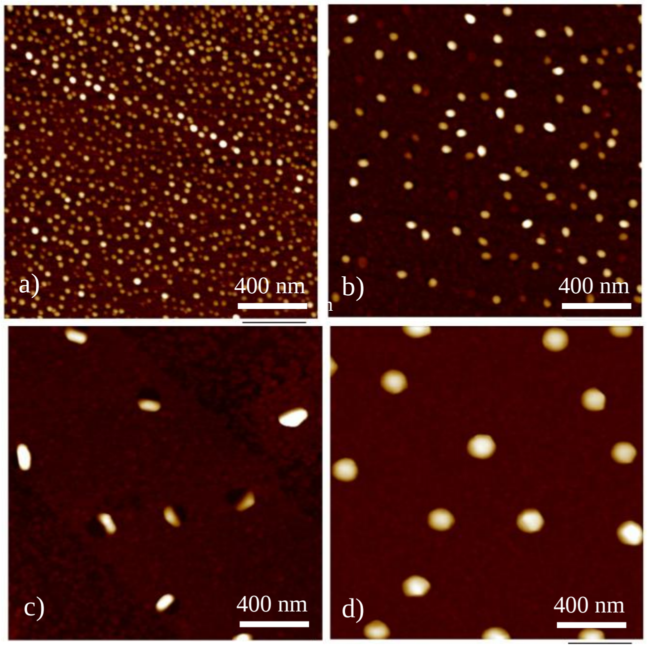

Figure 31: AFM images of (2 × 2) µm of InN QDs formed on sapphire substrate at same growth and crystallization substrate temperatures (a) 200 °C, (b) 300 °C to (c) 400 °C, but (d) shows the InN QDs grown at 400 °C crystallized at 450 °C.

Figure 31 shows the results by AFM of forming the In droplets at various substrate temperatures and subsequently crystallizing them by exposure to nitrogen plasma. As before, the substrate growth temperature was changed from (a) 200, (b) 300 to (c) 400 °C, and crystallization of the In droplets was accomplished at the same temperature as the growth for 15 min. Additionally, Figure 31 (d) shows InN QDs formed from droplets grown at 400 °C for 30 sec, then subjected to nitrogen plasma at 450 °C for 15 min. Figure 32 shows cross section examples of the InN QDs where it is evident that again, the dimensions increase with higher droplet growth temperature as expected. The white lines in 2D AFM insets indicate the line-profiles. The length of each line profiler is 500 nm. Each line profile corresponds to each AFM figure.

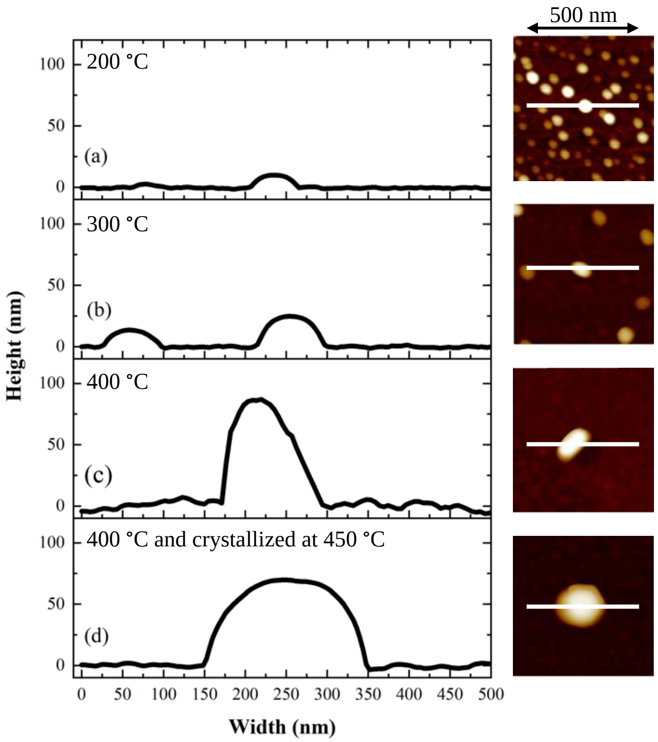

Figure 32: Cross-sectional line-profiles of InN QDs grown at various substrate growth temperatures, (a) 200, (b) 300 to (c) 400 °C, but (d) shows the InN QDs grown at 400 °C and crystallized at 450 °C.

In addition, Figure 33 shows the RHEED pattern transition to spotty, Figure 33 (c), which is characteristic of QD formation, and was observed only after the QD crystallization at 400 °C. The pattern observed from the substrate is normally shadowed during droplet growth. However, the QD spots did not appear for either of the samples grown and crystalized at 200 or 300 °C. This corresponds with the XRD data, which indicated that no significant InN was formed at these low temperatures. However, the sample grown at 400 °C and crystallized at 450 °C showed a significant InN peak in the XRD, and one would expect the RHEED to indicate the same. In fact, the spotty pattern did form after ~2 min of crystallization but further weakened throughout the rest of the 15 min exposure to the nitrogen plasma until there was no evidence of spots by the end. This could indicate a more complicated process of InN decomposition which may be involved during exposure to such high temperatures explaining the significantly intense In XRD peak from this sample.

Figure 33: RHEED pattern of (a) sapphire substrate, (b) In DE, and (c) the nitridated QDs at 400 °C.

The average density, height, and diameter of the In droplets and the crystallized InN QDs are plotted as functions of the droplet growth temperatures for all the samples in Figure 34 (a), ((b), and (c), respectively. It was found that the average density decreases with increasing T_{sub}, while the dot height and diameter both increases. At 200 °C, the lowest T_{sub}, there are significant differences in the average density between the samples grown using three different approaches. The average density of the In droplets grown under UHV conditions was $7.25\times10^{9}\ cm^{-2}$. This increased to $9.88\times10^{9}\ cm^{-2}$ for droplets form under an N_2 ambient. Finally, the crystallized QDs exhibited a density of $18.0\times10^{9}\ cm^{-2}$. At lower temperatures, the diffusion length is small compared to the distance between nucleation sites, so nucleation can form between sites leading to higher density [92]. This follows for each of the deposition approaches. In addition, the size of the droplets deposited under UHV conditions was 29.0 nm in height and 148.10 nm in diameter. Under N_2 ambient, the droplet height was very similar at 30.2 nm, while the diameter decreased to 123.80 nm. In finally crystalizing the InN QDs both the height and diameter fell significantly to 10.5 nm and 67.42 nm, respectively. These results generally follow and can be understood within nucleation theory with thermally activated diffusion. However, the change in density and dimension upon crystallization must be due to some re-evaporation of In due to plasma induced decomposition [93]. In addition, though, the sample grown at 400 °C for 30 sec then exposed to nitrogen plasma at 450 °C showed a similar density of $2.5\times10^{8}\ \mathrm{cm}^{-2}$ as the one grown and crystalized at 400 °C with a significantly smaller height of 3.08 nm and a larger diameter of 8.78 nm. This is indicative of the early stages of a ripening process, with the continued loss due to decomposition and desorption.

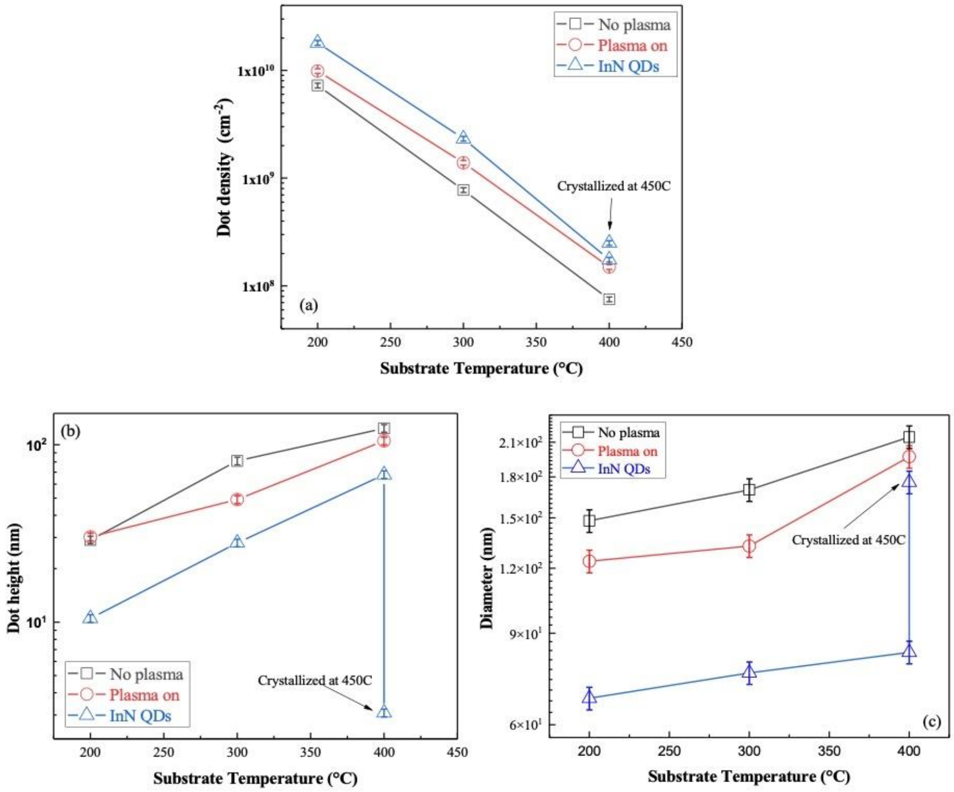

Figure 34: The dot density (a), height (b), and diameter (c) of the In droplets and InN QDs are plotted as a function of substrate temperatures.

When studying the influences of substrate temperature on the size and density of InN QDs, which were crystallized at their growth temperatures, it was found that the height and density of the QDs followed similar trends as the droplets. This is an indication that the crystallization process is as expected and predominantly does not affect the distribution of the droplets. However, it was observed an overall decrease in height and increase in density upon crystallization. This indicates that during the extended crystallization process, the In migrates away from the established nucleation sites which form the droplets, however, the impinging activated N acts to redeposit that In in the form of InN QDs [94]–[96]. This results in a higher density of smaller QDs in comparison with the droplets.

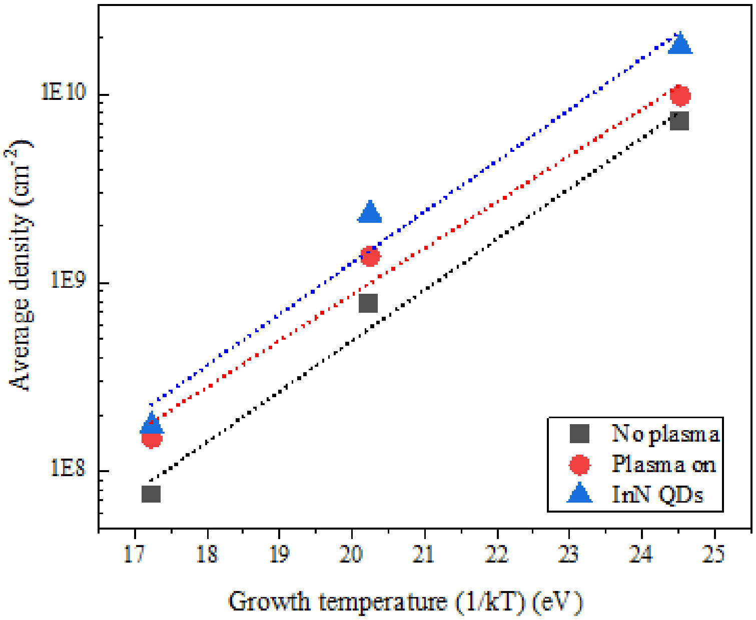

Figure 35: Arrhenius plot of quantum dot density grown using three different approaches: 1) UHV droplet growth, 2) N2 ambient droplet growth, and 3) N plasma crystallized InN QDs growth.

Figure 35 presents the density of nanostructures grown by the three different growth approaches as a function of the inverse temperature. This is the same data as displayed in Figure 34 (a). From this Arrhenius plot, the activation energies were determined via fitting the data to an exponential function. The resulting activation energy for In surface diffusion on sapphire was found to be 0.62 ± 0.07 eV in ultra-high vacuum, ~10^{-10} Torr, and 0.57 ± 0.08 eV in ambient N_2, ~10^{-5} Torr. In addition, it was found that by analyzing the density of crystallized QDs, which followed the droplet formation under ambient N_2, a similar activation energy of 0.63 ± 0.11 eV. By comparison, the activation energy for the In droplets grown on InAs by MBE was found previously to be 0.81 eV [97]. These results match with a classic nucleation theory, and the density of droplets follows the nucleation scaling law with an increase in temperature and Ostwald ripening [98].

Generally, atom migration and the surface diffusion determine the size and shape of the droplets and in turn of the resulting quantum dots, which can be controlled by the growth temperature [99]. Thus, the variation in the sizes and shapes of the QDs using the two different nitridation procedures can be explained in terms of the In atom surface diffusion. As shown in figure 30 (a-c), the nitridation was conducted at the same droplet formation temperatures as in the first two methods. At the low crystallization temperatures of T_{sub} = 200 and 300 °C, the In atom migration was low, resulting in In droplets crystallizing into smaller QDs during the nitridation process. When the In droplets were grown and crystallized under T_{sub} of 400 °C, the In atom diffusion length was higher. These larger In droplets crystallized into QDs that were much smaller and with irregular shapes. In order to effectively convert the In droplets into InN QDs and to prevent the irregular shape in the resulting QDs, it was attempted to crystalize at the higher temperature of 450 °C. The T_{sub} was increased rapidly after the In droplet formation, but the nitridation started only after reaching 450 °C. This resulted in very large diffusion lengths [82], leading to larger In droplets. However, at the higher temperature the crystallization process was very fast. As mentioned above, the RHEED indicated this occurred after only 2 min., followed by a period where InN decomposition was likely a significant factor. This must be considered at T_{sub} = 450 °C [100], [101] leading to a redeposition of indium instead of InN as it was clearly seen in the XRD measurements. The InN peak was significantly decreased, and the indium peak appeared and became stronger. In principle, the density, size, and shape of InN QDs grown by the DE approach can be controlled by further controlling the substrate temperatures of the droplet formation and crystallization process.

4.5 Conclusion

The control of density and size of InN QDs by the DE approach was demonstrated utilizing MBE. Nanostructures were formed under three different conditions for comparison: UHV with no exposure to nitrogen; ambient of nitrogen equivalent having the plasma on but shuttered; and nitridated with the direct nitrogen plasma following droplet formation with the plasma on but shuttered. The size, density, and shape of In droplets and InN QDs were studied via controlling the substrate temperature through the In droplets growth and the crystallization process and were explained utilizing the In atom surface diffusion. The droplet formation was determined to follow well known principles of nucleation theory with ripening. The resulting activation energy for In surface diffusion on sapphire was found to be 0.62 ± 0.07 eV in ultra-high vacuum, ~10^{-10} Torr, and 0.57 ± 0.08 eV in ambient N2, ~10^{-5} Torr. These results should aid in the future development and understanding of InN QDs and QD based devices.

Chapter 5: Investigating self-assembled strain free growth of InN QDs grown on GaN using droplet epitaxy.

5.1 Introduction

Topological insulators provide a mechanism in which spins can be “forced” to remain in the state they are in, called protected states. The spins of confined charges can then be used as qubits with their spin “protected” by the topological phase from the environment. Thus, the initial motivation of this research was to use the features of topological insulators combined with quantum dots to confine a single electron, which will be forced to remain in its spin state until acted upon having the potential for room temperature operation. The internal field present in thin InN quantum wells (QWs) due to internal polarization effects was predicted to drive the system to the topological insulating state as a result of the band edge inversion due to strain [5]. However, instead of growing QWs with more than three monolayers of InN, which is challenging due to strain-relaxation, it was aimed to grow QDs to the same height as the QW thickness prediction for the appearance of topological properties.

In this work, it was attempted to control the InN QDs sizes on GaN utilizing the droplet epitaxy procedure. The substrate growth temperature of InN QDs, although low relative to average MBE growth, is well above the melting temperature of Ga and In resulting in liquid droplets, which can grow in size regardless of the lattice mismatch with the substrate. By using this droplet procedure, a wide range of QD sizes could be controlled as compared with the classical SK or strain driven method of forming self-assembled QDs. Thus, in order to control the height of InN QDs, the conditions for In droplets was first studied since maintaining the size is very challenging after the formation of droplets in the DE method [82], [51]. Then, studying the crystallization conditions of the In droplets with nitrogen-plasma in the MBE growth chamber was accomplished. To date, most of the work on InN QDs growth has been focused on

SK dots with only a few examples of optical measurements [102] [103] [104]. Finally, in order to be able to utilize the InN QDs as an active layer in any devices, the InN QDs were capped via a GaN cap layer.

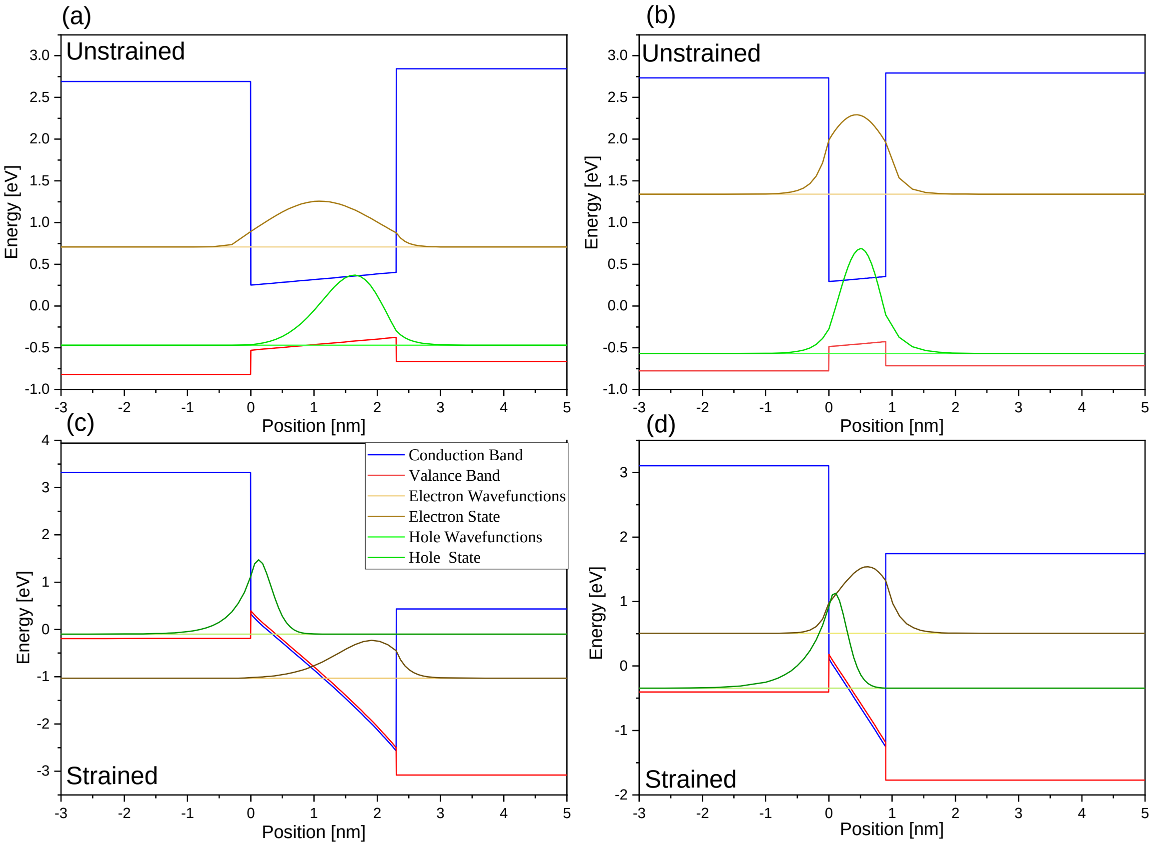

Figure 36: The band structure of GaN/InN/GaN for two different QW thicknesses without strain in (a) and (b) and with strain in (c) and (d).

Moreover, the influence of strain and thickness on the energy gap of InN with various thicknesses was investigated to decrease the bandgap and invert the electron and hole states of the InN QD, which is an indication of a direct point and potential topological insulator behavior. The QDs contain a layer of InN sandwiched between two layers of GaN. Using an effective mass model, the band structure of GaN/InN/GaN is calculated using Nextnano software, as presented in Figure 36 for different QW thicknesses, with and without strain. It was determined that without strain, the intrinsic polarization is not sufficient to invert the band structure even with a larger thickness of several nanometers. However, the application of strain by the GaN substrate resulting from coherent growth results in two strong phenomena. First, the bandgap narrows and inverts due to the large strain and deformation potentials of InN. Second, the resulting piezoelectric polarization results in a substantial quantum-confined stark effect, which ultimately causes the confined electron-hole states to become inverted at ~4 monolayers.

Figure 37 shows the electron-hole transition energy versus the QD thickness in black. For very short QDs, the energy is significantly higher than the fundamental bandgap (0.7 eV) of InN due to the quantum confinement. However, as the thickness of the InN QD rised, the effective transition energy becomes negative at ~ 1.7 nm (~3-4 MLs). Also, the transition probability, which is presented in a red color (Figure 37), demonstrates that the lifetime of the resulting exciton becomes very long as the QD gets large.

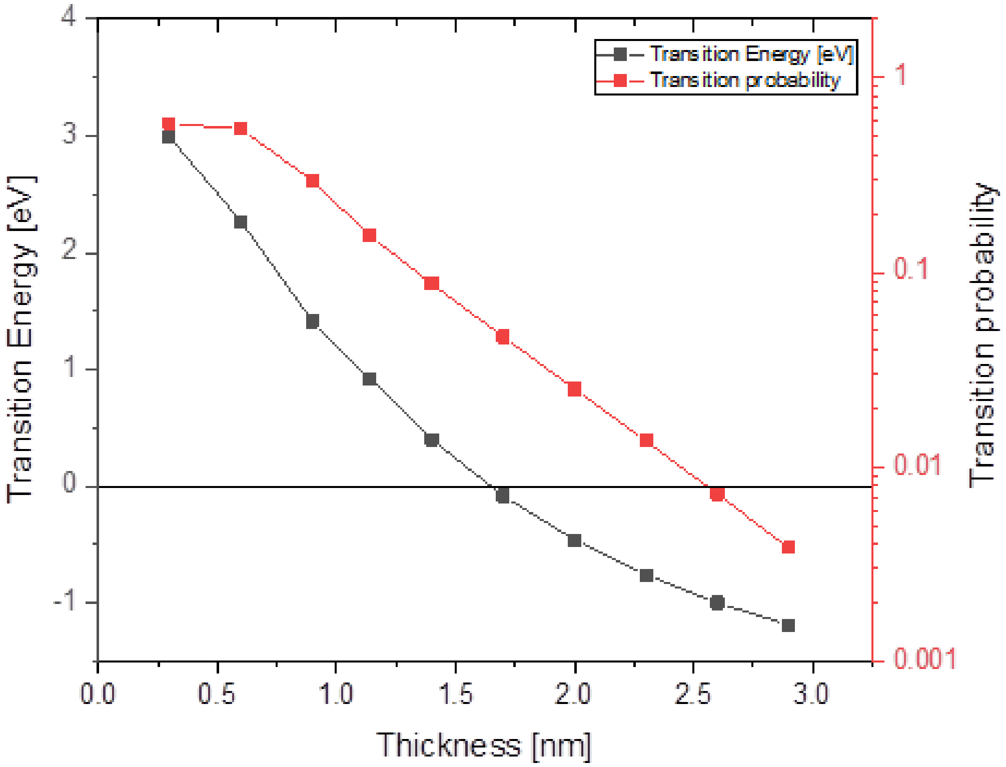

Figure 37: The transition energy in the QDs as a function of different InN thickness.

5.2 The growth of In droplets on GaN under ultra high vaccum

This section has been published as “Investigating self-assembled strain-free growth of In droplets on GaN using droplet epitaxy”, and it is presented here since it is considered one of the main parts of developing the final InN QDs.

In the present work, the growth of In droplets on the GaN buffer layer utilizing the droplet epitaxy procedure in MBE was demonstrated. Generally, maintaining the size is very challenging after the formation of droplets in the DE method. Thus, controlling the dots' size should be accomplished during the formation of the droplets [82], [51]. Also, it has been shown that the substrate temperature strongly affects the density and size of the In droplets [82]. Therefore, the In droplet formation was explored at different substrate temperatures and under ultra-high vacuum conditions to prevent nitrogen from influencing the formation of the In droplets. XRD is used to evaluate the structural characteristics of In droplets. Understanding the In droplet formation can play a substantial role in developing controlled QDs.

5.2.1 Experimental methods

All samples were grown on semi-insulating GaN (0001) templates via molecular beam epitaxy (MBE), while being monitored by reflection high-energy electron diffraction (RHEED). The GaN substrates consisted of ~5 μm of GaN grown on a sapphire substrate. Before growth ~1 μm of Ti was evaporated on the unpolished side of the sapphire wafer in order to allow for radiative heating of the substrates. The substrates, then were outgassed in several steps in vacuum until the pressure reached below ~10^{-8} Torr before introducing to the growth chamber with a base pressure of better than 10^{-10} Torr. Here, they were heat cleaned for one hour at 830 °C for defect-free GaN buffer layer growth. A 177 µm-thick buffer layer of a metal-rich GaN was then grown at 795 °C. The GaN buffer layer was then annealed at 795 °C for ~10 min to stabilize the surface and desorb any access Ga. Subsequently, the substrate temperature was reduced to the droplet growth temperature and held constant throughout the deposition. Droplets were formed via exposing the substrate to In flux with a BEP of 1.62×10^{-7} Torr for 30 seconds after pumping the nitrogen from the chamber and achieving a pressure of less than 10^{-9} Torr. Here, the substrate temperature (T_{sub}) was set to each growth temperature: 30, 50, 75, 95, 200, 300, and 400 °C. The nitrogen flow rate and plasma power were remined constant at 0.5 sccm and 350 W whenever active.

For growth temperatures less than ~100 °C, the substrate was allowed to stabilize for up to 2 hours under constant heater power, so that the surface temperature could reach the low values and that the automatic regulation did not provide any power pulses during growth. During the In deposition, the RHEED intensity was seen to decrease indicating an increase in surface coverage of non-crystalline material. In order to prevent the effects of ripening, the samples grown at 95 °C and lower were immediately transferred out of the growth chamber. However, for samples grown at 200, 300, and 400 °C, the substrate temperature was reduced rapidly at 50 °C /min right after finishing each growth. When the substrate temperature reached 100 °C, the samples were transferred out of the growth chamber. The growth quality, dot density, diameter, and height of the droplets were investigated after growth using Atomic Force Microscopy (AFM). Finally, x-ray diffraction (XRD) was employed to confirm the presence of crystalized In droplets.

5.2.2 Results and Discussion

The main objective is to study the controlling of the density and size of In droplets since it is the initial and the most important step in developing controlled InN QDs. This is accomplished by controlling the substrate temperature from near room temperature to a high substrate growth temperature at a fixed growth time of 30 sec. Figure 38 shows the $2\theta/\omega$ XRD measurements of the In droplets grown under ultra-high vacuum at T_{sub} ranging from 30 °C to 400 °C. The diffraction peaks at 32.93° and 34.57° are assigned to the metal In (101) diffraction plane and wurtzite structure of GaN (0002), respectively. This demonstrates two main results: 1) that the In is crystalline an aligned with the (101) tetragonal face parallel with the substrate surface, and 2) that there is no InN present. Both of these directly correspond with RHEED observations in that any formation of InN would have occurred at higher temperatures and been visible in the RHEED as spots, and the droplets that did form were liquid at the higher temperatures and did not create a diffraction pattern in the RHEED. As it is shown below, the peaks for lower growth temperatures appear broader, which is a general indication of smaller dots.

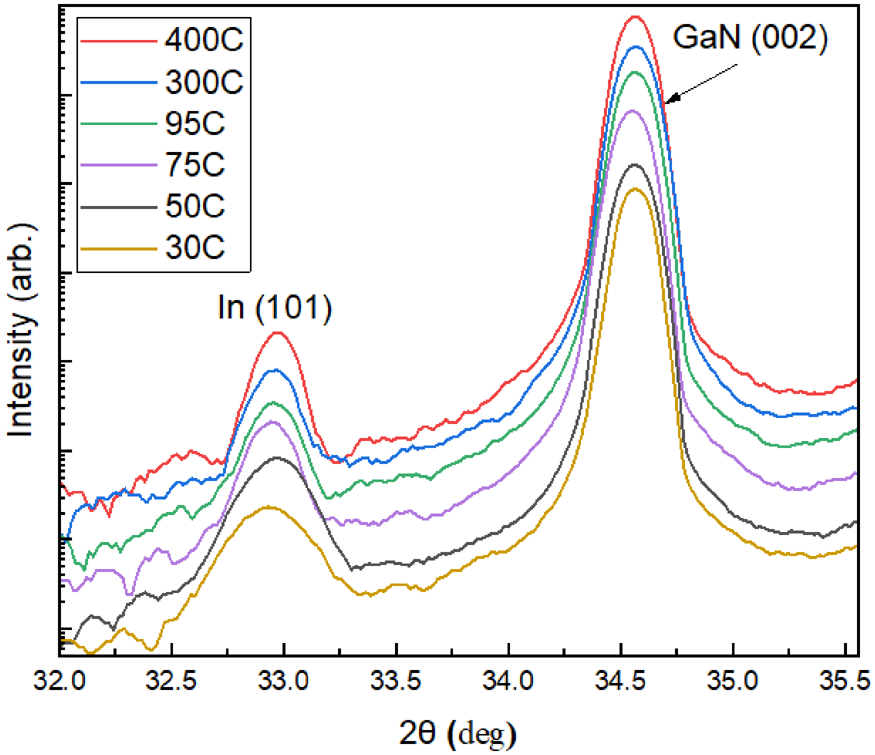

Figure 38: $2\theta/\omega$ XRD pattern of In droplets grown on a GaN buffer layer at different T_{sub} under high vacuum.

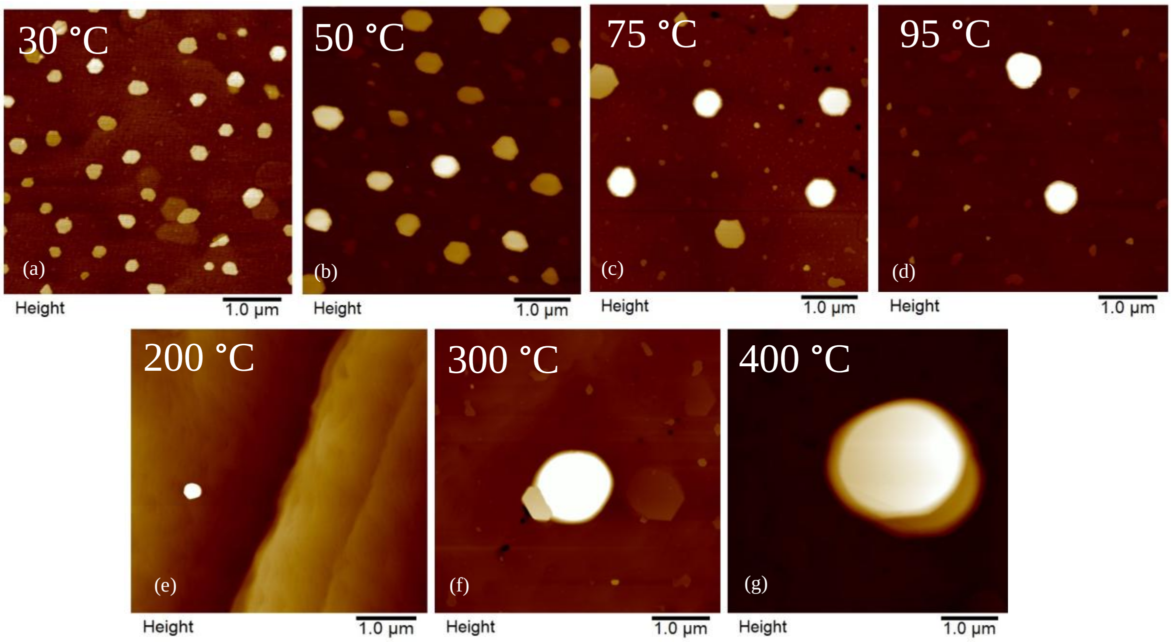

Figure 39: AFM images of (5 × 5) μm of In droplets formed on GaN buffer layer at different T_{sub}.

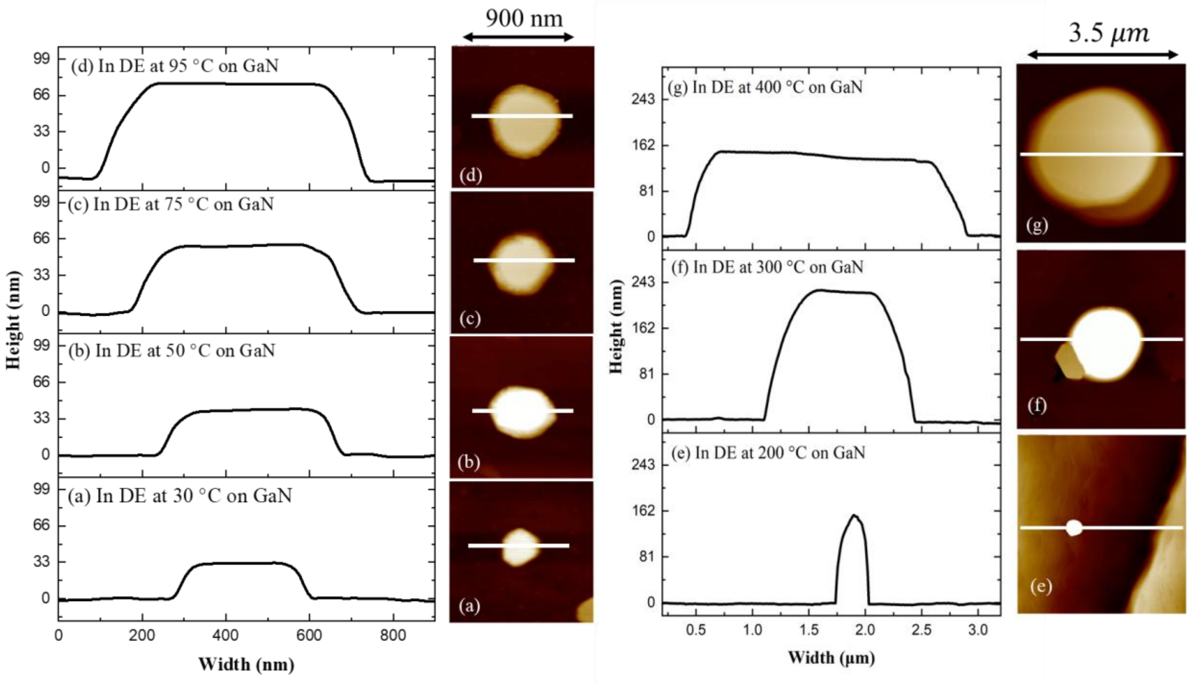

Figure 40: Cross-sectional line-profiles of the grown In droplets at different substrate growth temperatures. The white lines in 2D AFM insets indicate the line-profiles. The length of each line profiler is 900 nm for (a-d) images and 3.5 μm for (e-g) images. Each line profile corresponds to each AFM figure.

AFM was used to investigate the size and density of the In droplets. Figure 39 shows 5 μm × 5 μm AFM images of each sample. Generally, there are several features, and possibly even two different sizes of droplets or dots on some of the samples. In what follows, it is focused on the distribution of the larger droplets, which are found on all samples. Figure 40 shows cross sections of the In droplets formed at different T_{sub}, which demonstrates the monotonic increase in droplet size with higher growth temperature. Generally, all samples exhibit droplets with relatively steep sidewalls and flat tops. In addition, the SEM measurements were performed to describe uniformity, size distribution, surface morphology, and density of the In droplets. The SEM images are displayed in Figure 41 for the samples grown at 200, 300, and 400 °C. The average density, diameter, and height of the In droplets are plotted as functions of the growth temperature in Figure 42 (a), (b), and (c), respectively, as well as in table 2. Here, it is evident that the average size of the droplets enlarged with higher substrate growth temperature while the areal density drops, which confirms that the In atoms are tremendously sensitive to changes in the substrate temperature during the formation of the droplets even at extremely low temperatures such as 30 °C. This is predictable since the surface diffusion length of In atoms raised with temperature [82], [94] resulting in a Volmer-Weber type growth of nanostructures [88] with ripening.

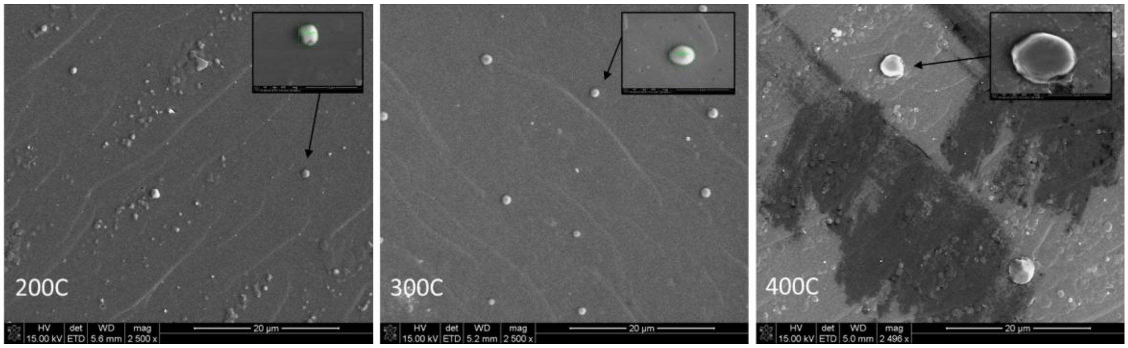

Figure 41: SEM images for the samples grown at 200, 300, and 400 °C.

It can be clearly observed from Figure 42 that there is a slightly different variation in the In droplet size and density for samples grown at higher temperatures (200, 300, and 400 °C) from those grown at lower temperatures (below 100 °C). For a high T_{sub} of 400 °C, the size of the In droplets was 2.56 µm in diameter and 166.36 nm in height with a density of 7.5×10^{5} cm^{-2}. The diameter of the droplets was further reduced from 1.51 µm to 1.2 µm with decreasing T_{sub} from 300 to 200 °C. However, the height was increased to 236 nm for the sample grown at 300 °C and then reduced to 159 nm when decreasing T_{sub} to 200 °C. At the T_{sub} of 95 °C, the droplet dimensions were considerably dropped to 815 nm for the diameter and 86 nm for the height, and the density was improved to 8×10^{6} cm^{-2}. This can be due to the decline in adatom diffusion length, caused by the reduction in substrate temperature. With a further decrease of T_{sub} from 75 °C to 50 °C, the droplet dimension continued to decrease. At a near room temperature of 30 °C, the droplet dimension was reduced to 35.02 nm in height and 384.88 nm in diameter, and the density considerably enhanced to 1.36×10^{8} cm^{-2}.

Table 2: In droplets' height, diameter, and density at different substrate temperatures formed under UHV.

T_{sub} (°C)	**Density** (cm^{-2})	**Diameter** (nm)	**Height** (nm)	**Aspect ratio** -
400	7.5×10^{5}	2560	166.4	15.38
300	7.5×10^{5}	1510	236	6.39
200	1.0×10^{6}	1200	159	7.54
95	8.0×10^{6}	815	86	9.47
75	1.5×10^{7}	697	61.31	11.36
50	2.6×10^{7}	586	39.08	14.99
30	1.36×10^{8}	384.8	35.02	10.99

Examination of the aspect ratio of the droplets in Table 1 (diameter divided by height) with increasing growth temperatures showed an increase for very low T_{sub} of 30 ˚C to 50 ˚C of 10.9 to 14.9 [57], [92], [105], [106]. However, it was observed that the aspect ratio then dropped monotonically from 14.99 at T_{sub} = 75 °C to 6.39 at T_{sub} = 300 °C. Further increase of T_{sub} to 400 °C saw a sudden, nearly threefold increase to 15.38. This observed increase at very low temperatures is a sign of extremely low diffusion length, and the primary addition of extra adatoms to the top surface of the droplets, whereas further increase in temperature adds primarily to the diameter with less diffusion up the surface of the droplet. Finally, at the highest temperatures, it was seen that the beginning effects of evaporation, which appears to happen primarily at the top of the droplets resulting in a reduction in height [57], [92], [94], [105].

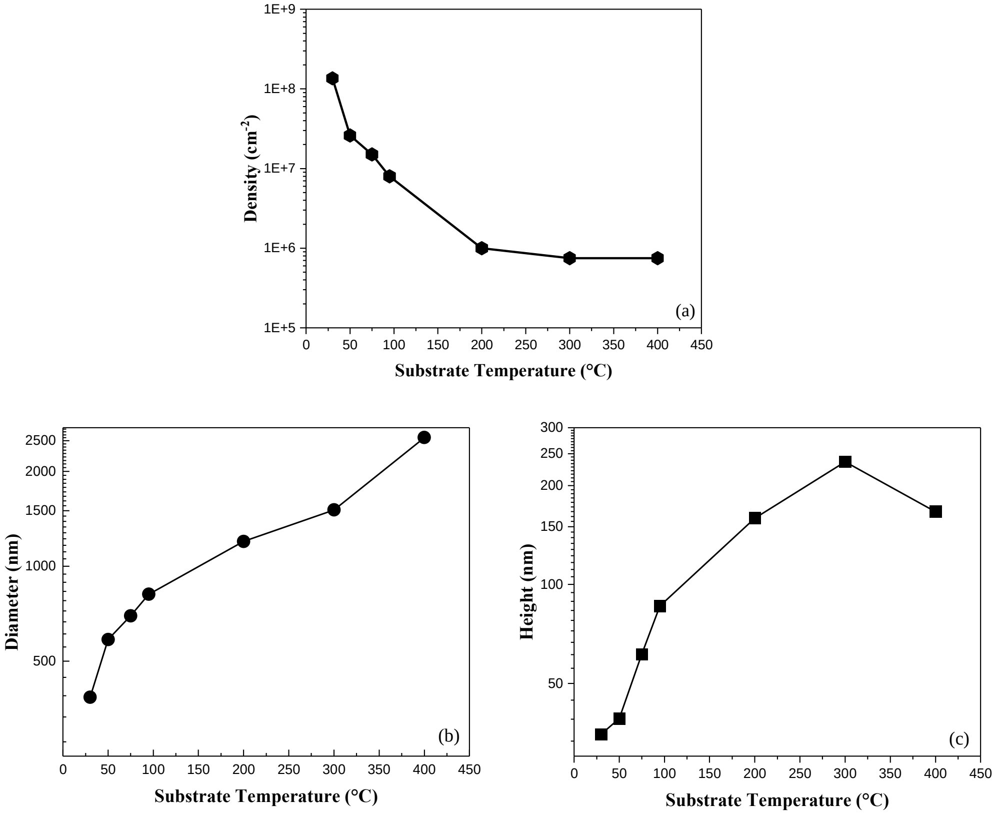

Figure 42: The density (a), diameter (b), and height (c) of the In droplets are plotted as a function of substrate temperatures.

To further evaluate the influence of temperature on the droplet density, the average density of In droplets as a function of the inverse temperature is presented in Figure 43 (a) and (b) for two different temperature ranges: ~30 °C to ~100 °C, and 200 °C to 400 °C, respectively. From this Arrhenius plot, the activation energies (E_a) were determined via exponential fitting, and it was found to be 0.39 eV for low-temperature range and 0.04 eV for high-temperature range. These relatively low activation energy values indicate that In atoms diffuse relatively faster with higher temperatures [98]. Comparing our results to previous works in the literature, it was found that our E_a for low T_{sub} is very similar to that of In on GaAs, which was found to be 0.34 eV under low 10^{-5} background pressure [106]. This result agrees with a classic nucleation theory, and the density of droplets follows the nucleation scaling law with an increase in temperature as predicted by Ostwald ripening [98].

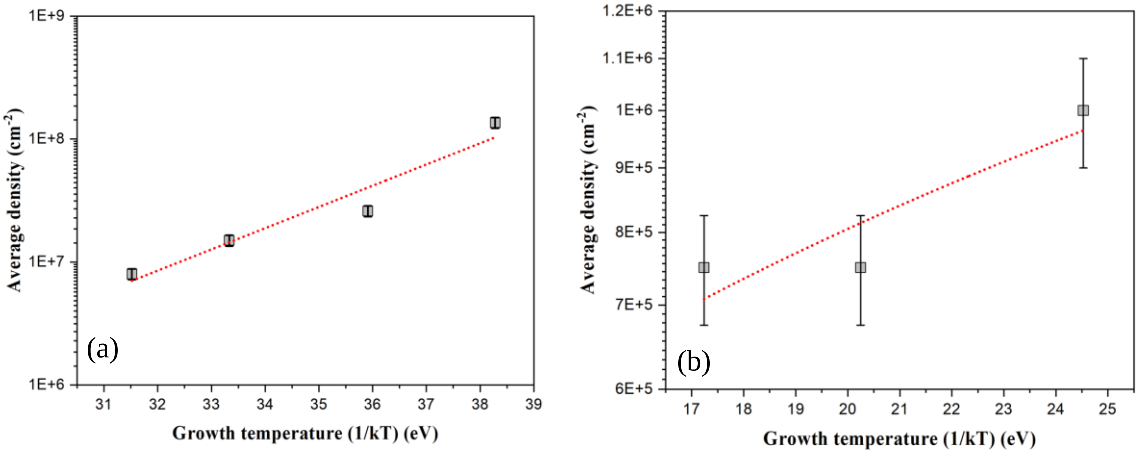

Figure 43: Arrhenius plot of quantum dot density as a function of (1/kT) at (a) low (30, 50, 75, and 95 °C) and (b) high (200, 300, and 400 °C) substrate growth temperatures.

Because of the higher surface diffusion at a higher temperature, the density became noticeably smaller. This can be explained by the time required to cool down to 100 °C after the In deposition, before removing the sample from the growth chamber. Even though T_{sub} was reduced very quickly after the deposition at 50 °C /min, these times increased the time for In diffusion, which affected the size and density of the droplets through Ostwald-ripening [107]. From these observations, the results agree well with the literature that the substrate growth temperature affects the density (smaller) and dimension (larger) of the droplets at higher T_{sub} [57], [95], [108]. Nevertheless, the diffusion length of In adatoms surprisingly continues to be affected even at near room temperature.

5.2.3 Conclusion

In droplets grown on GaN by droplet epitaxy were demonstrated with MBE. The droplets were formed under UHV with no nitrogen exposure to prevent both reaction with nitrogen and the diffusion suppression of elevated pressure on the growth of In droplets. The density and size of the In droplets were studied as functions of the substrate temperature during their formation and explained utilizing the In atom surface diffusion. Even at extremely low substrate temperatures of ~30 °C, the In atoms are extremely sensitive to the substrate temperature during growth. The highest density of $1.36 \times 10^{8}\ cm^{-2}$ was observed at a relatively low substrate temperature of 30 °C. This study can assist in understanding the first stage of forming a controlled InN QD on GaN using DE, which is promising for quantum information applications.

5.3 The growth of In droplets on GaN under low vacuum conditions

In order to simulate more closely the environment under which the droplets would be formed if they were to be subsequently crystalized in the normal droplet epitaxy fashion, the In droplets were grown under a nitrogen ambient pressure of $\sim 10^{-5}$ Torr with the plasma struck but shuttered closed.

5.3.1 Experimental method

As in the previous section, all samples here were grown on semi-insulating GaN (0001) templates by molecular beam epitaxy (MBE). The same substrate preparation process was followed in this set of samples. After transferring the substrates to the growth chamber, they were heat cleaned for one hour at 830 °C in order to remove any residual contaminants from the template surface, as well as the Ti back coating. Then, a 177 nm-thick buffer layer of metal-rich GaN was grown at 795 °C. The GaN buffer layer was then annealed at 795 °C for ~10 min to stabilize the surface and desorb any access Ga. Subsequently, the substrate temperature was decreased to the droplet growth temperature and held constant throughout the deposition.

Droplets were formed by exposing the substrate to In flux with a BEP of 1.62×10^{-7} Torr for 30 seconds under a nitrogen ambient pressure of $\sim10^{-5}$ Torr at each of the growth temperatures, T_{sub} = 35, 50, and 100 °C. The substrate was allowed to stabilize for up to 2 hours under constant heater power, so that the surface temperature could reach the low values and that the automatic regulation did not provide any power pulses during growth. During the In deposition, the RHEED intensity was seen to decrease indicating an increase in surface coverage of non-crystalline material. In order to prevent the effects of ripening, the as-grown samples were immediately transferred out of the growth chamber.

5.3.2 Results and Discussion

Figure 44 displays the $2\theta/\omega$ XRD measurements of the In droplets grown under a nitrogen atmosphere with the plasma on at 350 W of RF power and a flow rate of 0.5 sccm, but with the shutter in front of the nitrogen cell closed. Thus, there is no direct line of site between the nitrogen plasma source and the substrate. The assumption here is that any activated nitrogen created in the source, either stays in the source or becomes inactive upon scattering off from any surface or another molecule. This is in order to simulate more closely the environment under which the droplets would be formed if they were to be subsequently crystallized in the normal droplet epitaxy fashion. Here, it was seen that qualitatively the In (101) peaks follow the same trend in intensity as for the droplet formation under UHV conditions. The peaks for lower growth temperatures appear broader, a general indication of smaller dots.

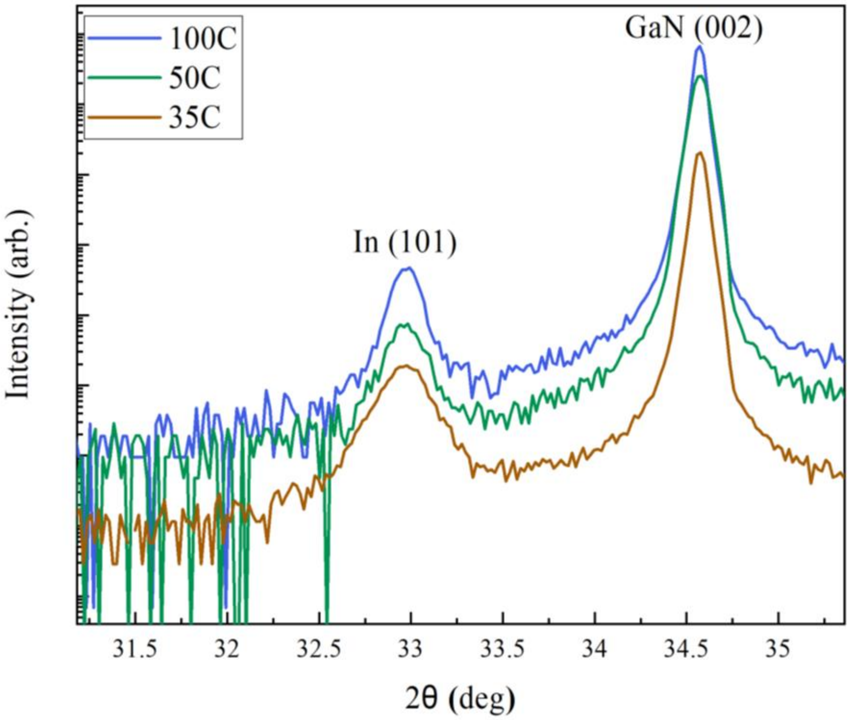

Figure 44: $2\theta/\omega$ XRD pattern of In droplets grown on a GaN buffer layer at different T_{sub} under low vacuum.

Figure 45 shows the AFM of the samples grown under nitrogen ambient conditions. As seen in the droplets grown on GaN under UHV, the average size of the resulting droplets enlarged with increasing the substrate growth temperature while the areal density decreases. Again, this is expected since the surface diffusion of In atoms increases with temperature [82][87] resulting in classical Volmer-Weber-type growth of nanostructures [88] with ripening. Figure 46 clearly exhibits the enlargement of droplet dimensions with increasing the substrate temperature, which shows how sensitive the In atoms are to the substrate temperature even at near room temperatures during the formation of droplets. Additionally, it was seen that for samples grown at the same T_{sub} under nitrogen ambient conditions and under UHV (see section 5.2), the In droplets are on average smaller and denser when grown under higher nitrogen pressure. This is also as expected from the kinetic nucleation theory of growth [89]–[91], where increased ambient pressure should reduce the mobility of adatoms, resulting in higher density nucleation points and smaller droplets.

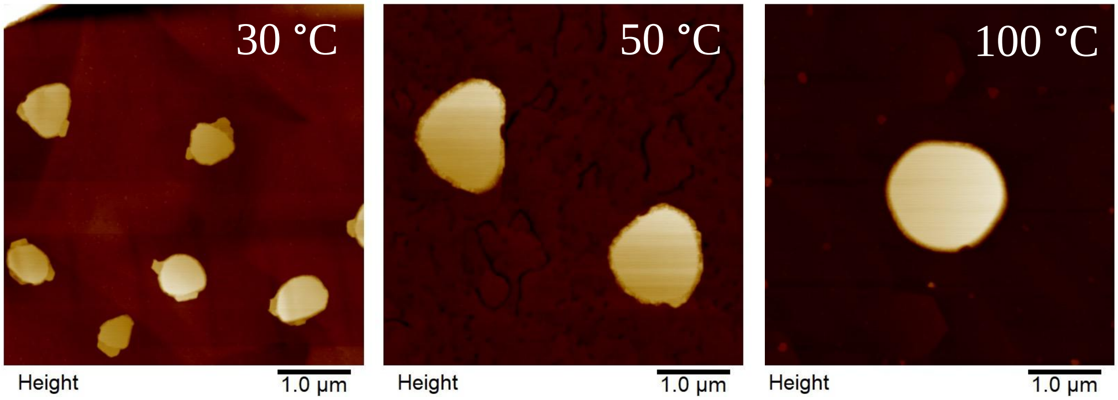

Figure 45: AFM images of (5 × 5) μm of In droplets formed on GaN at different substrate growth temperatures 30, 50, and 100 for 30 sec under ambient nitrogen pressure.

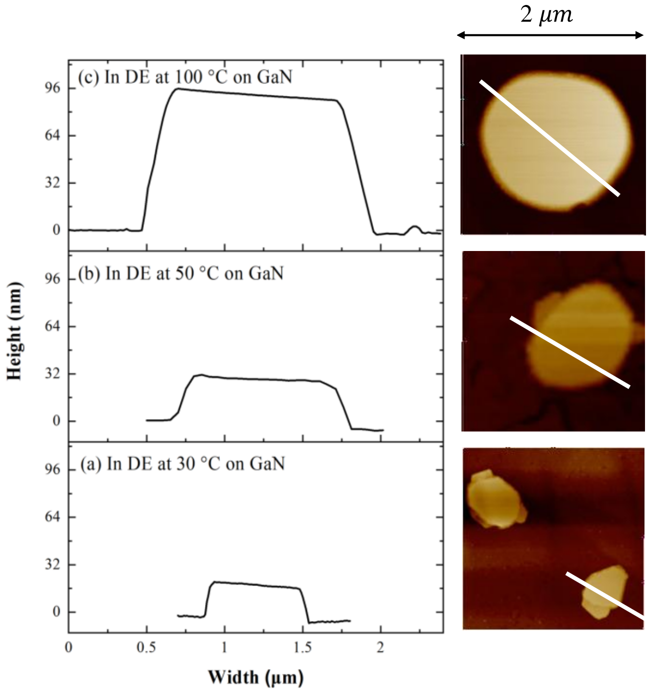

Figure 46: Cross-sectional line profiles of In droplets grown at different T_{sub} under ambient nitrogen pressure.

Figure 47 a, b, and c present the average density, diameter, and height of the In droplets grown under low vacuum plotted as functions of the substrate growth temperature, respectively, while Table 3 shows these values for comparison. It is obvious that the average size of the droplets increases under low vacuum more than in the sample grown under UHV (see section 5.2, Figure 39) and with higher substrate growth temperature while the areal density drops, which confirms that the In atoms are extremely sensitive to the changes in the T_{sub} during the formation of the droplets, even at extremely low temperatures such as 30 °C. A horizontal error bar is associated with the precision of the substrate temperature identified by the thermocouple and equals approximately ± 10 °C.

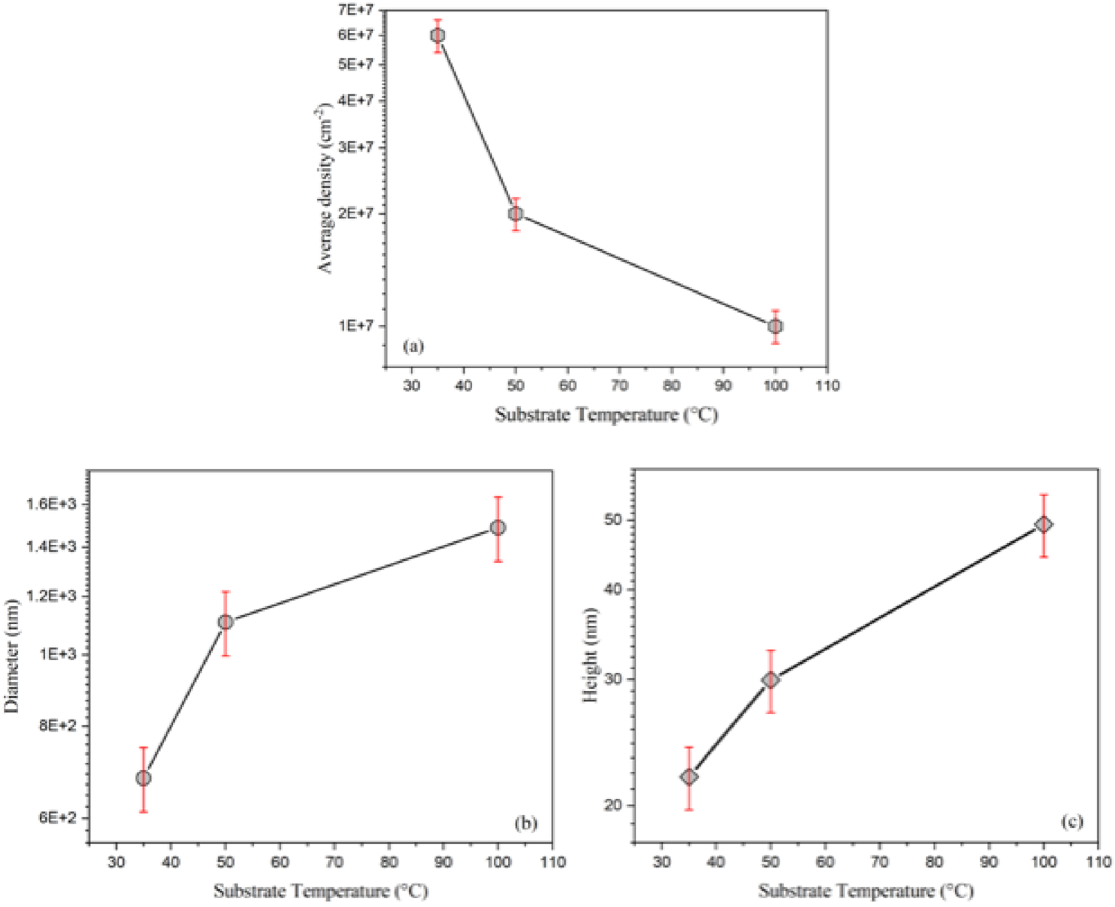

Figure 47: The density (a), diameter (b), and height (c) of the In droplets formed in ambient N2 versus T_{sub}.

Compared with the In droplets grown under UHV on GaN at T_{sub} = 30 °C (see section 5.2, Figure 39), there are significant differences in the average density and size. The average density of the In droplets grown under UHV conditions was 1.36×10^8 cm^{-2}, and it was reduced to 6×10^7 cm^{-2} for In droplets formed under ambient nitrogen. In addition, the height of In droplets formed under an N_2 ambient was 21.2 nm which is smaller than that of the In droplets formed under UHV (35.02 nm), while the diameter increased to 680 nm in comparison to 384.8 nm of the In droplets formed under UHV implies a very low surface energy of In droplets at low temperatures on GaN, which favors a flat droplets shape.

Table 3: In droplets' height, diameter, and density at different substrate temperatures.

T_{sub} (˚C)	Density (cm^{-2})	Diameter (nm)	Height (nm)	Aspect ratio -
100	1×10^7	1488	49.3	30.18
50	2×10^7	1107	29.9	36.97
30	6×10^7	680	21.2	30.98

The aspect ratio of the In droplets formed under low vacuum in Table 3 (diameter divided by height) showed an increase for very low T_{sub} of 30 °C to 50 °C of 30.98 to 36.97 and a decrease to 30.18 at T_{sub} = 100 °C. This increase at shallow temperatures (30 °C and 50 °C) is an indication of the very low diffusion length. The primary addition of extra adatoms to the top surface of the droplets, whereas a further increase in temperature, adds primarily to the diameter with less diffusion up the droplet's surface as seen in the droplets grown at 100 °C. According to the kinetic nucleation theory of growth, increased ambient pressure should reduce the mobility of adatoms, resulting in higher-density nucleation points and smaller droplets. However, since the surface energy of a liquid droplets is low at low temperatures along with the low mobility under high ambient pressure, the metal liquid droplets tend to expand its surface area, and the contact angle between a metal liquid droplet and a solid reduced. Therefore, the liquid favors a flat droplets shape on the surface [59]. Apparently, the chemical nature of the solid and liquid as well as the substrate temperatures significantly influence a liquid wetting the solid substrate [59].

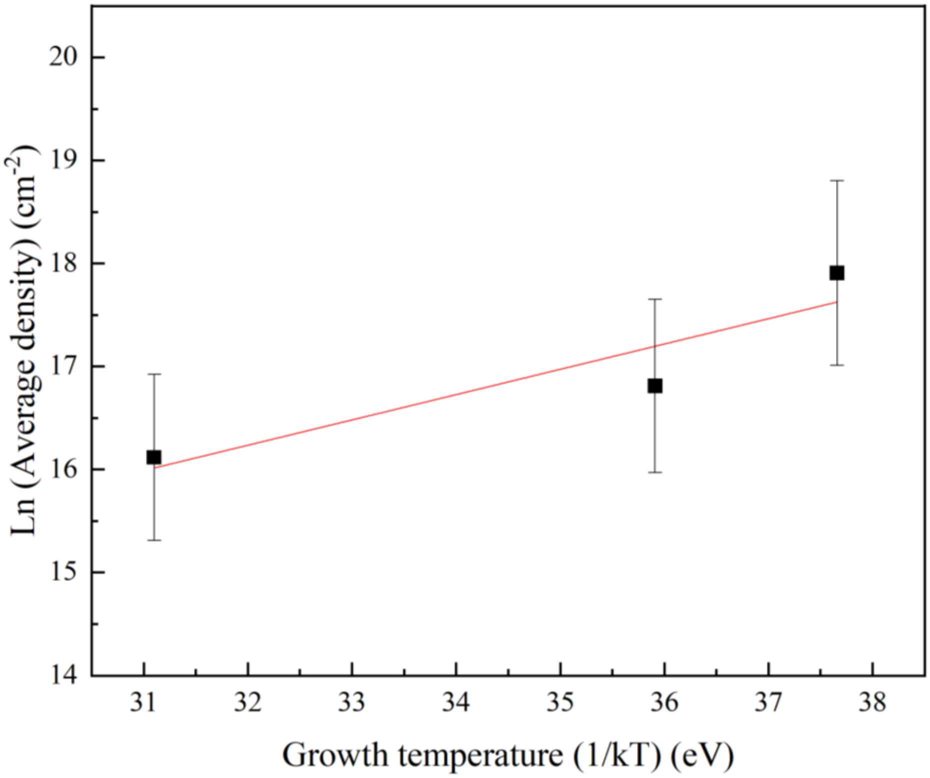

Figure 48: Arrhenius plot of In droplets density formed in ambient N_2 versus growth temperature (1/kT).

To further evaluate the effect of temperature as well as the nitrogen background pressure on the droplet density, the average density of In droplets formed in ambient N_2, ~10^{-5} Torr is plotted as a function of the inverse temperature, presented in Figure 48. From this Arrhenius plot, the activation energy, E_a, was determined via exponential fitting, and found to be 0.25 ± 0.10 eV which is lower than the 0.39 eV found for droplets formed under ultra-high vacuum, ~10^{-10} Torr, on GaN in the same growth temperature range. It was observed that when the substrate growth temperatures are lower than the In melting point of 156.6 °C, the In droplet density varies from the single exponential law of the nucleation theory [98] [109], leading to a decrease in the activation energy. Such result is coherent with other studies of the growth of In droplets on Ga leading to a decrease in the activation energy. Such result is consistent with other studies of the growth of In droplets on GaAs [110] and Ga droplets on GaAs [111] In addition, it was found that the surface diffusion length of In adatoms is strongly dependent on the growth temperature and the ambient N_2 background pressure. Thus, the surface diffusion length of In adatoms on GaN surface goes up with reducing the ambient N_2 background pressure.

5.4 The growth of InN QDs on GaN

5.4.1 RHEED study of InN QDs Formation

RHEED real time tracking of the surface was the main tool used in this section to comprehend the surface morphology during the growth and to find the optimum temperature at which the transition to spotty pattern appeared, which indicated the nanocrystal formation.

5.4.1.1 Experimental Methods

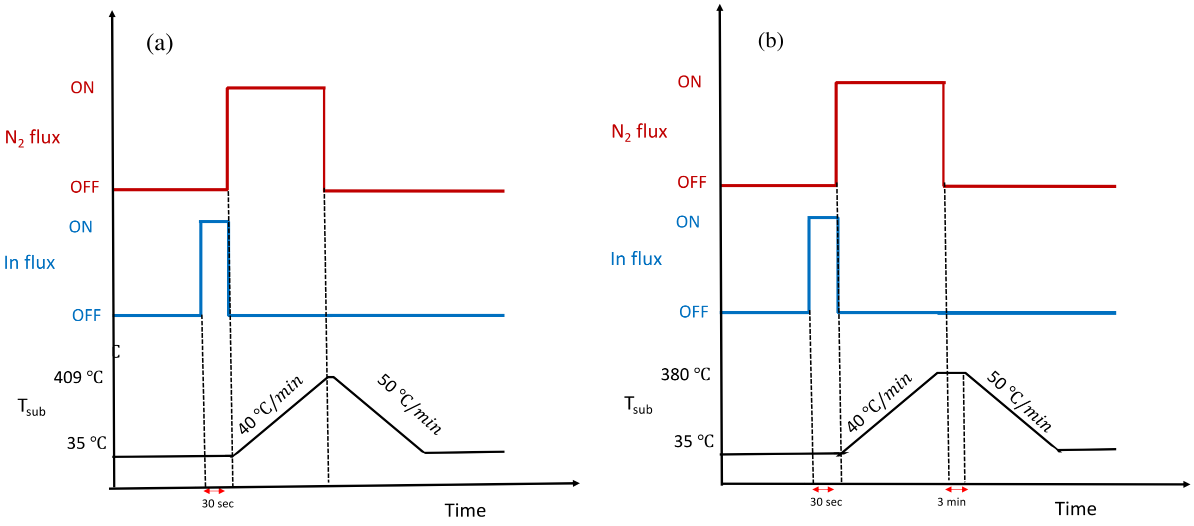

Figure 49: An illustrating of two different growth methods utilized to crystalize the In droplet a) at 500 °C and b) at 380 °C and annealed at 380 °C for 3 min.

Here, the necessary process for the formation of droplet epitaxial InN QDs on GaN was investigated via RHEED. Two separate experiments were performed to observe the temporal evolution of surface morphology. As in the previous section, both experiments were performed on semi-insulating GaN (0001) templates by MBE. The same substrate preparation process was followed. After transferring the substrates to the growth chamber, they were heat cleaned for one hour at 830 °C and followed by a 177 nm-thick buffer layer of metal-rich GaN grown at 795 °C. The GaN buffer layer was then annealed at 795 °C for ~10 min to stabilize the surface and desorb any access Ga. Subsequently, the substrate temperature was decreased to 35 °C and held constant throughout the droplet deposition. In droplets were formed by exposing the substrate to In flux with a BEP of 1.62×10^{-7} Torr for 30 seconds under a nitrogen ambient pressure of $\sim10^{-5}$ Torr. In the first testing experiment, as illustrated in Figure 49 (a), the nitrogen shutter was opened immediately after closing the In shutter and the substrate was increased to 500 °C at a rate of 40 °C/min in order to see at which temperature the transition to 3D (spotty pattern) occurred and then the substrate temperature was reduced to 100 °C at a rate of 50 °C/min. In the second testing experiment, as illustrated in Figure 49 (b), the nitrogen shutter was opened immediately after closing the In shutter and increased to 380 °C at a rate of 40 °C/min for 12 min and followed by 3 min annealing at 380 °C to complete the conversion process. The nitrogen flow rate and plasma power were kept at 0.5 sccm and 350 W whenever active. In both cases, the growth of the InN QDs were tracked continuously vis RHEED.

5.4.1.2 Results and Discussion

Figure 50 displays the RHEED patterns observed at each stage of experiment 1. Prior to the In droplet deposition, the RHEED pattern exhibited long streaks (Figure 50 (a)) indicating a 2D surface. After depositing In on the surface for 30 sec, the RHEED pattern becomes diffused

(Figure 50 (b)) due to the formation of liquid In droplets and effective shadowing of the surface. After 3 min of introducing the RF plasma nitridation, the RHEED pattern became bright and streaky again (Figure 50 (c)), likely as the surface of the exposed In began to crystallize. Subsequent changes in the RHEED pattern over time and temperature are described as follows. At t = 8 min and at $T_{sub} \approx 275$ °C, the intensities of streaks were increased with the appearance of small spots (Figure 50 (d)). At t = 9 min and at $T_{sub} \approx 395$ °C, the intensity increased, and the spots became more distinct (Figure 50 (e)). At t = 9 min & 20 s and at $T_{sub} \approx 410$, the spotty pattern became sharp and bright °C (Figure 50 (f)), which confirmed the complete formation of 3D nanocrystals or QDs on the surface. The spotty pattern is the result of transmission electron diffraction through the 3D material. As T_{sub} reached 435 °C, the spotty pattern began to weaken as in Figure 50 (g) until the pattern became diffused demonstrating an amorphous thin film. This could indicate a more complicated process of InN decomposition which may be involved during exposure to such high temperatures, leaving liquid In on the surface again. It was observed from this experiment that the transition to spotty started to appear at ~ 355 °C and became very clear and bright at ~ 380 °C. Finally, the RHEED pattern began to decay after 410 °C. Based on these observations, in the second experiment T_{sub} was ramped to 380 °C quickly, and the RHEED was observed over time, while soaking at that temperature to determine the time required for full crystallization.

Figure 51 shows the RHEED patterns observed at each stage of the droplet epitaxy of InN QDs in the second experiment. As previously, the transition to spotty appeared at ~ 355 °C and became bright and sharp by ~ 380 °C. After soaking the sample in the nitrogen plasma at T_{sub} at 380 °C further, the intensity of the pattern continued to increase. This indicates that the InN QDs continued to ripen, becoming better defined, a higher quality.

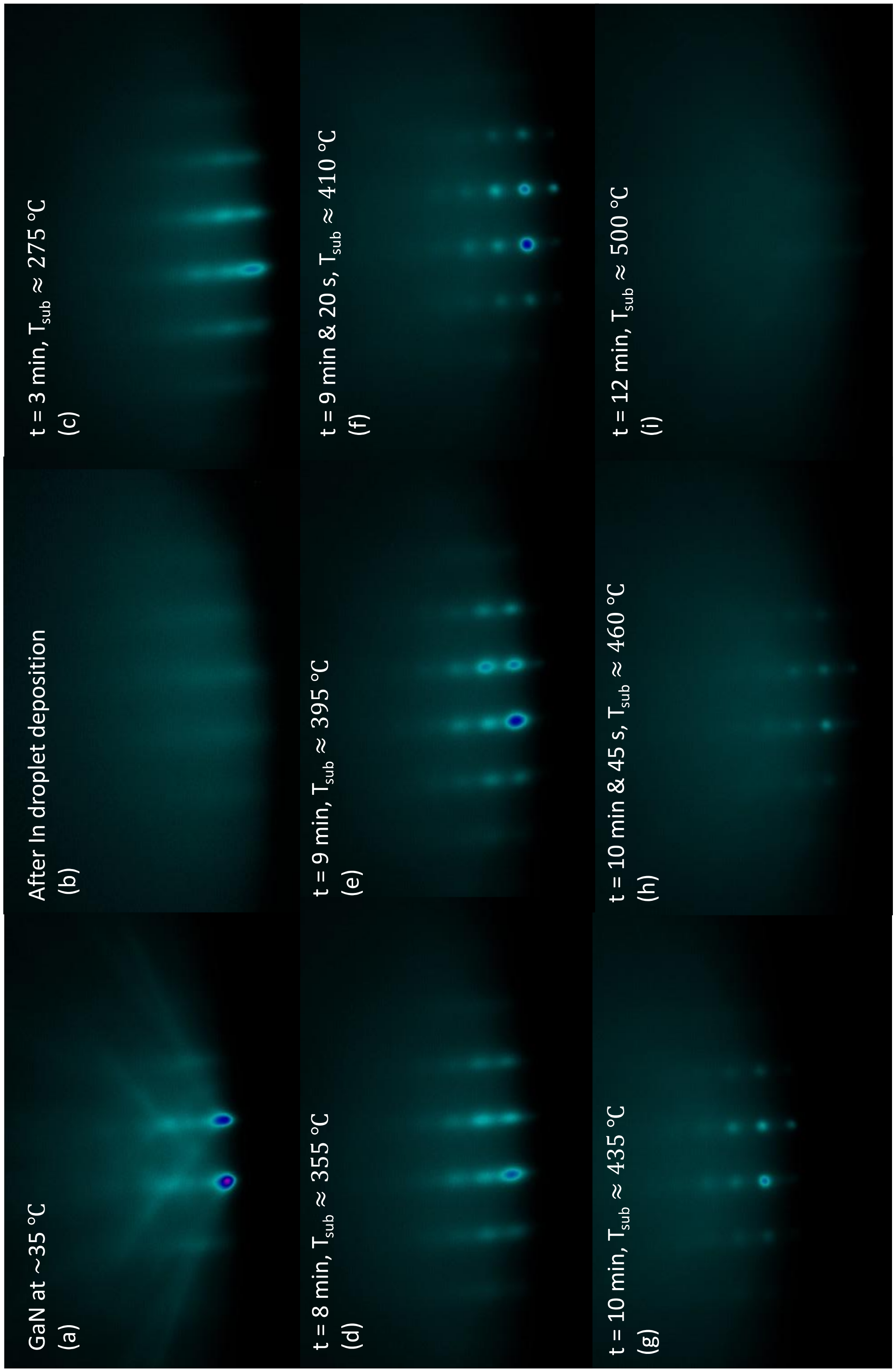

Figure 50: RHEED patterns detected at each phase of the droplet epitaxy InN QDs growth used in the first case.

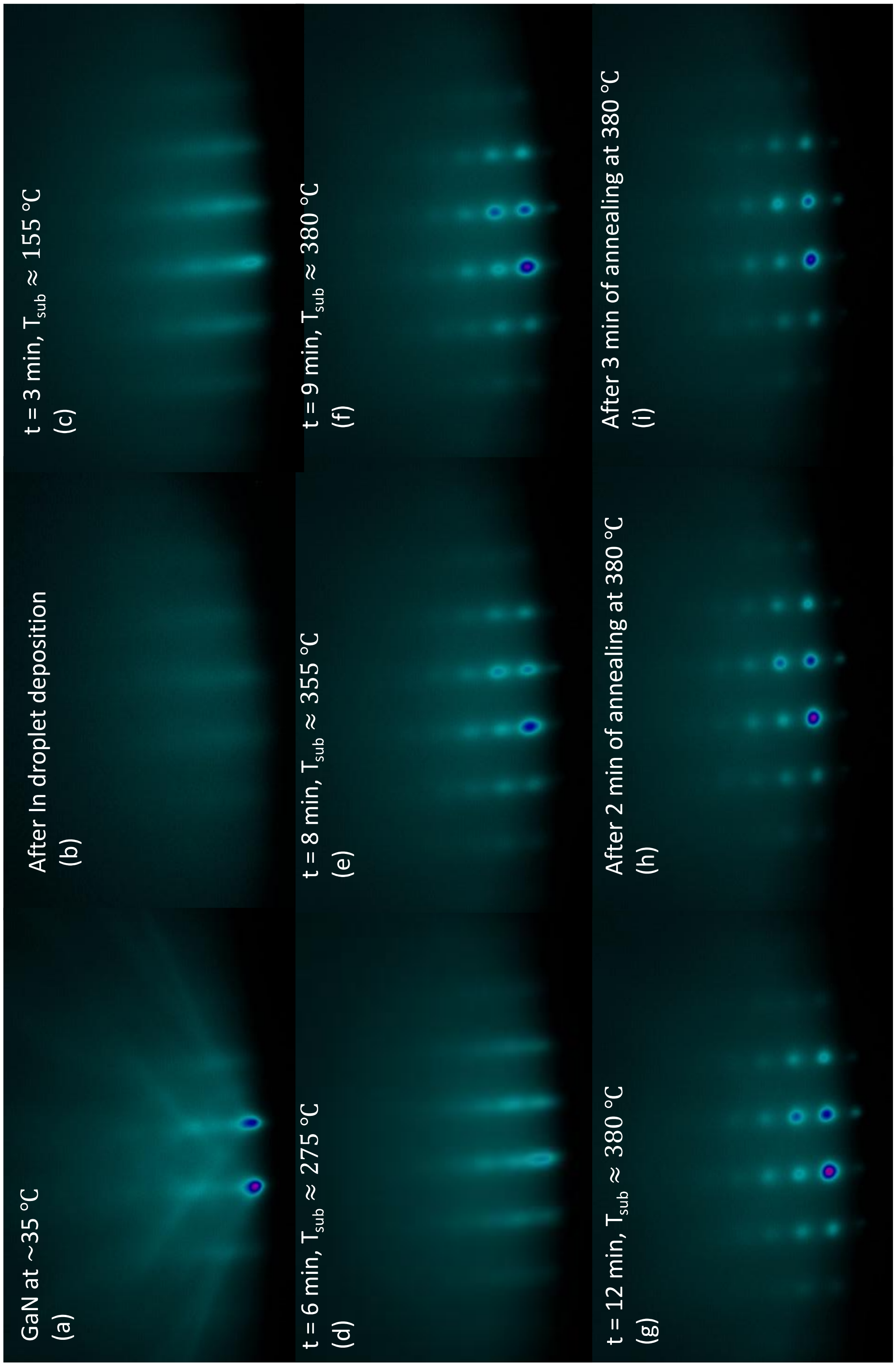

Figure 51: RHEED patterns detected at each phase of the droplet epitaxy InN QDs growth used in the second case.

After 3 min of annealing at 380 °C, the patten stayed clearly spotty without significant degradation (Figure 51 (f)). This is a good indication that all In droplets were completely converted into InN, which was confirmed via XRD from this sample (Figure 52). The diffraction peak appearing at 31.38° is for InN (002) [84]. The position and width of this peak indicate that the wurtzite InN has a bulk relaxed lattice constant and is contained in small nanocrystals or QDs [86]. At the same time, there is a complete absence of a peak at 32.93°, which indicates no residual In. Figure 53 shows (2 × 2) μm AFM images of the InN QDs formed by droplet epitaxy in the second experiment. The AFM showed a high density QDs on the GaN surface which was very encouraging to further investigate the surface morphology.

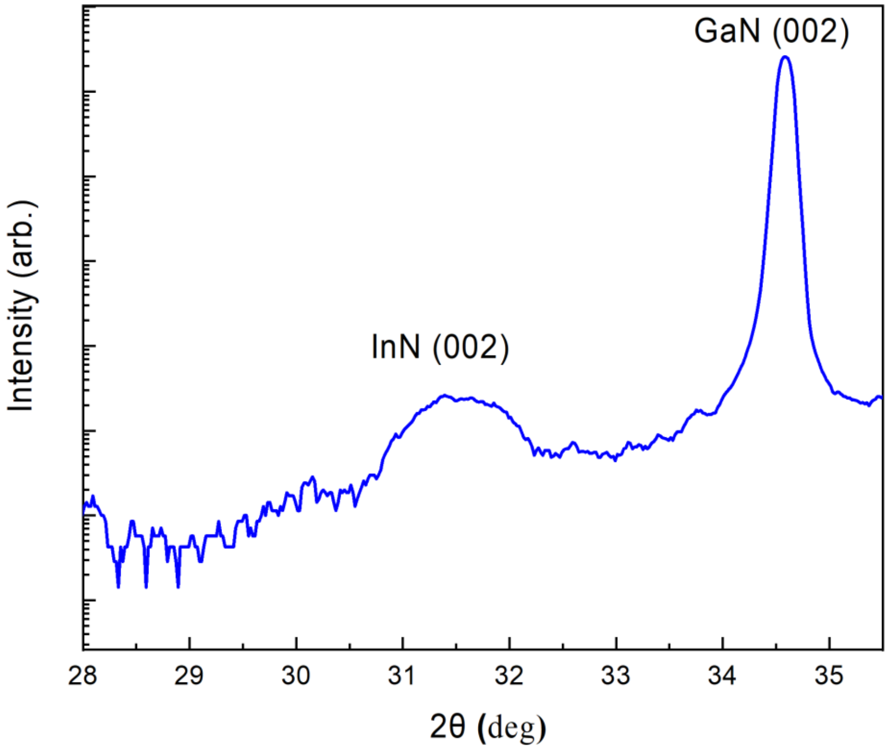

Figure 52: $2\theta/\omega$ XRD pattern of the droplet epitaxy InN QDs growth on GaN via the second case.

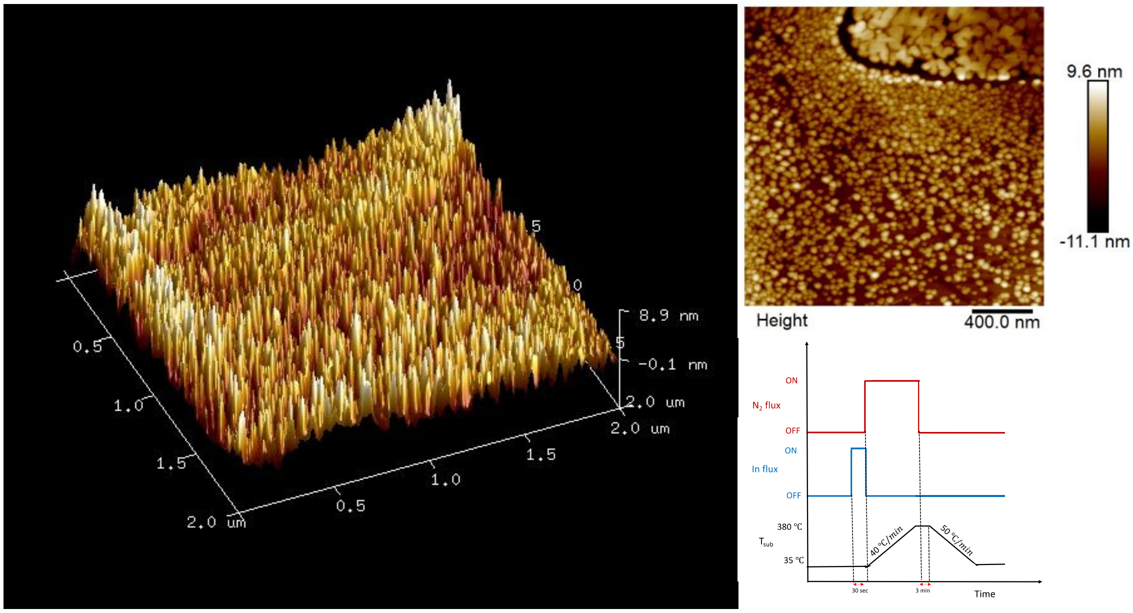

Figure 53: a 3D and 2D AFM images of (2 × 2) μm of the droplet epitaxy InN QDs growth on GaN via the second case.

5.4.2 The Influence of Growth Temperatures on The Formation of InN QDs

In this section, the growth of droplet epitaxy InN QDs on GaN was investigated. Since the substrate temperature has exhibited a significant influence on the density and size of the InAs QDs formed by droplets epitaxy [82], it is assumed that the formation of InN QDs will have a similar result. During the growths, the surface was monitored by an in-situ RHEED system.

5.4.2.1 Experimental Methods

All samples were grown on semi-insulating GaN (0001) templates by MBE. The same substrate preparation process was followed as in previous experiments. After transferring the substrates to the growth chamber, they were heat cleaned for one hour at 830 °C and followed by a 177 nm-thick buffer layer of GaN, grown metal-rich at 795 °C. The GaN buffer layer was then annealed at 795 °C for ~10 min to stabilize the surface and desorb any access Ga. Then, the substrate temperature was decreased to the droplet growth temperature and held constant throughout the deposition of In droplets, which were formed by exposing the substrate to In flux with a BEP of 1.62×10^{-7} Torr for 30 seconds under a nitrogen ambient pressure of ~10^{-5} Torr. Here, the T_{sub} was set to the droplet growth temperature for each sample: 35, 50, 100, 150, 200, and 300 °C. After the In droplet formation, the nitrogen shutter was opened immediately to introduce the RF plasma nitridation, and the substrate temperature was increased to 380 °C at a rate of 40 °C/min for 9 min and followed by 3 min annealing at 380 °C to complete the conversion process. The nitrogen flow rate and plasma power were kept at 0.5 sccm and 350 W whenever active. The crystallization temperature and duration were kept the same for all samples.

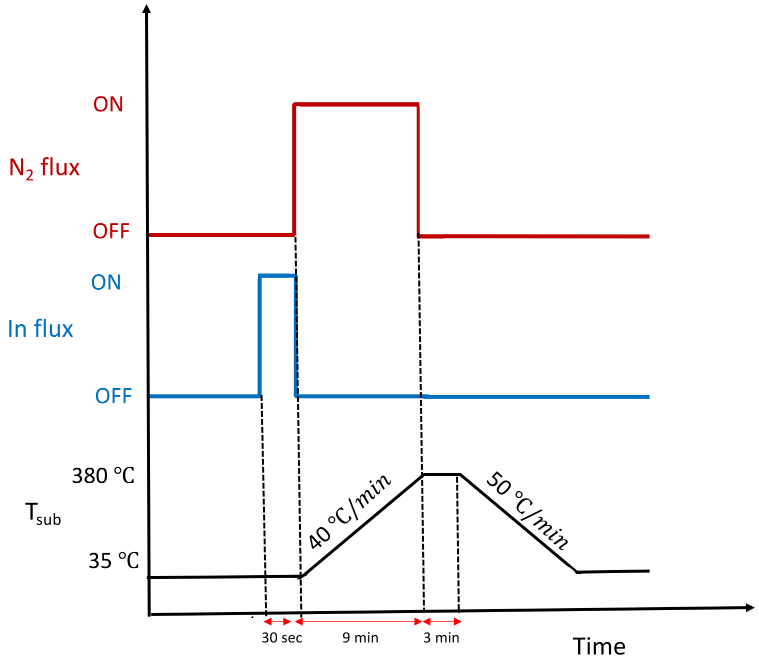

Figure 54: An illustrated of the steps of the formation of droplet epitaxial InN QD on GaN.

An illustration of the steps to form droplet epitaxial InN QDs on GaN is presented in Figure 54. For growth temperatures less than ~100 °C, the substrate was allowed to stabilize for up to 2 hours under constant heater power, so that the surface temperature could reach the low values and that the automatic regulation did not provide any power pulses during growth. In order to prevent the effects of ripening, the samples grown at 150 °C and lower were immediately transferred out of the growth chamber after droplet formation. However, for samples grown at 200 and 300 °C, the substrate temperature was reduced rapidly at 50 °C /min right after finishing each growth. When the substrate temperature reached ~ 100 °C, the samples were taken out of the chamber.

5.4.2.2 Results and Discussion

The key objective of this work was to control the size and density of InN QDs. This was accomplished by controlling the substrate temperature from near room temperature to a high substrate growth temperature with a fixed In droplet growth time of 30 sec and crystallization through ramping to 380 °Cover 9 min, followed by 3 min annealing at 380 °C to complete the conversion process. Figure 55 (a) shows the $2\theta/\omega$ XRD measurements of the droplet epitaxy InN QDs grown at T_{sub} ranging from 35 °C to 300 °C. The diffraction peaks at 31.38° and at 34.57° are assigned to diffraction from the InN (002) [84] and the GaN (002) planes, respectively. The position and width of these peaks indicate that the wurtzite InN has a bulk relaxed lattice constant and since the peaks are very wide, they are likely in small nanocrystals or QDs [86]. At the same time the peak-width for lower growth temperatures appears broader. This is generally an indication of smaller dots. By increasing the substrate growth temperatures, the intensities of the characteristic InN peak declined initially and then improved, demonstrating that the degree of crystallinity decreased at first and then increased as rising the T_{sub} of In droplet. To further investigate the effect of temperature on the crystalized InN QDs, the full width at half maximum (FWHM) of the InN (002) peak is plotted in Figure 55 (b), where it drops first until reaching a T_{sub} of 150 °C and then increases with further increase in temperature indicating a similar, but inverted trend in the QD size, i.e., the largest FWHM corresponds with the smallest QDs.

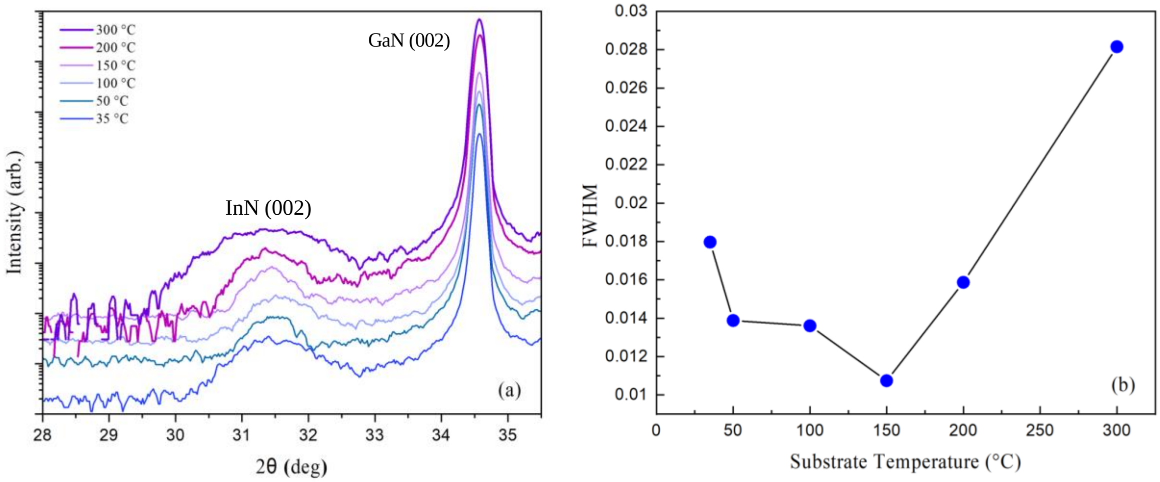

Figure 55: (a) XRD pattern and (b) FWHM of InN QDs at different substrate growth temperatures.

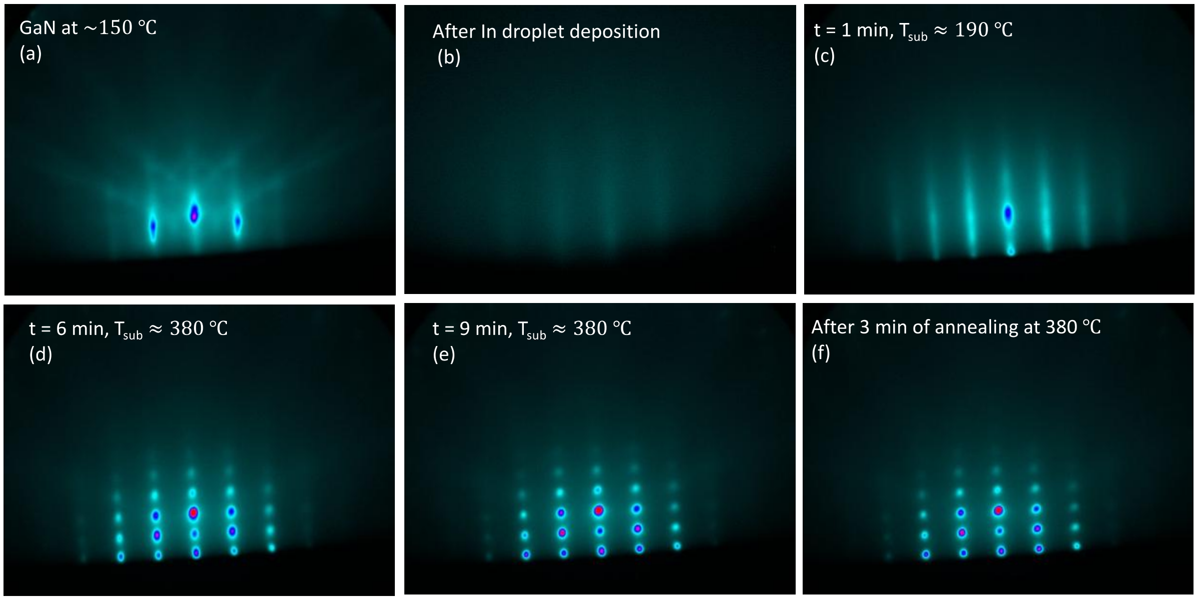

Figure 56: an illustration of the RHEED patterns detected at each period of the droplet epitaxy growth of InN QDs for the sample grown at 150 °C.

In addition, Figure 56 displays the RHEED pattern at each stage of the droplet epitaxy growth of InN QDs for the sample grown at 150 °C. All the samples had shown the transition to spotty patten at ~ 355 °C and became sharp at ~ 380 °C, which is characteristic of the QD formation. The pattern observed from the substrate is normally shadowed during droplet growth.

Also, the sample grown at 150 °C and crystallized at 380 °C showed a significant InN peak in the XRD. This results directly correspond with RHEED observations in that a high intensity and clearly spotty pattern was detected. In fact, the spotty pattern did form after ~6 min of crystallization in that sample.

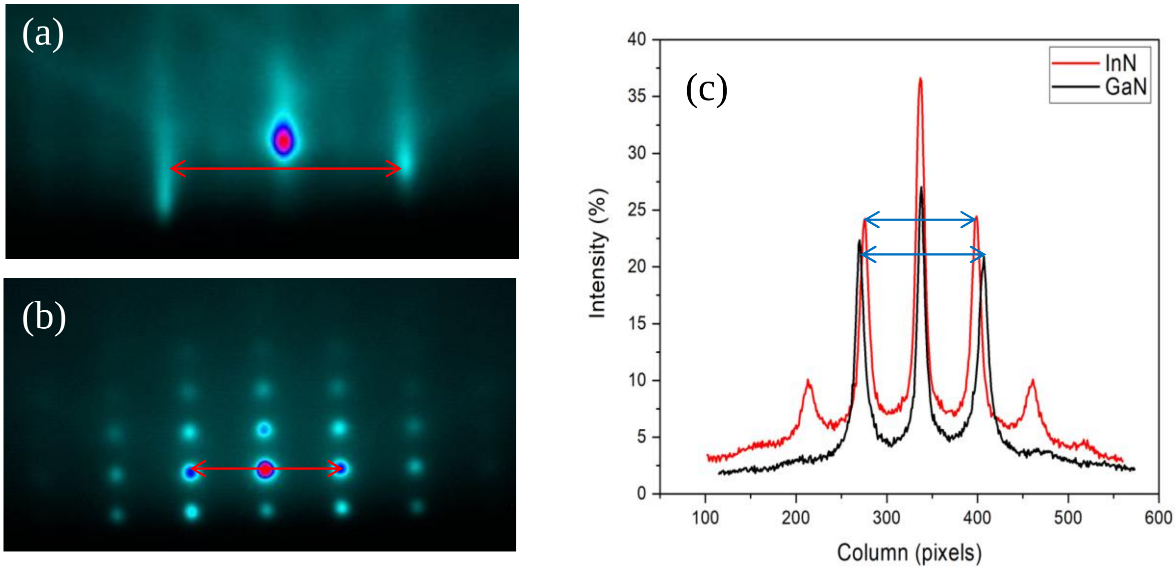

Figure 57: An illustration of RHEED pattern: (a) streaky, (b) spotty, and (c) the intensity profile of data taken from the sample grown at 150 °C and crystallized at 380 °C.

Using the RHEED pattern, the in-plane lattice parameter can be determined by fitting the intensity profile with Gaussian curves and measuring the distance between outside streaks and comparting with that of the spots. Figure 57 shows an example of RHEED pattern: streaky (a) and spotty (b) and the intensity profile with cross-section curves (c) from the data taken from the sample grown at 150 °C and crystallized at 380 °C. The lattice parameter of InN QDs could be obtained using the lattice parameter of GaN (0.319 nm) [112]. It is well known that the spacing in reciprocal space is inversely proportional to that in real space. Therefore, the spacing between GaN peaks (d_{GaN} = 137 pixels) can be compared with that of InN peaks (d_{InN} = 124 pixels) to compute the InN's lattice constant by equation 23 [64]. It was found that the lattice constant of

InN is 0.3524 nm which very close to the reported lattice constant of 0.3044 nm using transmission electron microscopy (TEM) for InN QDs grown on GaN [113].

$$a_{InN} = a_{GaN}\left(\frac{d_{GaN}}{d_{InN}}\right) \qquad \textit{Equation 23}$$

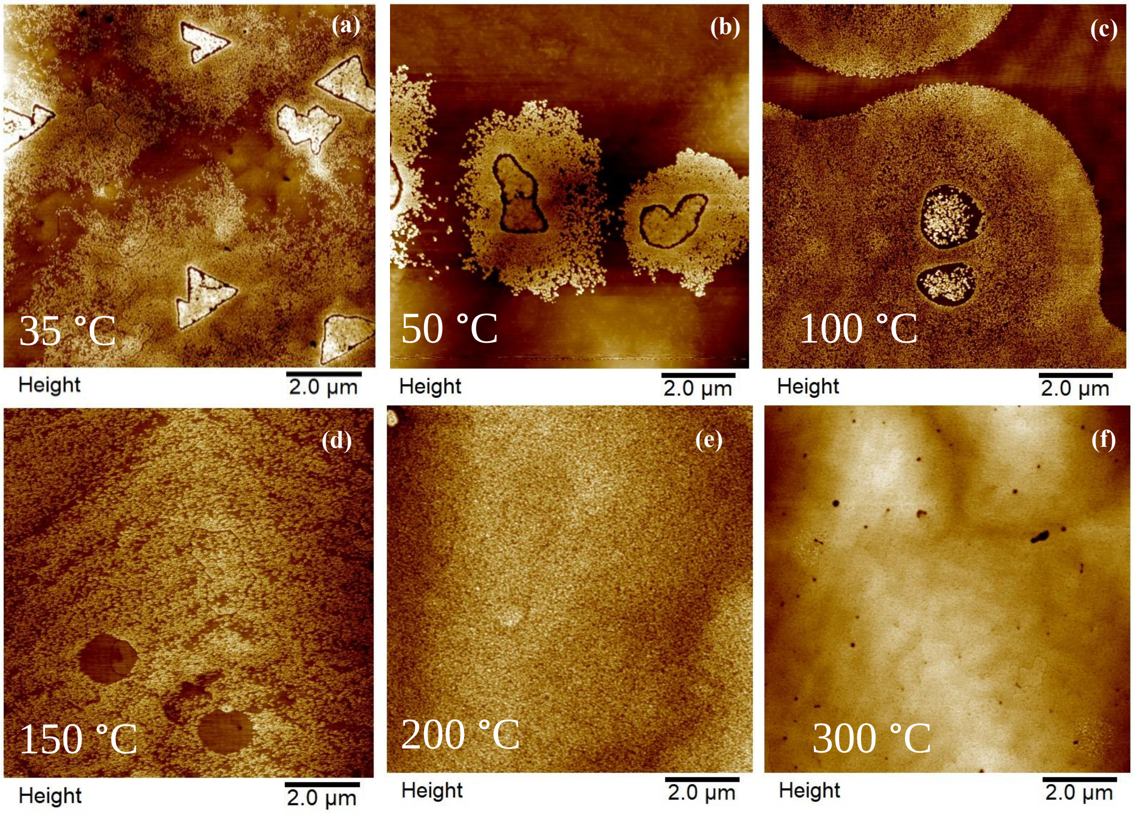

Figure 58: AFM of (10 × 10) μm images of the InN QDs formed at various growth temperatures.

Under the RF plasma nitridation, each In droplet should evolve into an InN nanocrystal. Figure 58 shows (10 × 10) μm AFM images of the InN QDs acquired from crystallizing the In droplets which were formed at the different growth temperatures. For the growth temperatures below the bulk melting point of In, it can be seen that the InN QDs formed ring-like structures (Figure 59 (a), (b), and (c)). The inner ring radius (R_1) can be seen to be similar to the original In droplet sizes, which was also seen to vary with growth temperature. This can be confirmed by comparing the diameter of the inner ring (1740 nm) of the sample gown at 100 °C with the diameter of the In droplet formed under a nitrogen ambient pressure of ~10^{-5} Torr (1488 nm) at the same growth temperature (presented in Figure 60). However, the diameter of ring is consistently larger than the droplet sizes. This is likely due to the initial redistribution of material during the crystallization process. Similar observations were found in GaAs QDs formed by droplet epitaxy [114], [115].

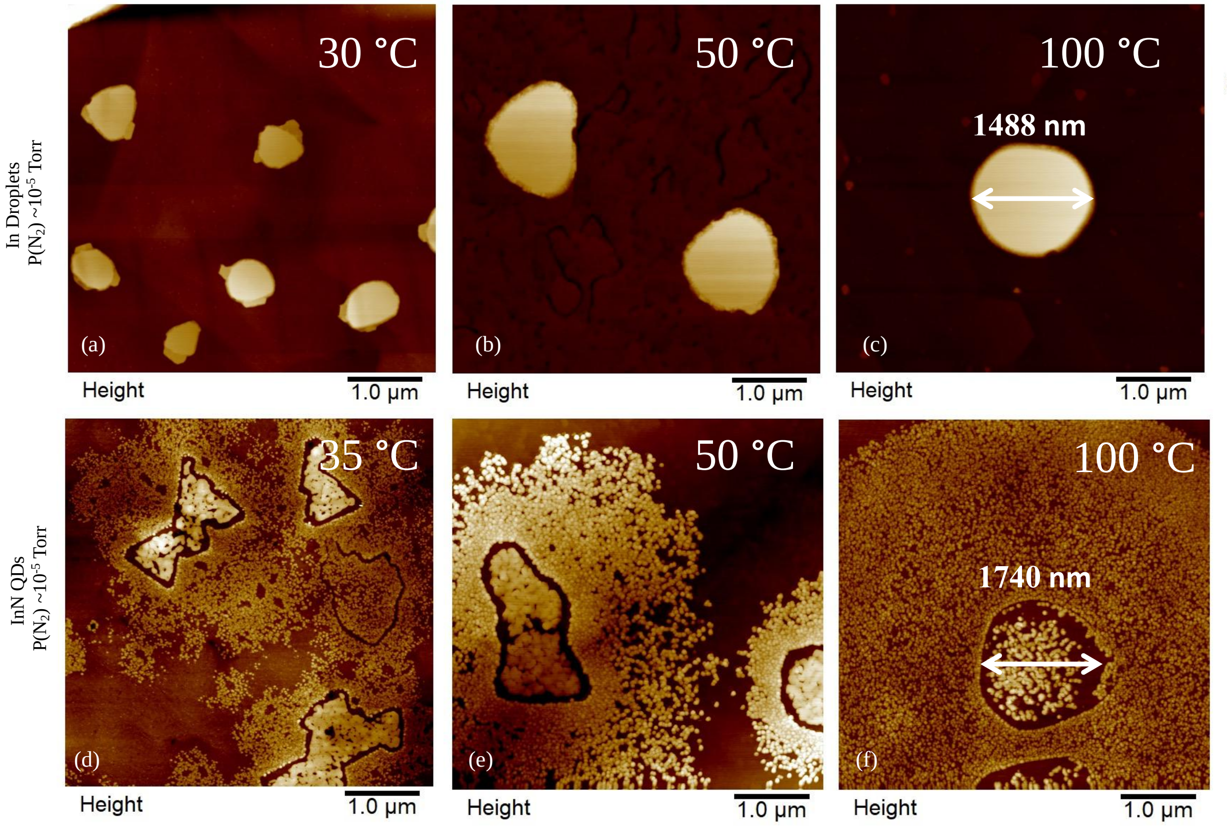

Figure 59: AFM of (5 × 5) μm of the samples grown at ≤ 100 **(°C)** before crystallization and under a nitrogen ambient pressure of ~10^{-5} Torr in (a-c) and after crystallization in (d-f).

Figure 59 shows the In droplets grown under a nitrogen ambient pressure of ~10^{-5} Torr (a-c) and shows the post-nitridated structures (d-f). The material inside the inner rings have diffused out for growth temperatures above 100 °C, and the radius of outer disk has become significantly larger. The inner ring (R_2), which represents the droplet edge, as well as an outer disk radius (R_1) are described in Figure 60 (a). The outer disk radius is obviously dependent on the crystallization conditions. As seen from the morphologies of the samples grown at 200, and 300 °C (Figure 59 (e) and (f)), the outer disk radius is increased with increasing the substrate temperature until forming a nearly thin film at 300 °C. To further evaluate the effect of temperature on the InN QDs grown at 35, 50, and 100 °C, the mean radius (ΔR) was plotted as a function of the inverse temperature, presented in Figure 60 (b). From this Arrhenius plot, the activation energies were determined via exponential fitting, which was found to be -0.38 ± 0.03 eV which is much lower than 0.25 ± 0.10 eV for those formed in ambient N_2, $\sim10^{-5}$ Torr on GaN and in the same growth temperature range. The values of the radius of the inner ring and outer disk along with density, height, and diameter of InN QDs in the outer disk area were stated in Table 4.

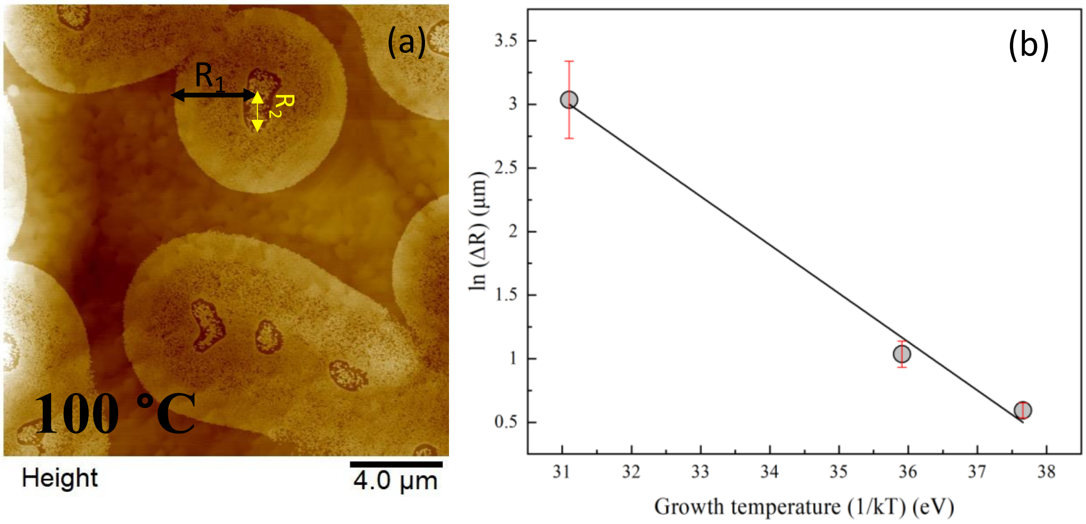

Figure 60: An illustration of the inner ring (R1) and the outer disk radius (R2) (a) and the mean radius (ΔR) versus the inverse temperatures (b).

Generally, there are several features, and possibly even two different sizes of droplets or dots on some of the samples. In what follows, it is focused on the distribution of the dot formed in the outer disk on all samples. Figure 61 displays the cross sections of the droplet epitaxy InN

QDs formed at different T_{sub}. The density, height, and diameter of the InN QDs are plotted as functions of T_{sub} in Figure 61. It can be clearly seen that there is a slightly different variation in the droplet epitaxy InN QDs size and density for samples grown at higher temperatures (150 °C and 200 °C) from those grown at lower temperatures $\leq$ 100 °C. For a high T_{sub} of 200 °C, the size of the QDs was 85.5 nm in diameter and 14.7 nm in height with a density of 3.56×10^{9} cm^{-2}. The diameter of the droplets was further increased from 85.5 μm to 95.1 μm with decreasing T_{sub} from 200 to 150 °C, and the height was increased to 20 nm for the sample grown at 150 °C. Then, the height was reduced to 18 nm, and the diameter was increased to 104.9 nm, when decreasing T_{sub} to 100 °C. At the T_{sub} of 50 °C, the QDs dimensions were considerably dropped to 85.8 nm for the diameter and 17 nm for the height, and the density was increased to 4.20×10^{10} cm^{-2}. This can be due to the decline in adatom diffusion length, caused by the reduction in substrate temperature. With a further decrease of T_{sub} from 50 °C to 35 °C, the QDs dimension continued to decrease, so the QDs dimension was reduced to 11 nm in height and 53.4 nm in diameter, and the density increased to 6.07×10^{10} cm^{-2}.

Table 4: The values of the radius of the inner ring and outer disk along with the density, diameter, and height of InN QDs in the outer disk.

T_{sub} (°C)	Density ($\mathrm{cm^{-2}}$)	Diameter (nm)	Height (nm)	Aspect ratio -	R_2 (μm)	R_1 (μm)	ΔR (μm)
35	6.07×10^{10}	53.4	11	4.85	1.69	1.09	0.59
50	4.20×10^{10}	85.8	17	5.04	1.87	0.83	1.036
100	8.68×10^{9}	104.9	18	5.82	3.88	0.85	3.036
150	4.62×10^{9}	95.1	20	4.75	-	0.63	-
200	3.56×10^{9}	85.5	14.7	5.81	-	-	-

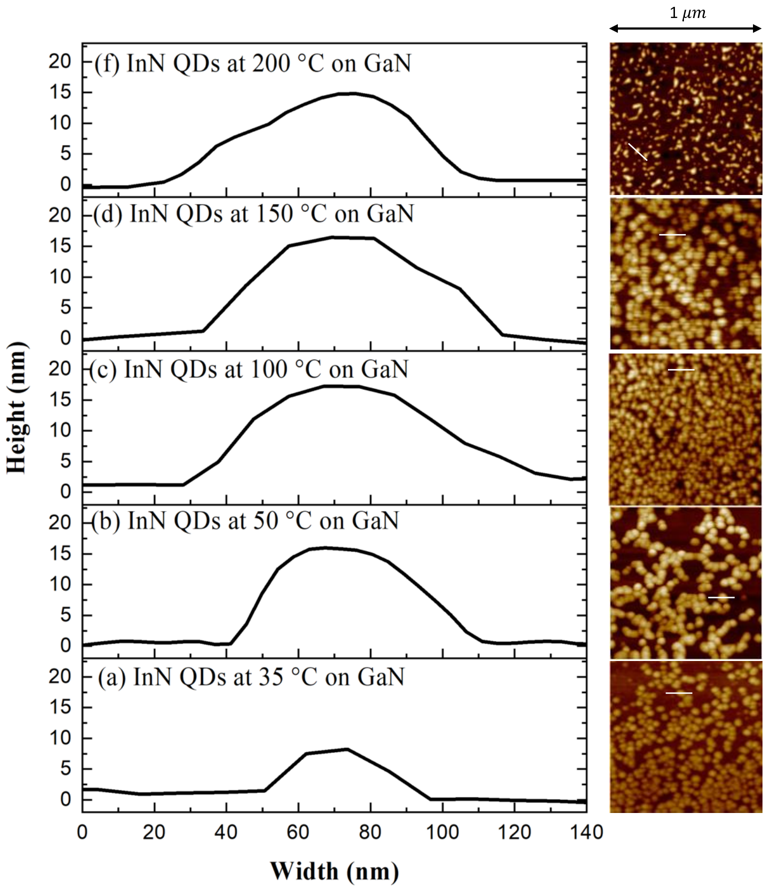

Figure 61: Cross-sectional line profiles of the droplet epitaxy InN QDs grown at different T_{sub}.

Investigation of the aspect ratio of the InN QDs presented in Table 4 (diameter divided by height) showed that as increasing in growth temperatures led to a rise from 4.85 at T_{sub} = 35 °C to 5.82 at T_{sub} = 100 °C. However, it was observed that the aspect ratio then dropped to 4.75 at T_{sub} = 150 °C. Further increase of T_{sub} to 200 °C saw a sudden, increase to 5.81. This observation of improving the aspect ratio at very low temperatures was an indication of the very low diffusion length, and the primary addition of extra adatoms to the top surface of the QDs, whereas further increase in temperature above the In melting point adds primarily to the diameter with less diffusion up the surface of the QDs. Finally, it was seen that the beginning effects of evaporation, which appears to happen primarily at the top of the QDs resulting in a reduction in height [57], [92], [94], [105].

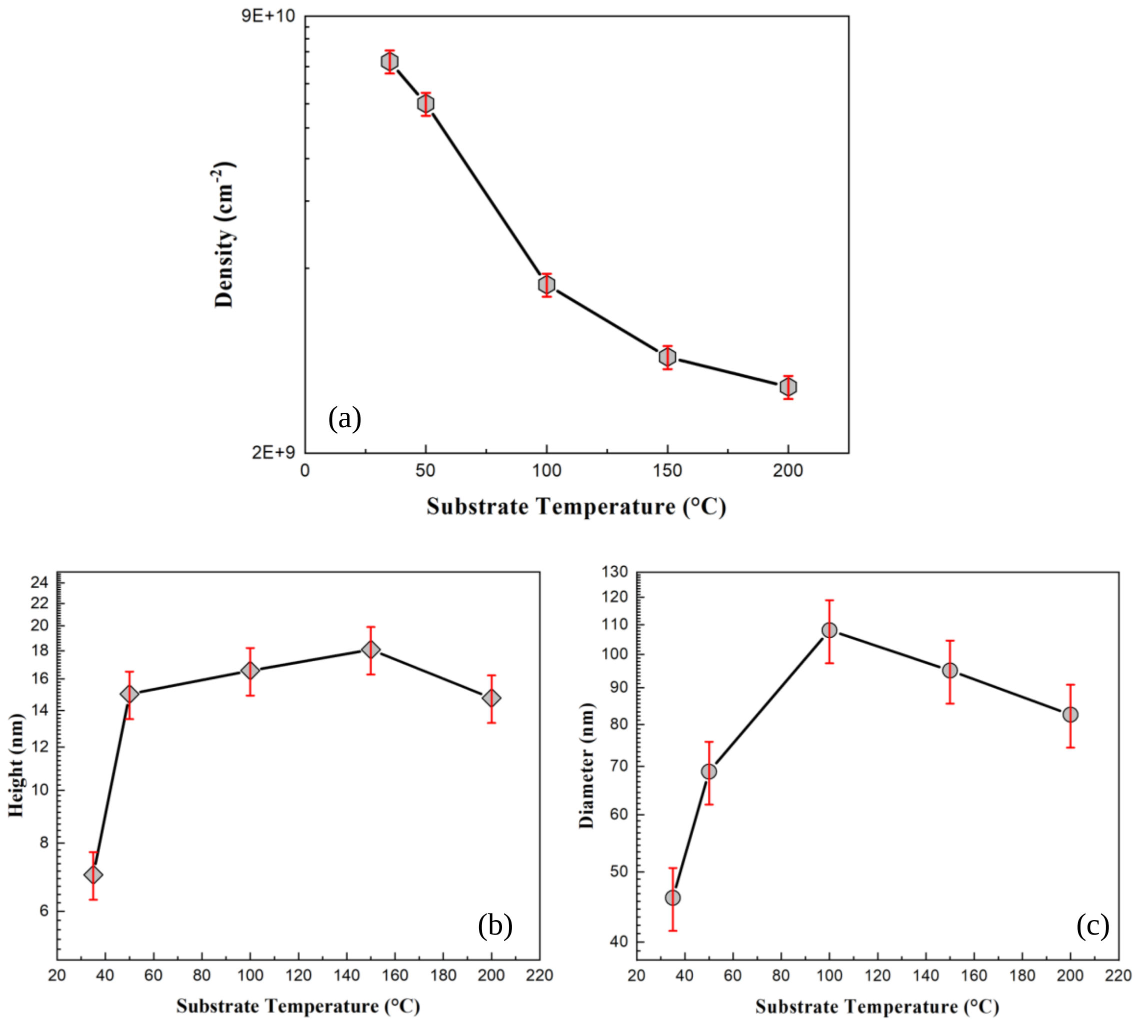

Figure 62: The density (a), height (b), and diameter (c) of InN QDs on GaN.

Figure 63 presents the density of InN nanostructures as a function of the inverse temperature. This is the same data as displayed in Figure 62 (a). From this Arrhenius plot, the activation energy was determined by fitting the data to an exponential function. The resulting activation energy for InN surface diffusion on GaN was found to be 0.23 ± 0.03 eV. In addition, it was found that by analyzing the density of crystallized QDs, which followed the droplet formation under ambient N_2, a very close activation energy of 0.25 ± 0.10 eV (see Figure 45) was found. By comparison, the activation energy for the InAs nanocrystals formed on InP by droplet epitaxy was found to be 0.28 ± 0.01 eV [116], which matches quite well with the activation energy found here for InN QDs. These results also match with a classic nucleation theory, and the density of QDs follows the nucleation scaling law with an increase in temperature and Ostwald ripening [98].

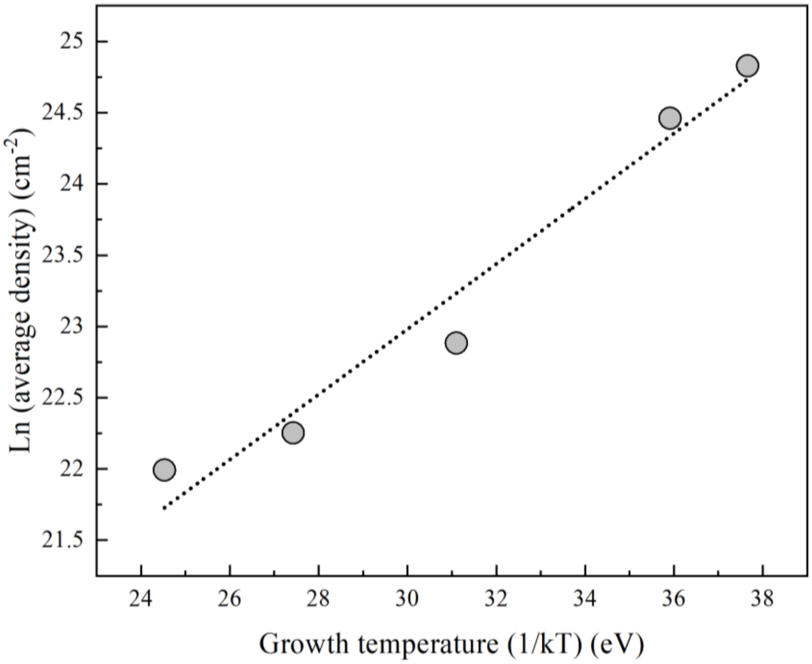

Figure 63: Arrhenius plot of InN QDs density formed on GaN at different growth temperatures (1/kT).

5.4.3 The effect of the crystallization duration on InN QDs.

The influence of the crystallization time on the growth of InN QDs on GaN by droplet epitaxy was investigated. As seen in the previous section, the substrate temperature has a significant influence on the density and size of the InN QDs. Here, both the In droplet growth temperature and the InN crystallization temperature were fixed while the crystallization duration was varied in order to be able to control the size and density of the InN QDs. During the growths, the surface was monitored by in-situ RHEED.

5.4.3.1 Experimental Methods

Here, two samples were grown on semi-insulating GaN (0001) templates by MBE. The same substrate preparation process was followed as in previous experiments. After transferring the substrates to the growth chamber, they were heat cleaned for one hour at 830 °C and followed by a 177 nm-thick GaN buffer layer grown metal-rich at 795 °C. The GaN buffer layer was then annealed at 795 °C for ~10 min to stabilize the surface and desorb any access Ga. Then, the substrate temperature decreased to 35 °C and held constant throughout the deposition of In droplets. The In droplets were formed by exposing the substrate to In flux with a BEP of $1.62{\times}10^{-7}$ Torr for 30 sec after pumping the nitrogen from the chamber and achieving a pressure of less than 10^{-9} Torr to reduce the effect of the nitrogen. Then the samples were taken out of the growth chamber immediately after the droplets formation on order to reduce the influence of the substrate temperature until the nitrogen ambient pressure reached $\sim 10^{-5}$ Torr. The samples were then transferred back to the growth chamber to crystalize the droplets.

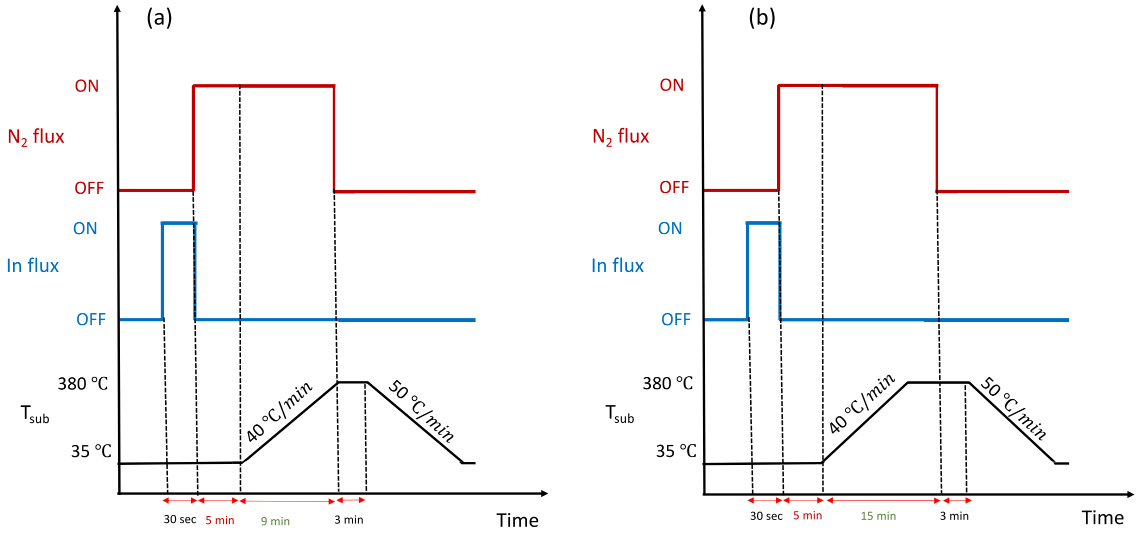

Figure 64: An illustration of the InN QDs growth procedures at shorter (a) and longer (b) crystallization duration.

The crystallization process was completed in two steps. In the first step, the nitrogen shutter was opened immediately to introduce the RF plasma nitridation for 5 min at 35 °C to reduce the effect of diffusing and Ostwald ripening, and then the substrate temperature was increased to 380 °C at a rate of 40 °C/min for 9 min and followed by 3 min annealing at 380 °C to complete the conversion process as was accomplished in the first sample (NL 221). In the second sample (NL 222), the same process was followed as in the previous sample except in the second step of the crystallization. After crystallizing the droplet at 35 °C for 5 min, the substrate temperature was increased to 380 °C at a rate of 40 °C/min for 9 min and continued the crystallization at 380 for ~ 6 min. Then, the InN QDs was annealed at 380 °C for 3 min. The nitrogen flow rate and plasma power were kept at 0.5 sccm and 350 W whenever active. An illustration of the InN QD on GaN growth steps is presented in Figure 64.

5.4.3.2 Results and Discussion

Figure 65 shows the $2\theta/\omega$ XRD measurements of the droplet epitaxy InN QDs grown at 35 °C under ultra-high vacuum, 10^{-9} Torr, and crystallized at 380 °C for two different times. The peaks at 31.38° and at 34.57° are assigned to diffraction from the InN (002) [84] plane and the GaN (002) planes, respectively. The position and width of this peak indicate that the wurtzite InN has a bulk relaxed lattice constant and is contained in small nanocrystals or QDs [86]. As it is shown below, the XRD peaks for shorter crystallization time appear broader, which is a general indication of smaller dots. By increasing the crystallization time, the intensities of the characteristic InN peaks improved, demonstrating that the degree of crystallinity increased. These results directly correspond with RHEED observations in that a high intensity and clearly spotty pattern was detected in the sample crystallized for longer time. To further investigate the effect of crystallization duration on the InN QDs, the full width at half maximum (FWHM) was calculated, and its values went up from shorter crystallization time to longer one. The FWHM values varied from 0.0097 to 0.0113 for samples crystallized for shorter time (14 min) and longer time (20 min), respectively. This demonstrated that the crystal size is improved as the crystallization duration increases.

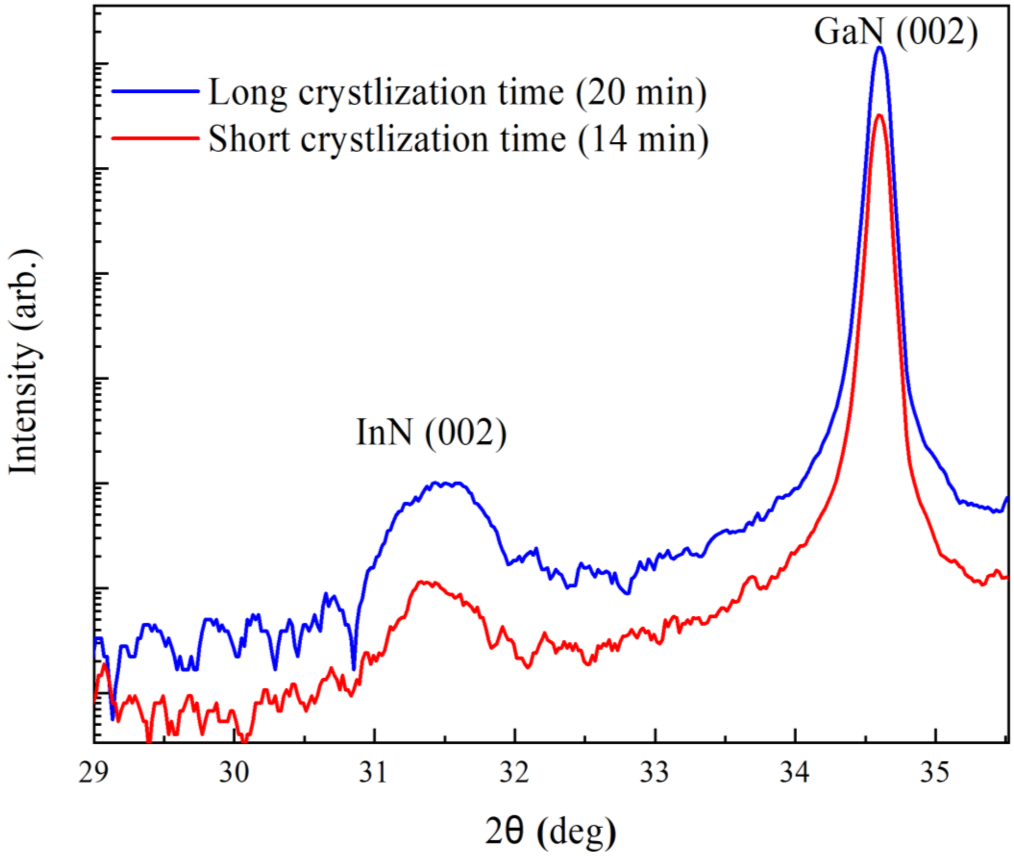

Figure 65: $2\theta/\omega$ XRD pattern of the droplet epitaxy InN QDs on GaN for two different crystallization durations.

Figure 66 shows the RHEED pattern of the GaN before the droplet growth (streaky pattern) and after crystallization for both samples: (a-b) for short crystallization time and (c-d) for long crystallization time. The GaN substrate displays a quite decent RHEED pattern as seen in both samples (Figure 66 (a) and (c)). After depositing the In droplets, the RHEED patterns shadowed. During the crystallization process, the transmission spots were detected for both samples (Figure 66 (b) and (d)). In the samples crystallized for short time (14 min), the RHEED pattern formed a spotty and foggy pattern as seen in Figure 66 (b) demonstrating a formation of nanocrystals and the amorphous thin film.

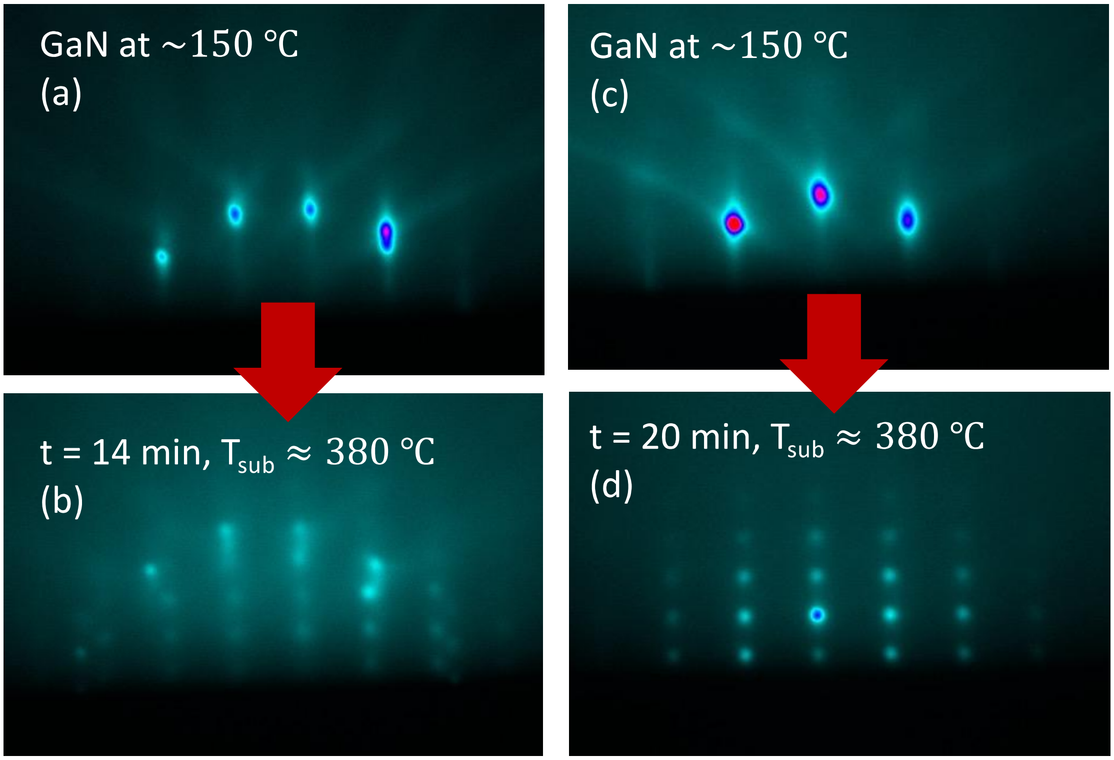

Figure 66: RHEED pattern of InN QDs grown on GaN using two different crystallization times.

Figure 67 shows the AFM of $(10 \times 10)\ \mu m$ images of InN QDs acquired from crystallizing the In droplets using two different crystallization times. As clearly noticeable in the AFM images, the InN QDs crystallized for a shorter time formed spherical dots (Figures 69 (a)). It was observed that the crystallization at low temperature for 5 min prevented the formation of the ring-disk. However, when increasing the crystallization time at higher temperature the ring-disk like structures appeared again (Figure 67 (b)). The spherical dots were converted into a cornered crystallite resulting from crystallization at the droplet edges [117]. By comparing the average diameter of the inner ring (1301.6 nm) of the sample crystallized for longer time at 380 °C with the average diameter (1168.8 nm) of the sample crystallized for shorter time at 380 °C, the diameter of inner ring was quite larger than the InN QDs crystallized for shorter time due to the initial redistribution of material during the crystallization process and by extending the crystallization time at a higher temperature, the uncrystallized In atoms diffused out of the dots and crystallized as smaller dots on the surface [114], [115].

Table 5: the diameter, height, and density of InN QDs crystallized for two different times.

Crystallization time (min)	**Density (cm^{-2})**	**Diameter (nm)**	**Height (nm)**	**Aspect ratio -**
14	3.90×10^{7}	680.171	39.541	17.20
20	1.90×10^{10}	56.33	7.697	7.31

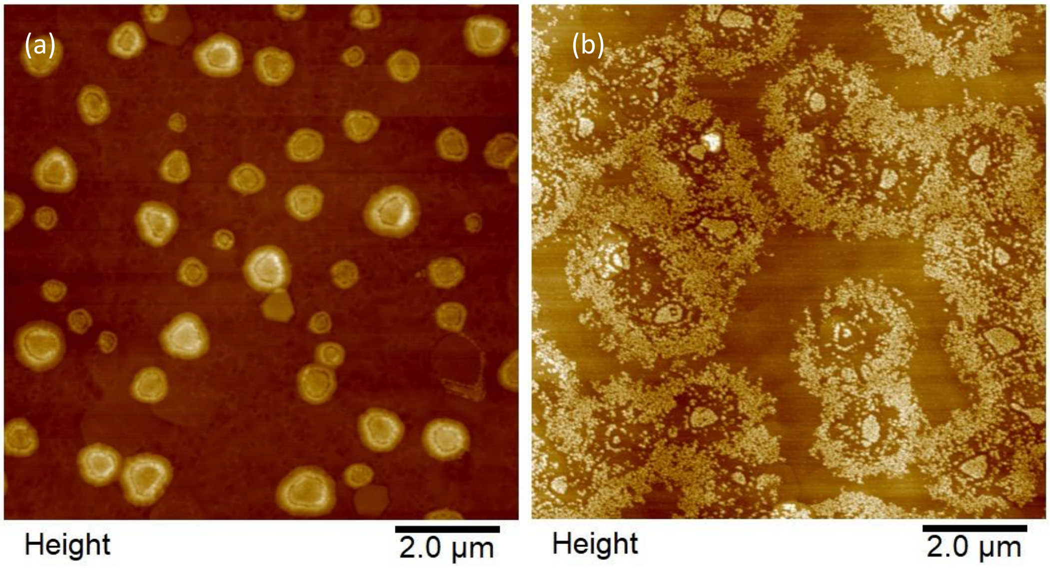

Figure 67: AFM of (10 × 10) μm images of the InN QDs formed using two different crystallization times.

In what follows, the focus is on the distribution of the dot formed in the outer disk in the sample crystallized for longer time at 380 °C. Figure 68 shows cross sections of the droplet epitaxy InN QDs formed for two different nitridation times. From Figures 68 and 69, it can be clearly seen that there is a significant difference in the size and density of the QDs after exposure to the nitrogen plasma for different times. For a short nitridation time, the size of the QDs was 680 nm in diameter and 39.5 nm in height with a density of 3.90×10^{7} cm^{-2} while the diameter and height of the QDs was significantly reduced to 56.3 nm and to 7.70 nm for the longer nitridation time. However, the density increased by almost three orders of magnitude to 1.90 ×

10^{10} cm^{-2} for the longer time. Table 5 summarizes the diameter, height, and density of InN QDs crystallized for two different times. Investigation of the aspect ratio of the InN QDs presented in Table 5 (diameter divided by height) showed that increasing the crystallization time led to a decrease from 17.20 to 7.31. This observation of decreasing the aspect ratio for longer crystallization time was an indication of the very high decomposition.

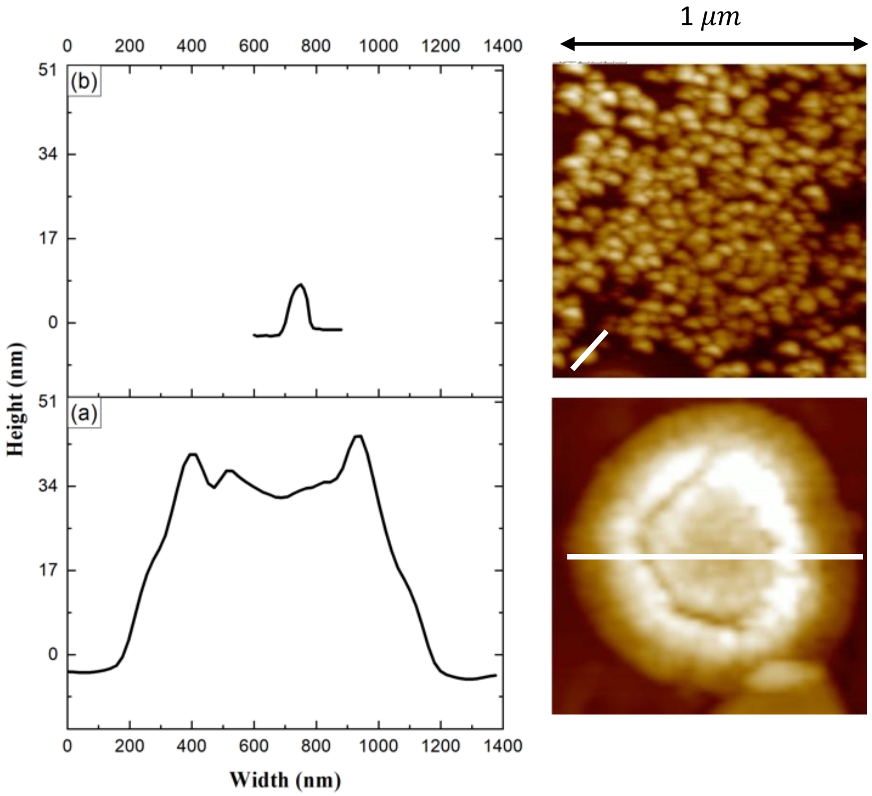

Figure 68: Cross-sectional line profiles of the droplet epitaxy InN QDs crystallized for two different time.

5.5 Capping the InN QDs with GaN layer

In order to utilize the InN QDs as an active layer in any device, the QDs were capped with a GaN layer. GaN has traditionally been formed with substrate temperatures varying from ~ 650 °C to ~ 800 °C. This temperature is exceptionally high for InN, which would decompose the InN QDs immediately. Therefore, the effect of capping the InN QDs with low temperature (LT)

GaN layer was investigated.

5.5.1 Experimental Methods

Three samples of InN QDs formed on the GaN buffer layer were capped with various capping procedures. A graphic illustration of the structure of the three samples is presented in Figure 69. All three samples followed the same preparation methods used in the previous sections. In the first two samples, the InN QDs were formed using the same procedure to grow sample NL 221. After the formation of InN QDs, two different approaches were applied to cap these QDs.

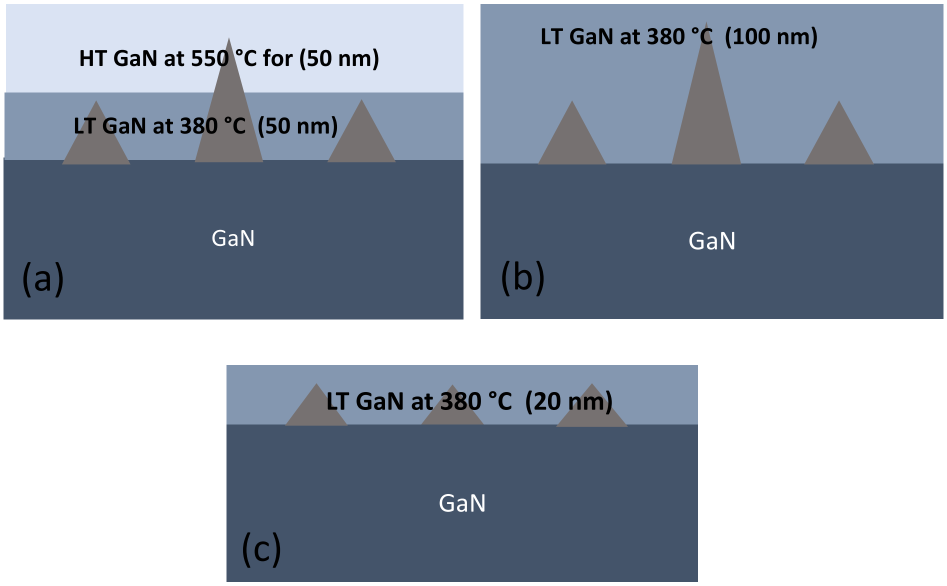

Figure 69: A graphic illustration of the structure of the capped InN QDs.

In the first sample (NL 227) (Figure 69 (a)), to overcome the decomposition of InN, a double GaN layer was grown. The InN QDs were first capped with a 50 nm low temperature (LT) GaN-capped layer to protect the dots and stop the decomposition, which can occur at a high temperature. The LT GaN layer was deposited at 380 °C. The growth temperature was increased, and another 50 nm GaN was deposited at 550 °C to enhance the quality of the capped layer. In the second sample (NL 231) (Figure 69 (b)), after growing the InN QDs, a 100 nm LT GaN capped layer was grown at 380 °C to ensure covering the grown all the dots and to prevent the decomposition.

However, the third sample (NL 232) (Figure 69 (c)) was intended to grow a relatively thin GaN cap layer, so small QDs were grown on GaN by depositing the In droplets by exposing the substrate to In flux with a BEP of 1.62×10^{-7} Torr for 30 seconds under a nitrogen ambient pressure of ~10^{-5} Torr at 35 °C. Next, the sample was transferred out of the growth chamber for around 10 min to reduce the In cell temperature since the shutter was broken. After transferring the sample back to the growth chamber, the nitrogen shutter was opened immediately at 35 °C to introduce the RF plasma nitridation and the substrate temperature was increased to 380 °C at a rate of 40 °C/min for 9 min and followed by 3 min annealing at 380 °C to complete the conversion process. These InN QDs were capped by a 20 nm LT GaN capped layer at 380 °C.

5.5.2 Results and Discussion

Figure 70 presents the AFM of (5 × 5) μm images of uncapped InN QDs (a-b) and InN QDs with GaN capping layer via various approaches (c-f). As seen in sample NL 227 (Figure 70 (c)), the surface morphology formed a reasonably smooth surface with dot density lower than the uncapped sample (NL221, Figure 70 (a)), which is most probably related to the increase in the diffusion length of indium atoms, and the desorption of indium raised at high capping temperature. When a thick (100 nm) low temperature (380 °C) GaN cap layer was deposited on InN QDs (Figure 70 (d)), the surface became rough with the reforming of a ring disk-like structure, which was most likely due to spending a long time at 380 °C during the GaN capping deposition causing the bigger InN dots to be destroyed. Moreover, since the GaN capped layer was deposited at 380 °C, a relatively low temperature compared to its traditional substrate growth temperature ranging from ~650 °C to ~800 °C, this low growth temperature could be the cause of the surface roughness due to low nitrogen supply. Figure 70 (f) is for a thin LT (380 °C) GaN cap layer grown on a high density and small InN QDs (sample NL 232) and it was observed a rough surface with large dots, which could be related to InN QDs. Hence, the InN QDs whose height lower than the GaN cap layer's thickness were still noticeable even after capping. Also, the grown GaN capping layer at much lower temperatures than its appropriate high growth temperature caused a significantly low-quality layer, increasing surface roughness.

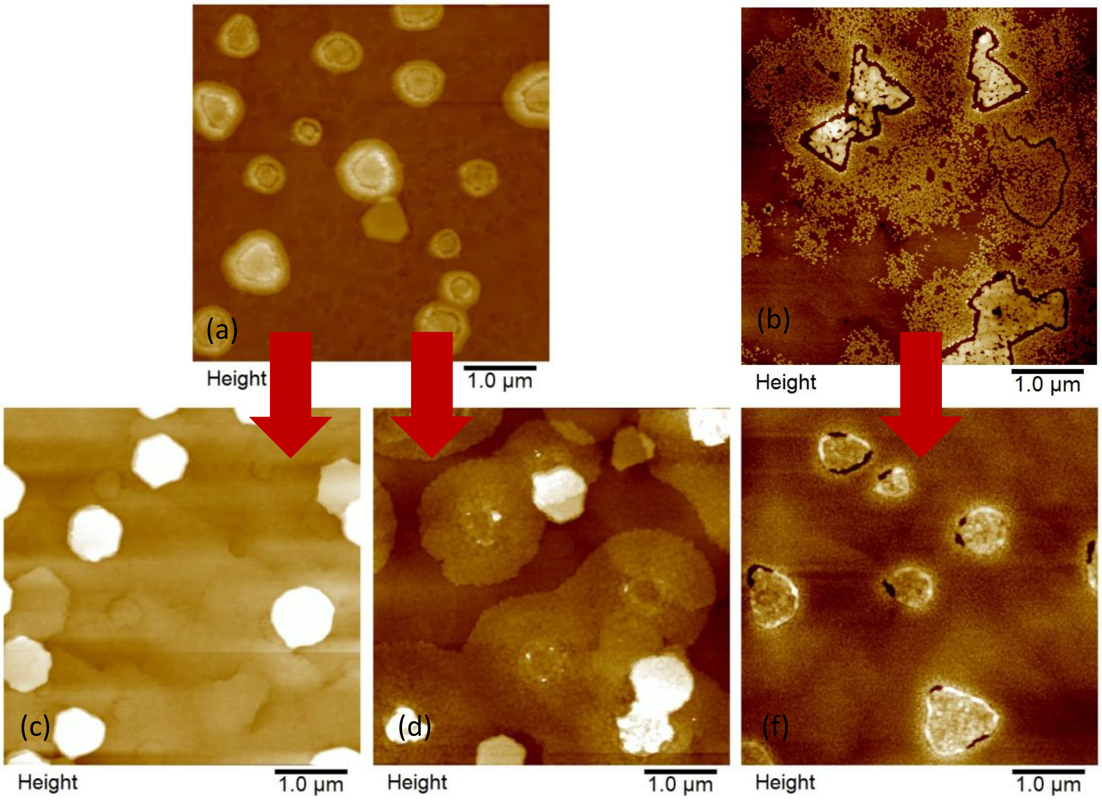

Figure 70: AFM images of uncapped InN QDs (a-b) and capped InN QDs via various approaches (c-f).

Figure 71 shows the $2\theta/\omega$ XRD measurements of the droplet epitaxy InN QDs capped with GaN layer using three procedures. The diffraction peaks at 34.57° were assigned to the wurtzite structure of GaN (002). There were not any peaks detected for InN nor In. Many reasons can explain the disappearance of the InN peak, such as the formation of an amorphous GaN layer covering the InN or the decomposition of InN during the capping process.

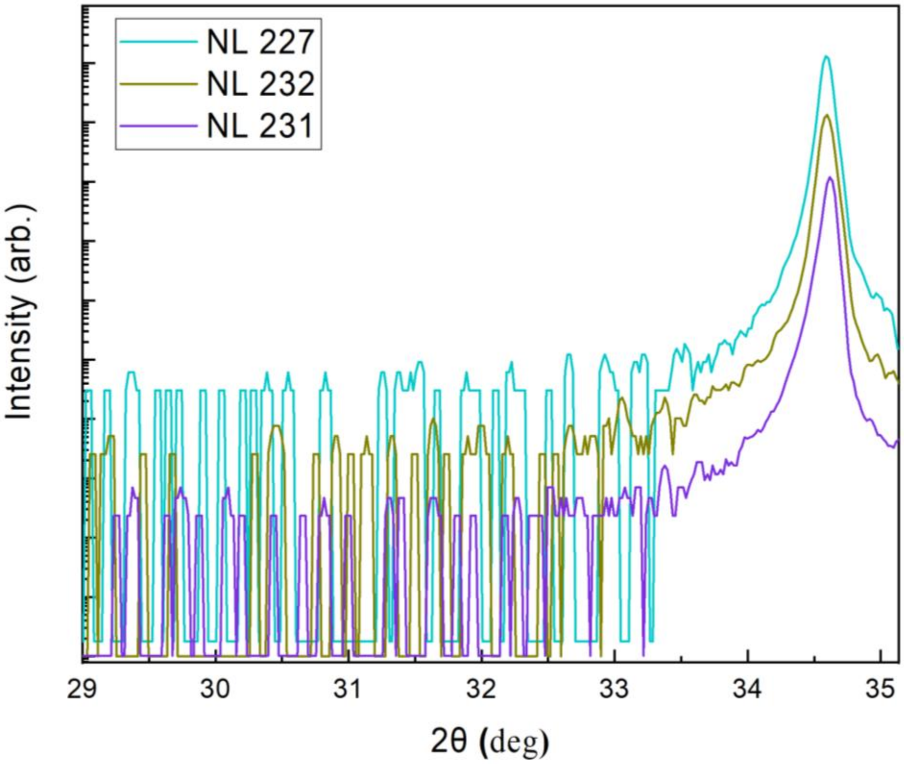

Figure 71: XRD measurements of InN QDs capped with GaN layer using three different procedures.

The elemental composition of GaN capping layers was investigated via energy dispersive X-ray (EDX). Figure 72 shows the EDX map of the entire SEM image in order to explore the dots and the underlying film. Figure 72 (a) and (b) confirm a high ratio of indium element inside the dot and indium intermixing with gallium in the underlying film with a lower percentage of nitrogen inside the dot. However, the indium was observed inside the dot, and it was clearly separated from the gallium in the underlying film with the presence of a higher nitrogen ratio in the dot. This indicated the presence of InN QDs on the surface of the GaN capping layer in Figure 72 (c). In addition, Figure 72 (d) presented the EDX spectra of the spherical shape and the surrounding surface of three different samples. All three samples displayed the presence of InN on the GaN buffer layer.

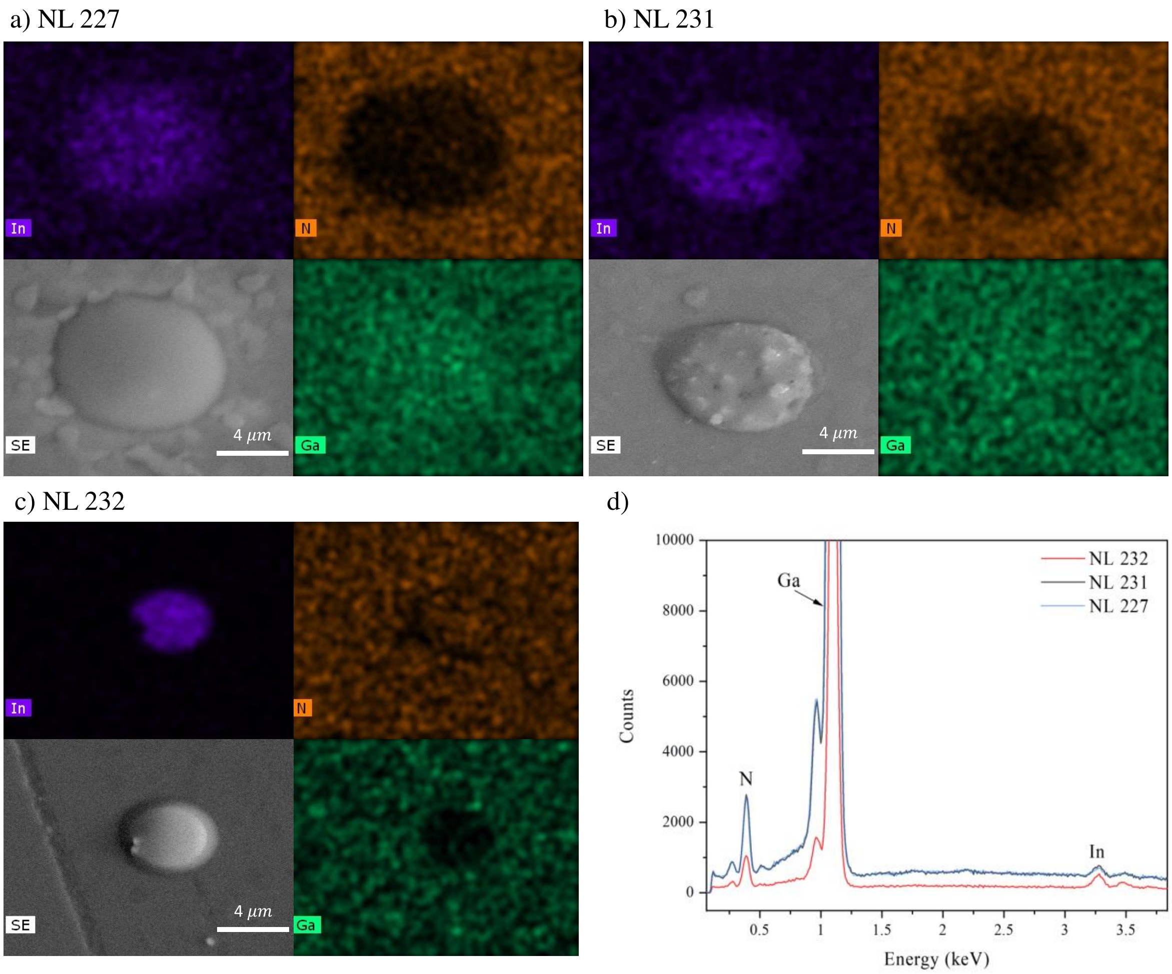

Figure 72: SEM images and the EDX mapping results of the grown GaN capped layer on InN QDs of three different samples: a) NL 227 b) NL 231 and c) NL 232, and EDX spectra of the spherical shaped and surrounding surface.

Raman spectroscopy was used to investigate the crystallinity of InN QDs and the LT GaN-capped film. Raman spectroscopies were accomplished at room temperature in a backscattering configuration. A 632.8 nm helium–neon (He-Ne) laser was utilized with 5 mW power. Figure 73 represents the Raman spectra for different GaN cap layers grown using diverse temperatures and thicknesses, along with a spectrum acquired from an uncapped InN QD and a semi-insulating GaN substrate. All Raman spectra were obtained from the formed dots on the surface. All samples exhibited an intense Raman spectrum of GaN E_2 (high) mode at 570 cm^{-1}

and GaN E_1 (TO) phonon at 560 cm^{-1}. Besides the GaN peaks, a spectrum was obtained from the uncapped InN QDs sample at around 490 cm^{-1} for InN E_2 (high) phonon. The Raman spectra obtained from the thick HT/LT GaN cap layer (NL 227) demonstrated a broad peak of A_1 (LO) phonon at around 700 cm^{-1}, which could correspond to a relaxed InGaN [118]. In thick HT/LT GaN cap layer sample, it was not clear what cause the formation of InGaN. One guess was that the LT GaN layer could not covered all InN QDs leading to the formation of the InGaN layer at a higher temperature cap layer growth. However, the other two samples did not show any shift for InN or InGaN in the Raman spectroscopy.

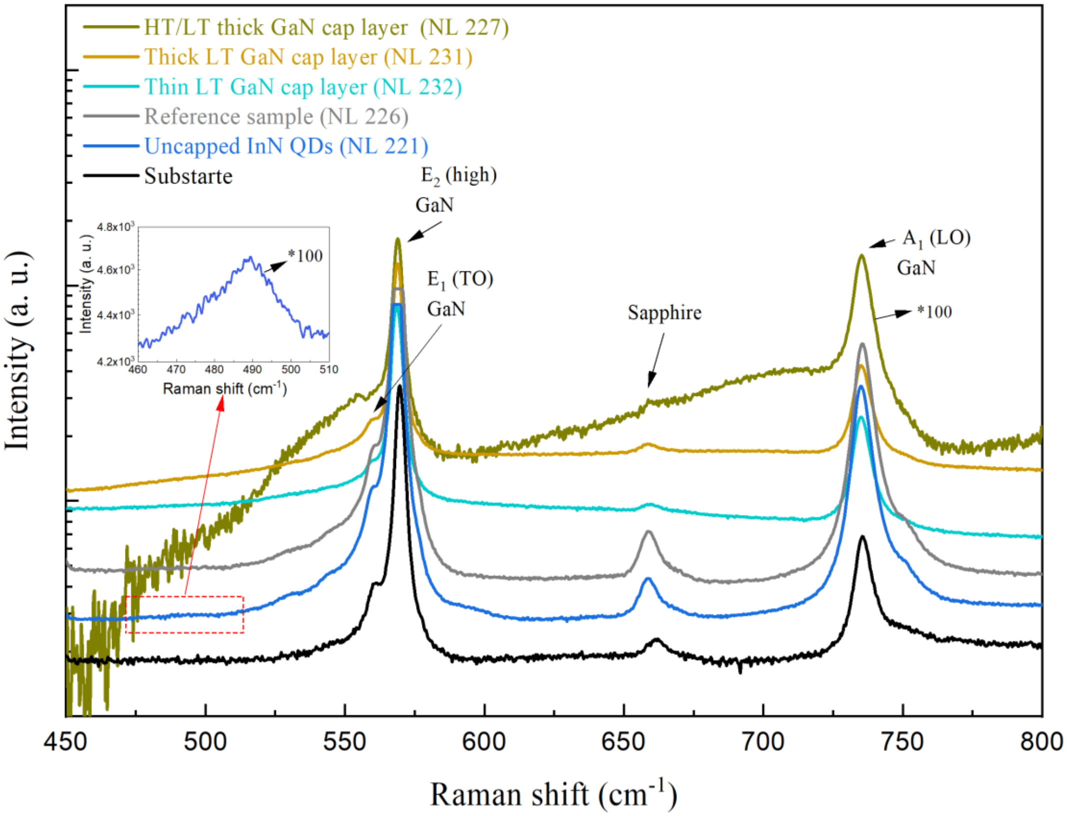

Figure 73: Raman spectroscopy measurement for capped InN QDs with GaN grown at different temperatures and thickness.

The PL measurements were performed to examine the optical quality of the capped InN QDs. A 632.8 nm He-Ne laser was utilized to excite the samples. PL emission was detected via

Si detector for the range from 650 nm to 1000 nm and a single channel, extended range InGaN detector for the range from 1000 nm until 2200 nm at room temperature and 77 K.

Figure 74 exhibits the PL measurements at 77 K of uncapped InN QDs and a reference sample of 1 μm InN film grown on GaN. A very week, narrow signal was detected at 0.68 eV from the uncapped InN QDs, which is well within the range of the observed band-to-band emission of the reference InN film centered at 0.70 eV. However, none of the other samples showed this response.

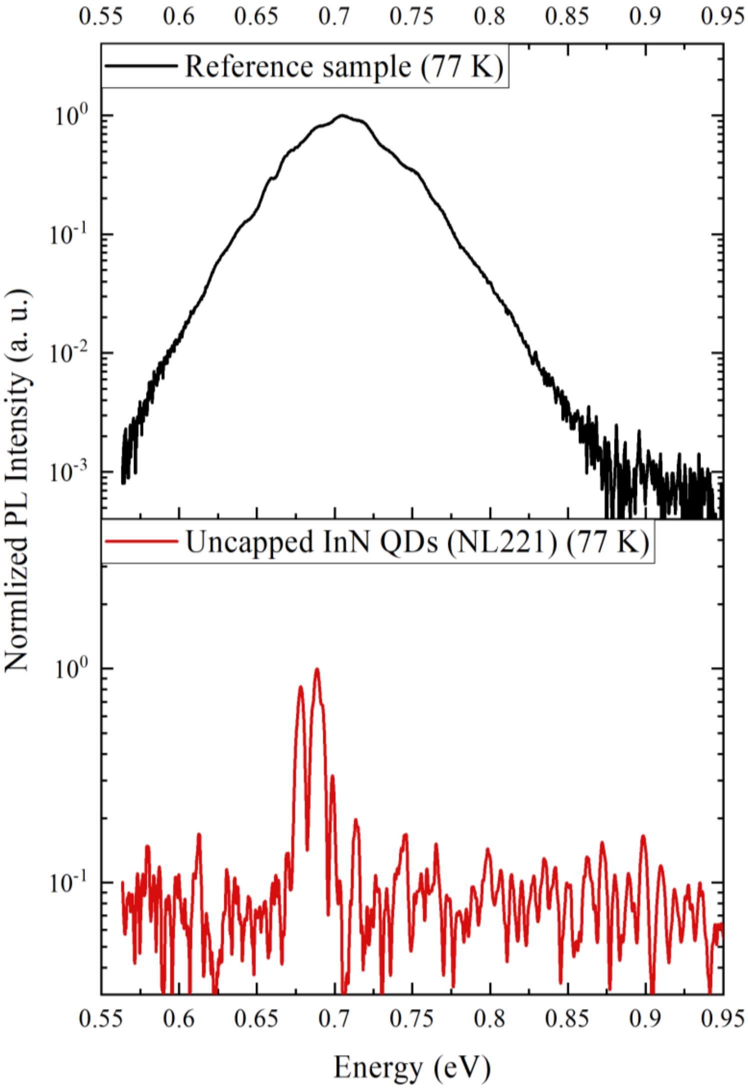

Figure 74: PL spectra of uncapped InN QDs with GaN and the reference InN film at 77 K.

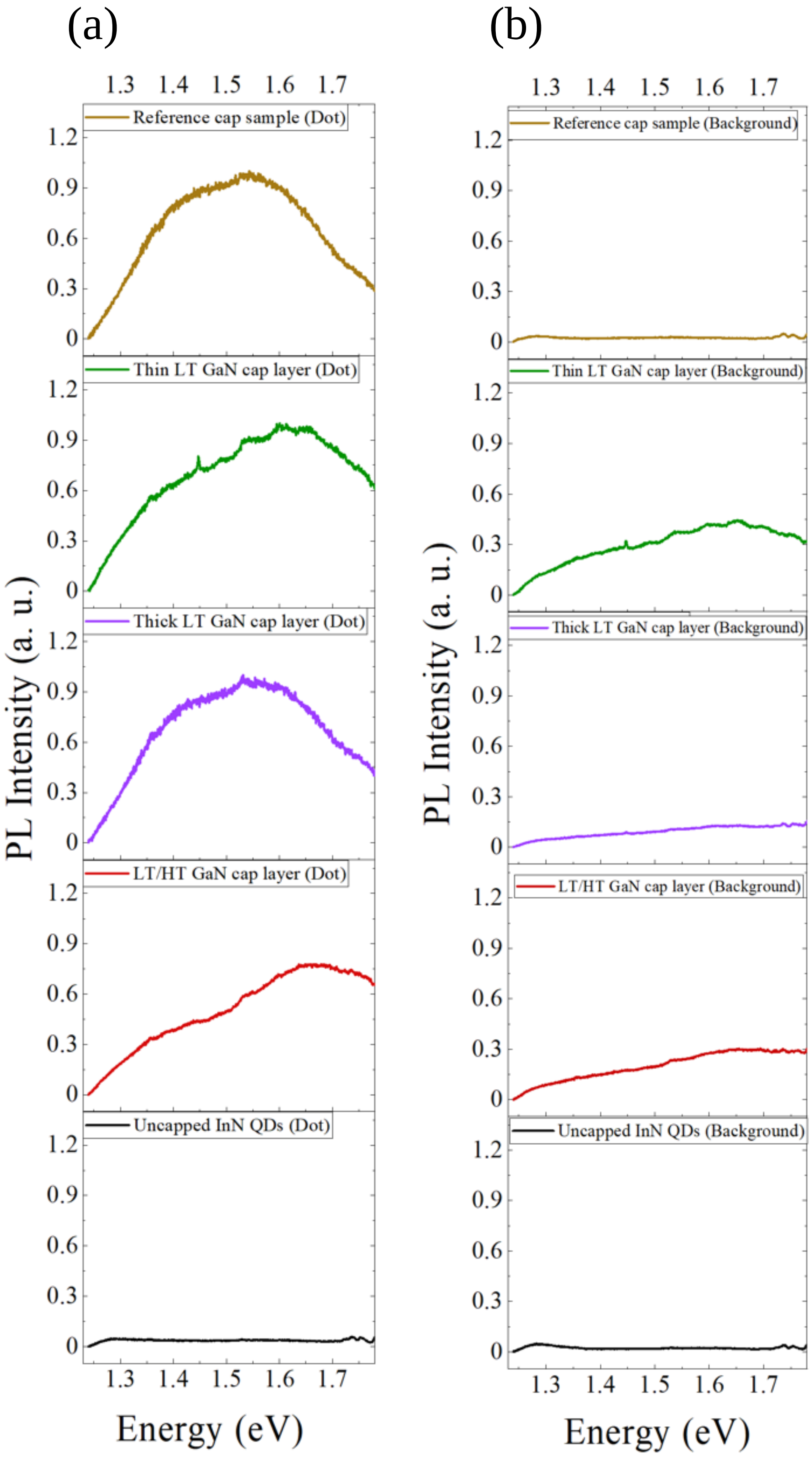

Figure 75: PL spectra of uncapped and capped InN QDs with GaN at room temperature.

Therefore, in order to examine the possibilities of InGaN formation, a Si CCD detector was employed with the samples at room temperature with a focus on spatial correlation. When the laser was directed towards one of the larger features as seen in the microscope, which were assumed to be the result of capping one of the larger dots (Figure 75 (a)), three broad emission peaks were observed at 1.68, 1.60, and 1.53 eV for the thick HT/LT GaN cap layer, thick LT GaN cap layer, and thin LT GaN cap layer, respectively. These emission peaks could have appeared due to assorted defects in GaN [119], [120] or because of InGaN formation [121]. To further investigate these samples, the laser was directed toward the background surface, i.e., away from any features as seen in the microscope (Figure 75 (b)). The peak emission intensity was reduced for the thin LT GaN cap layer and decreased for the thick HT/LT GaN cap layer until it almost disappeared for the thick LT GaN cap layers. It was acquired that the thin LT layer showed a more substantial peak at the background, which was not matched with the EDX result, and it indicated that some dots were incorporated with the GaN during the cap formation, even in a small thickness. No PL spectra were detected for the uncapped InN QDs in the dot or the background, and it corresponded with the PL spectra detected from the GaN substrate.

5.6 Conclusion

In this chapter, it was attempted to control the InN QDs sizes on GaN using the droplet epitaxy technique. The conditions for In droplets were first studied since maintaining the size is very challenging after the formation of droplets in the DE method. Then, exploring the crystallization conditions of the In droplets with nitrogen plasma in the MBE growth chamber was accomplished. Finally, the InN QDs were capped via the GaN layer to be able to use it as an active layer in any future devices.

Chapter 6: Conclusions and Future Work

6.1 Conclusions

This dissertation focused on investigating the growth of InN quantum dots (QDs) by droplet epitaxy (DE) using radio frequency plasma-assisted molecular beam epitaxy (MBE) in order to control the growth through four monolayers or ~1.3 nm of InN. The QD growth procedure from liquid In droplets to the InN QDs was described with a focus on the effect of ambient nitrogen from an active RF-plasma source on the formation of In droplets as a function of substrate temperatures on different substrates: c-plane sapphire and GaN buffer layer grown on semi-insulating GaN (0001) templates. The growth quality, dot diameter, height, and density of In droplets as well as InN QDs were investigated utilizing reflection high-energy electron diffraction (RHEED), Atomic Force Microscopy (AFM), X-Ray Diffraction (XRD), and Scanning Electron Microscope (SEM). To further understand the growth of InN QDs, the system was explored at different growth temperatures.

For the QDs formed on c-plane sapphire substrates, the nanostructures were formed under three conditions for comparison: UHV with no exposure to nitrogen; ambient of nitrogen equivalent having the plasma on but shuttered; and nitridated with the direct nitrogen plasma following droplet formation with the plasma on but shuttered. The size, density, and shape of In droplets and InN QDs were studied via controlling the substrate temperature during the In droplets formation and the crystallization process and were explained in terms of the In atom surface diffusion. The droplet formation was determined to follow well-known principles of nucleation theory with ripening. The resulting activation energy for In surface diffusion on sapphire was found to be 0.62 ± 0.07 eV in ultra-high vacuum, ~10^{-10} Torr, and 0.57 ± 0.08 eV in ambient N2, ~10^{-5} Torr.

For the InN QDs grown on a GaN buffer layer, the conditions for growing In droplets were first studied since maintaining the size was very challenging after the formation of droplets in the DE method. The droplets were formed under UHV with no nitrogen exposure to prevent both reactions with nitrogen and the diffusion suppression of elevated pressure on the growth of In droplets. The density and size of the In droplets on GaN were studied as functions of the substrate temperature during their formation and explained utilizing the In atom surface diffusion. Even at extremely low substrate temperatures of ~ 30 °C, the In atoms were extremely sensitive to the substrate temperature during the growth. The highest density of $1.36 \times 10^{8}\ cm^{-2}$ was observed at a relatively low substrate temperature of 30 °C. This study developed an understanding of the first stage of forming a controlled InN QD on GaN using DE.

In order to simulate more closely the environment under which the droplets would be formed if they were to be subsequently crystallized in the typical droplet epitaxy fashion, the In droplets were grown under a nitrogen ambient pressure of $\sim 10^{-5}$ Torr with the plasma struck but shuttered closed. Again, the density and size of the In droplets were studied as functions of the substrate temperature during their formation and described via the In atom surface diffusion. The activation energies were determined to be 0.25 ± 0.10 eV which is even lower than E_a (0.39 eV) for those formed under ultra-high vacuum, $\sim 10^{-10}$ Torr, on GaN at the same growth temperatures range. It was observed that when the substrate growth temperatures are lower than the In melting point of 156.6 °C, the In droplets density varies from the single exponential law expected through applying the nucleation theory, causing a reduction in the activation energy. Additionally, it was found that the surface diffusion length of In adatoms firmly relied on the growth temperature and the ambient N_2 background pressure. Thus, the In adatoms' surface diffusion length on the GaN surface went up with reducing the ambient N_2 background pressure.

RHEED was used to understand the necessary process and surface morphology to form droplet epitaxial InN QD on GaN. It was observed that the transition to spotty patterns appeared at ∼ 355 °C and became strong at ∼ 380 °C. After holding the T_{sub} at 380 °C for a longer time, the intensity of the patterns got even more substantial. This emphasized the formation of the InN QDs on the surface; even after 3 min of annealing at 380 °C, the pattern stayed clearly spotty. This observation was utilized to design the experiments for studying the crystallization conditions of the In droplets with nitrogen-plasma in the MBE growth chamber at different substrate temperatures: 35, 50, 100, 150, 200, and 300 °C to control the density and size of InN QDs. The resulting activation energy for InN surface diffusion on GaN was found to be 0.23 ± 0.03 eV. In addition, it was found that by analyzing the density of crystallized QDs, which followed the droplet formation under ambient N_2, a very close activation energy of 0.25 ± 0.10 eV was found.

Since the substrate temperature has significantly impacted the density and size of the InN QDs formed by droplets epitaxy, both the In droplet growth temperature and the crystallization temperature were fixed while the crystallization duration was varied, it was found that there is a slightly different variation in the droplet epitaxy InN QDs size and density between the In droplets crystallized for a shorter time and that crystallized for a longer time. For a short nitration time, the size of the QDs was 680 nm in diameter and 39.5nm in height with a density of $3.90 \times 10^7\ cm^{-2}$ while the diameter and height of the QDs were significantly reduced to 56.3 nm and 7.7 nm, respectively, but the density was considerably increased to $1.90 \times 10^{10}\ cm^{-2}$ for the sample to crystallize for a longer time. The aspect ratio showed that increasing crystallization time led to a decrease from 17.20 to 7.31. This observation of decreasing the aspect ratio for a longer crystallization time indicated a significant influence of decomposition. After controlling the growth of InN QDs through four monolayers or ~1.3 nm in height, three various GaN capping techniques were performed to cap InN QDs to be able to use as an active layer in any device. Raman spectroscopy, Photoluminescence (PL) spectroscopy, and Energy Dispersive X-Ray (EDX) were applied to investigate optical responses and crystal quality. These results should aid in developing and understanding InN QDs and QD-based devices.

6.2 Future work.

TEM analysis of InN QDs capped with GaN samples must be performed to demonstrate the presence of InN QDs. Additional capping technique optimization should be performed to establish good growth conditions for capping InN with epitaxial GaN controlling the height of the QDs and reaching the correct thickness for topological insulators. Finally, a trend in luminescence similar to a well-established PL trend of InAs QDs should be further investigated. Further study of controlling the height to reach the topological insulators should be completed. With control of the size of the QDs and achieving an optimum GaN capping, the InN QDs grown via droplet epitaxy have presented exceptional promise in accomplishing an optical response and reaching the topological insulators.

References

[1] D. Bouwmeester and A. Zeilinger, “The Physics of Quantum Information: Basic Concepts,” in *The Physics of Quantum Information*, Berlin, Heidelberg: Springer Berlin Heidelberg, 2000, pp. 1–14. doi: 10.1007/978-3-662-04209-0_1.

[2] M. Agbaje, “A review of quantum computing and its architecture,” no. April, 2019.

[3] J. Wu, Y.-L. Shen, K. Reinhardt, H. Szu, and B. Dong, “A Nanotechnology Enhancement to Moore’s Law,” *Applied Computational Intelligence and Soft Computing*, vol. 2013, pp. 1–13, 2013, doi: 10.1155/2013/426962.

[4] M. Stoneham, “Is a room-temperature, solid-state quantum computer mere fantasy?,” *Physics (College Park Md)*, vol. 2, p. 34, 2009, doi: 10.1103/physics.2.34.

[5] M. S. Miao, Q. Yan, C. G. van de Walle, W. K. Lou, L. L. Li, and K. Chang, “Polarization-Driven Topological Insulator Transition in a GaN / InN / GaN Quantum Well,” *Phys Rev Lett*, vol. 109, no. 18, p. 186803, Nov. 2012, doi: 10.1103/PhysRevLett.109.186803.

[6] G. Sun *et al.*, “Investigation of fast and slow decays in InGaN/GaN quantum wells,” *Appl Phys Lett*, vol. 99, no. 8, Aug. 2011, doi: 10.1063/1.3627166.

[7] P. W. Shor, “Polynomial-Time Algorithms for Prime Factorization and Discrete Logarithms on a Quantum Computer,” *SIAM Review*, vol. 41, no. 2, pp. 303–332, Jan. 1999, doi: 10.1137/S0036144598347011.

[8] M. H. Freedman, A. Kitaev, M. J. Larsen, and Z. Wang, “Topological quantum computation,” *Bulletin of the American Mathematical Society*, vol. 40, no. 1, pp. 31–38, Jan. 2003, doi: 10.1090/S0273-0979-02-00964-3.

[9] L. O. Mailloux, C. D. Lewis, C. Riggs, and M. R. Grimaila, “Post-Quantum Cryptography: What Advancements in Quantum Computing Mean for IT Professionals,” *IT Prof*, vol. 18, no. 5, pp. 42–47, Sep. 2016, doi: 10.1109/MITP.2016.77.

[10] S. das Sarma, M. Freedman, and C. Nayak, “Topo logical quantum computation,” *Phys Today*, vol. 59, no. 7, pp. 32–38, Jul. 2006, doi: 10.1063/1.2337825.

[11] W. Tian, W. Yu, J. Shi, and Y. Wang, “The property, preparation and application of topological insulators: A review,” *Materials*, vol. 10, no. 7, 2017, doi: 10.3390/ma10070814.

[12] S. Hussain, “Structural and optical characterization of green-yellow light emitting devices with high indium concentrated (In,Ga)N quantum wells,” Université Nice Sophia, 2015.

[13] G. E. Weng, A. K. Ling, X. Q. Lv, J. Y. Zhang, and B. P. Zhang, “III-nitride-based quantum dots and their optoelectronic applications,” *Nanomicro Lett*, vol. 3, no. 3, pp. 200–207, 2011, doi: 10.3786/nml.v3i3.p200-207.

[14] V. Rawat, D. N. Zakharov, E. A. Stach, and T. D. Sands, "Pseudomorphic stabilization of rocksalt GaN in TiN/GaN multilayers and superlattices", doi: 10.1103/PhysRevB.80.024114.

[15] J. Serrano, A. Rubio, E. Herná, A. Muñ Oz, and A. S. Mujica, "Theoretical study of the relative stability of structural phases in group-III nitrides at high pressures".

[16] N. E. Christensen, "Optical and structural properties of III-V nitrides under pressure," vol. 50, pp. 15–1994.

[17] N. v. Sidgwick, "Molecules," *Science (1979)*, vol. 86, no. 2233, pp. 336–340, Oct. 1937, doi: 10.1126/SCIENCE.86.2233.335/ASSET/29F29FD0-20A0-496C-882B-8BFF508007B1/ASSETS/SCIENCE.86.2233.335.FP.PNG.

[18] O. Ambacher *et al.*, "Pyroelectric properties of Al(In)GaN/GaN hetero- and quantum well structures," *Journal of Physics: Condensed Matter*, vol. 14, no. 13, p. 3399, Mar. 2002, doi: 10.1088/0953-8984/14/13/302.

[19] W. Paszkowicz, R. Černý, S. K.-P. Diffraction, and undefined 2003, "Rietveld refinement for indium nitride in the 105–295 K range," *cambridge.org*, 2017, doi: 10.1154/1.1566957.

[20] J. Wu *et al.*, "Unusual properties of the fundamental band gap of InN," 2002, doi: 10.1063/1.1482786.

[21] I. Bhat, "Physical properties of gallium nitride and related III–V nitrides," *Wide Bandgap Semiconductor Power Devices: Materials, Physics, Design, and Applications*, pp. 43–77, Jan. 2019, doi: 10.1016/B978-0-08-102306-8.00003-4.

[22] Hadis Morkoç and Ümit Özgür, *Zinc Oxide: Fundamentals, Materials and Device Technology* . Darmstadt: Wiley-VCH Verlag, 2009.

[23] F. Bernardini, V. Fiorentini, and D. Vanderbilt, "Spontaneous polarization and piezoelectric constants of III-V nitrides," 1997.

[24] O. K. Jani, "Development Of Wide-Band Gap InGaN Solar Cells For High-Efficiency Photovoltaics: Doctoral Dissertation," 2008.

[25] A. Yoshikawa, N. Hashimoto, N. Kikukawa, S. B. Che, and Y. Ishitani, "Growth of InN quantum dots on N-polarity GaN by molecular-beam epitaxy," *Appl Phys Lett*, vol. 86, no. 15, pp. 1–3, 2005, doi: 10.1063/1.1900948.

[26] "New physics and devices based on self-assembled semiconductor quantum dots," 2005, doi: 10.1088/0022-3727/38/13/002.

[27] B. Julsgaard, J. Sherson, J. I. Cirac, J. Fiurášek, and E. S. Polzik, "Experimental demonstration of quantum memory for light," *Nature 2004 432:7016*, vol. 432, no. 7016, pp. 482–486, Nov. 2004, doi: 10.1038/nature03064.

[28] S. Hussain, “Structural and optical characterization of green-yellow light emitting devices with high indium concentrated (In,Ga)N quantum wells,” 2016.

[29] G. E. Weng, A. K. Ling, X. Q. Lv, J. Y. Zhang, and B. P. Zhang, “III-nitride-based quantum dots and their optoelectronic applications,” *Nanomicro Lett*, vol. 3, no. 3, pp. 200–207, 2011, doi: 10.3786/nml.v3i3.p200-207.

[30] B. Damilano *et al.*, “Improved radiative efficiency using self-formed GaInN/GaN quantum dots grown by molecular beam epitaxy,” *Physica Status Solidi A Appl Res*, vol. 180, no. 1, pp. 363–368, Jul. 2000, doi: 10.1002/1521-396X(200007)180:1<363::AID-PSSA363>3.0.CO;2-R.

[31] R. W. Martin and K. P. O’Donnell, “Calculation of optical transition energies for self-formed InGaN quantum dots,” *Phys Status Solidi B Basic Res*, vol. 216, no. 1, pp. 441–444, 1999, doi: 10.1002/(SICI)1521-3951(199911)216:1<441::AID-PSSB441>3.0.CO;2-#.

[32] G. Sun *et al.*, “Investigation of fast and slow decays in InGaN/GaN quantum wells,” *Appl Phys Lett*, vol. 99, no. 8, Aug. 2011, doi: 10.1063/1.3627166.

[33] M. S. Miao, Q. Yan, C. G. Van de Walle, W. K. Lou, L. L. Li, and K. Chang, “Polarization-Driven Topological Insulator Transition in a GaN / InN / GaN Quantum Well,” *Phys Rev Lett*, vol. 109, no. 18, p. 186803, Nov. 2012, doi: 10.1103/PhysRevLett.109.186803.

[34] A. L. Rogach, *Semiconductor nanocrystal quantum dots synthesis, assembly, spectroscopy and applications*. Springer, 2008. doi: 10.1007/978-3-211-75237-1.

[35] W. J. Parak, L. Manna, F. C. Simmel, D. Gerion, and P. Alivisatos, “Quantum Dots,” in *Nanoparticles: From Theory to Application*, Second.John Wiley & Sons, Ltd, 2010, pp. 3–47. doi: 10.1002/9783527631544.CH2.

[36] G. Ramalingam *et al.*, “Quantum Confinement Effect of 2D Nanomaterials,” *Quantum Dots - Fundamental and Applications*, Jun. 2020, doi: 10.5772/INTECHOPEN.90140.

[37] O. Manasreh, *Introduction to Nanomaterials and Devices*. John Wiley and Sons, 2011. doi: 10.1002/9781118148419.

[38] A. M. Smith and S. Nie, “Semiconductor nanocrystals: Structure, properties, and band gap engineering,” *Acc Chem Res*, vol. 43, no. 2, pp. 190–200, Feb. 2010, doi: 10.1021/AR9001069/ASSET/IMAGES/LARGE/AR-2009-001069_0010.JPEG.

[39] E. U. Rafailov, “The Physics and Engineering of Compact Quantum Dot-based Lasers for Biophotonics,” pp. 7–42, 2014.

[40] P. (Paul) Harrison and A. Valavanis, *Quantum wells, wires and dots : theoretical and computational physics of semiconductor nanostructures*, 4th ed. West Sussex, England : Wiley Edition, 2016.

[41] Z. I. Alferov, “Nobel Lecture: The double heterostructure concept and its applications in physics, electronics, and technology*,” 2000.

[42] S. T. Malak *et al.*, “High-Resolution Quantum Dot Photopatterning via Interference Lithography Assisted Microstamping,” *Journal of Physical Chemistry C*, vol. 121, no. 24, pp. 13370–13380, Jun. 2017, doi: 10.1021/ACS.JPCC.7B03731/SUPPL_FILE/JP7B03731_SI_001.PDF.

[43] T. Berer *et al.*, “Lateral quantum dots in Si⁄SiGe realized by a Schottky split-gate technique,” *Appl Phys Lett*, vol. 88, no. 16, p. 162112, Apr. 2006, doi: 10.1063/1.2197320.

[44] A. A. Guzelian, U. Banin, A. v. Kadavanich, X. Peng, and A. P. Alivisatos, “Colloidal chemical synthesis and characterization of InAs nanocrystal quantum dots,” *Appl Phys Lett*, vol. 69, no. 10, pp. 1432–1434, Sep. 1996, doi: 10.1063/1.117605.

[45] D. Beke, Z. Szekrényes, I. Balogh, Z. Czigány, K. Kamarás, and A. Gali, “Preparation of small silicon carbide quantum dots by wet chemical etching,” *J Mater Res*, vol. 28, no. 1, pp. 44–49, Jan. 2013, doi: 10.1557/JMR.2012.223.

[46] V. Shchukin, N. Ledentsov, and D. Bimberg, *Epitaxy of nanostructures*. New York, Berlin: Springer, 2004.

[47] A. Yoshikawa, N. Hashimoto, N. Kikukawa, S. B. Che, and Y. Ishitani, “Growth of InN quantum dots on N-polarity GaN by molecular-beam epitaxy,” *Appl Phys Lett*, vol. 86, no. 15, pp. 1–3, 2005, doi: 10.1063/1.1900948.

[48] D. Krishnamurthy, S. Hasegawa, S. N. M. Tawil, S. Emura, and H. Asahi, “Growth of InN quantum dots by droplet epitaxy and their characterization,” *Physica Status Solidi (C) Current Topics in Solid State Physics*, vol. 9, no. 3–4, pp. 666–669, 2012, doi: 10.1002/pssc.201100329.

[49] H. J. Kim *et al.*, “Growth of In-rich InGaN/GaN quantum dots by metalorganic chemical vapor deposition,” in *Journal of Crystal Growth*, John Wiley & Sons, Ltd, Dec. 2004, pp. 95–99. doi: 10.1016/j.jcrysgro.2004.05.039.

[50] M. Kumar, M. K. Rajpalke, T. N. Bhat, B. Roul, A. T. Kalghatgi, and S. B. Krupanidhi, “Size dependent bandgap of molecular beam epitaxy grown InN quantum dots measured by scanning tunneling spectroscopy,” *J Appl Phys*, vol. 110, no. 11, p. 114317, Dec. 2011, doi: 10.1063/1.3665639.

[51] J. H. Lee, Z. M. Wang, B. L. Liang, K. A. Sablon, N. W. Strom, and G. J. Salamo, “Size and density control of InAs quantum dot ensembles on self-assembled nanostructured templates,” *Semicond Sci Technol*, vol. 21, no. 12, pp. 1547–1551, 2006, doi: 10.1088/0268-1242/21/12/008.

[52] C. L. Wu, L. J. Chou, and S. Gwo, “Size- and shape-controlled GaN nanocrystals grown on Si(111) substrate by reactive epitaxy,” *Appl Phys Lett*, vol. 85, no. 11, pp. 2071–2073,

Sep. 2004, doi: 10.1063/1.1787947.

[53] P. Aseev *et al.*, “Formation mechanisms of single-crystalline InN quantum dots fabricated via droplet epitaxy,” *J Cryst Growth*, vol. 493, pp. 65–75, 2018, doi: 10.1016/j.jcrysgro.2018.04.027.

[54] K. A. Lozovoy, A. G. Korotaev, A. P. Kokhanenko, V. v. Dirko, and A. v. Voitsekhovskii, “Kinetics of epitaxial formation of nanostructures by Frank–van der Merwe, Volmer–Weber and Stranski–Krastanow growth modes,” *Surf Coat Technol*, vol. 384, p. 125289, Feb. 2020, doi: 10.1016/J.SURFCOAT.2019.125289.

[55] A. Luque *et al.*, “Experimental analysis of the quasi-Fermi level split in quantum dot intermediate-band solar cells,” *Appl Phys Lett*, vol. 87, no. 8, p. 083505, Aug. 2005, doi: 10.1063/1.2034090.

[56] G. Linares-García *et al.*, “Optical Properties of a Quantum Dot-Ring System Grown Using Droplet Epitaxy,” *Nanoscale Res Lett*, vol. 11, no. 1, pp. 1–8, Dec. 2016, doi: 10.1186/S11671-016-1518-2/S/8.

[57] J. S. Kim and N. Koguchi, “Near room temperature droplet epitaxy for fabrication of InAs quantum dots,” *Appl Phys Lett*, vol. 85, no. 24, p. 5893, Dec. 2004, doi: 10.1063/1.1839642.

[58] M. Kumar *et al.*, “Droplet epitaxy of InN quantum dots on Si(111) by RF plasma-assisted molecular beam epitaxy,” *Adv Sci Lett*, vol. 3, no. 4, pp. 379–384, Dec. 2010, doi: 10.1166/ASL.2010.1163.

[59] M. Ohring, *Materials Science of Thin Films: Depositon and Structure* . Elsevier, 2001.

[60] W. D. Callister, *Material Science and Engineering: An Introduction*. Wiley, 1997.

[61] Fernando. Rinaldi, “Basics of molecular beam epitaxy (MBE),” *NIVERSITÄT ULM*, vol. 31, pp. 1–8, 2002.

[62] A. Yoshikawa, N. Hashimoto, N. Kikukawa, S. B. Che, and Y. Ishitani, “Growth of InN quantum dots on N-polarity GaN by molecular-beam epitaxy,” *Appl Phys Lett*, vol. 86, no. 15, pp. 1–3, 2005, doi: 10.1063/1.1900948.

[63] L. Lahourcade, “Plasma-assisted molecular beam epitaxy of (11-22)-oriented 3-nitrides,” 2009.

[64] N. Derriche, S. Godin, R. Greenwood, A. Mercado, and A. N. Warner, “Reflection High-Energy Electron Diffraction”.

[65] J. E. Mahan, K. M. Geib, and G. Y. Robinson, “A review of the geometrical fundamentals of reflection high-energy electron diffraction with application to silicon surfaces ,” *Journal of Vacuum Science & Technology A*, vol. 8, p. 3692, 1990, doi: 10.1116/1.576481.

[66] G. Haugstad, *Atomic Force Microscopy: Understanding Basic Modes and Advanced Applications*. John Wiley and Sons, 2012. doi: 10.1002/9781118360668.

[67] B. Dawn, *Scanning Probe Microscopy and Spectroscopy. Theory, Techniques, and Applications.* , 2nd ed., vol. 25 (2). Portland: Ringgold Inc, 2001.

[68] C. E. Lyman, J. I. Goldstein, A. D. Romig, Patrick. Echlin, and Charles. Fiori, *Scanning Electron Microscopy, X-Ray Microanalysis, and Analytical Electron Microscopy : a Laboratory Workbook.* Springer US, 1990.

[69] M. J. Walock, "Nanocomposite coatings based on quaternary metal-nitrogen and nanocarbon systems," University of Alabama at Birmingham, 2012.

[70] D. J. (David J. Dyson and M. Institute of Materials, *X-ray and electron diffraction studies in materials science*. Maney for the Institute of Materials, Minerals, and Mining, 2004.

[71] A. Segmüller, A. E. Blakeslee, and IUCr, "X-ray diffraction from one-dimensional superlattices in GaAs1−xPx crystals," *urn:issn:0021-8898*, vol. 6, no. 1, pp. 19–25, Feb. 1973, doi: 10.1107/S0021889873007995.

[72] M. E. Vickers, M. J. Kappers, and T. M. Smeeton, "Determination of the indium content and layer thicknesses in InGaN/GaN quantum wells by x-ray scattering," *J Appl Phys*, vol. 94, p. 1565, 2003, doi: 10.1063/1.1587251.

[73] K. Inaba, S. Kobayashi, K. Uehara, A. Okada, S. L. Reddy, and T. Endo, "High Resolution X-Ray Diffraction Analyses of (La,Sr)MnO<sub>3</sub>/ZnO/Sapphire(0001) Double Heteroepitaxial Films," *Advances in Materials Physics and Chemistry*, vol. 03, no. 01, pp. 72–89, 2013, doi: 10.4236/AMPC.2013.31A010.

[74] J. Camassel Groupe Etude des Semiconducteurs and J. Pascual, "Lattice dynamics of AgGaSe2. I. Experiment," *Phys Rev B*, vol. 41, no. 9, 1990.

[75] R. Spectroscopy and P. Rostron, "Corrosion flow loop design and build View project Balraj PhD View project," *Article in International Journal of Engineering and Technical Research*, no. 6, p. 50, 2016,

[76] R. Atalay, "Optical and Structural Properties of Indium Nitride Epilayers Grown by High-Pressure Chemical Vapor Deposition and Vibrational Studies of ZGP Single Crystal," *Physics and Astronomy Dissertations*, Dec. 2012, doi: https://doi.org/10.57709/3516443.

[77] H. Poulet, J. P. Mathieu, and M. V Klein, "Vibration Spectra and Symmetry of Crystals," *Citation: Physics Today*, vol. 31, p. 54, 1978, doi: 10.1063/1.2995144.

[78] S. Eaton-Magana and C. M. Breeding, *An Introduction to Photoluminescence Spectroscopy for Diamond and its Applications in Gemology*, no. 1. 2016.

[79] W. C. Huang *et al.*, “Investigations of GaN growth on the sapphire substrate by MOCVD method with different AlN buffer deposition temperatures,” *Mater Sci Semicond Process*, vol. 45, pp. 1–8, Apr. 2016, doi: 10.1016/J.MSSP.2016.01.008.

[80] J. M. Gérard, O. Cabrol, and B. Sermage, “InAs quantum boxes: Highly efficient radiative traps for light emitting devices on Si,” *Appl Phys Lett*, vol. 68, no. 22, pp. 3123–3125, May 1996, doi: 10.1063/1.115798.

[81] C. L. Wu, L. J. Chou, and S. Gwo, “Size- and shape-controlled GaN nanocrystals grown on Si(111) substrate by reactive epitaxy,” *Appl Phys Lett*, vol. 85, no. 11, pp. 2071–2073, Sep. 2004, doi: 10.1063/1.1787947.

[82] J. H. Lee, Z. M. Wang, and G. J. Salamo, “The control on size and density of InAs QDs by droplet epitaxy (april 2009),” *IEEE Trans Nanotechnol*, vol. 8, no. 4, pp. 431–436, 2009, doi: 10.1109/TNANO.2009.2021654.

[83] A. Krost, J. Bläsing, H. Protzmann, M. Lünenbürger, and M. Heuken, “Indium nanowires in thick (InGaN) layers as determined by x-ray analysis,” *Appl Phys Lett*, vol. 76, no. 11, p. 1395, Mar. 2000, doi: 10.1063/1.126043.

[84] C.-W. Hsu, P. Deminskyi, I. Martinovic, I. G. Ivanov, J. Palisaitis, and H. Pedersen, “Direct epitaxial nanometer-thin InN of high structural quality on 4H–SiC by atomic layer deposition,” *Appl Phys Lett*, vol. 117, no. 9, p. 093101, Sep. 2020, doi: 10.1063/5.0014900.

[85] A. Krost, J. Bläsing, H. Protzmann, M. Lu¨nenbu¨rger, and M. Heuke, “Indium nanowires in thick (InGaN) layers as determined by x-ray analysis,” *Appl. Phys. Lett*, vol. 76, p. 1395, 2000, doi: 10.1063/1.126043.

[86] C. L. Wu *et al.*, “The effects of AlN buffer on the properties of InN epitaxial films grown on Si(1 1 1) by plasma-assisted molecular-beam epitaxy,” *J Cryst Growth*, vol. 288, no. 2, pp. 247–253, Mar. 2006, doi: 10.1016/J.JCRYSGRO.2005.12.011.

[87] J. H. Lee, Z. M. Wang, N. Y. Kim, and G. J. Salamo, “Size and density control of in droplets at near room temperatures,” *Nanotechnology*, vol. 20, no. 28, p. 285602, Jun. 2009, doi: 10.1088/0957-4484/20/28/285602.

[88] A. F. Tsatsul’nikov *et al.*, “Volmer–Weber and Stranski–Krastanov InAs-(Al,Ga)As quantum dots emitting at 1.3 μm,” *J Appl Phys*, vol. 88, no. 11, p. 6272, Nov. 2000, doi: 10.1063/1.1321795.

[89] E. E. Finney and R. G. Finke, “Nanocluster nucleation and growth kinetic and mechanistic studies: A review emphasizing transition-metal nanoclusters,” *J Colloid Interface Sci*, vol. 317, no. 2, pp. 351–374, Jan. 2008, doi: 10.1016/J.JCIS.2007.05.092.

[90] D. C. Gary, B. A. Glassy, and B. M. Cossairt, “Investigation of indium phosphide quantum dot nucleation and growth utilizing triarylsilylphosphine precursors,” *Chemistry*

of Materials, vol. 26, no. 4, pp. 1734–1744, Feb. 2014, doi: 10.1021/CM500102Q/SUPPL_FILE/CM500102Q_SI_001.PDF.

[91] S. Abe, R. K. Čapek, B. de Geyter, and Z. Hens, “Tuning the postfocused size of colloidal nanocrystals by the reaction rate: From theory to application,” *ACS Nano*, vol. 6, no. 1, pp. 42–53, Jan. 2012, doi: 10.1021/NN204008Q.

[92] S. v. Balakirev, M. S. Solodovnik, and O. A. Ageev, “Hybrid Analytical–Monte Carlo Model of In/GaAs(001) Droplet Epitaxy: Theory and Experiment,” *physica status solidi (b)*, vol. 255, no. 4, p. 1700360, Apr. 2018, doi: 10.1002/PSSB.201700360.

[93] S. v. Balakirev, M. S. Solodovnik, I. A. Mikhaylin, M. M. Eremenko, and O. A. Ageev, “Analytical–Monte Carlo model of the growth of In nanostructures during droplet epitaxy on the triangle-patterned GaAs substrates,” *J Phys Conf Ser*, vol. 1124, no. 2, p. 022001, Dec. 2018, doi: 10.1088/1742-6596/1124/2/022001.

[94] J. H. Lee, Z. M. Wang, N. Y. Kim, and G. J. Salamo, “Size and density control of In droplets at near room temperatures,” *Nanotechnology*, vol. 20, no. 28, p. 285602, Jun. 2009, doi: 10.1088/0957-4484/20/28/285602.

[95] M. Kumar *et al.*, “Droplet Epitaxy of InN Quantum Dots on Si(111) by RF Plasma-Assisted Molecular Beam Epitaxy,” *Adv Sci Lett*, vol. 3, pp. 379–384, 2010, doi: 10.1166/asl.2010.1163.

[96] A. Yoshikawa, N. Hashimoto, and N. Kikukawa, “Growth of InN quantum dots on N-polarity GaN by molecular-beam epitaxy ARTICLES YOU MAY BE INTERESTED IN,” *Appl. Phys. Lett*, vol. 86, p. 153115, 2005, doi: 10.1063/1.1900948.

[97] X. Q. Shen and T. Nishinaga, “Inter-surface diffusion of In on (111)A-(001) InAs nonplanar substrates in molecular beam epitaxy,” *J Cryst Growth*, vol. 146, no. 1–4, pp. 374–378, Jan. 1995, doi: 10.1016/0022-0248(94)00550-8.

[98] R. Kremzow, M. Pristovsek, and M. Kneissl, “Ripening of InAs quantum dots on GaAs (0 0 1) investigated with in situ scanning tunneling microscopy in metal–organic vapor phase epitaxy,” *J Cryst Growth*, vol. 310, no. 23, pp. 4751–4753, Nov. 2008, doi: 10.1016/J.JCRYSGRO.2008.07.047.

[99] T. Mano *et al.*, “InAs Quantum Dots Growth by Modified Droplet Epitaxy Using Sulfur Termination,” *Jpn J Appl Phys*, vol. 39, no. 7S, p. 4580, Jul. 2000, doi: 10.1143/JJAP.39.4580.

[100] R. Togashi, T. Kamoshita, Y. Nishizawa, H. Murakami, Y. Kumagai, and A. Koukitu, “Experimental and ab-initio studies of temperature dependent InN decomposition in various ambient,” *physica status solidi c*, vol. 5, no. 6, pp. 1518–1521, May 2008, doi: 10.1002/PSSC.200778434.

[101] E. Dimakis, E. Iliopoulos, K. Tsagaraki, T. Kehagias, P. Komninou, and A. Georgakilas, "Heteroepitaxial growth of In-face InN on GaN (0001) by plasma-assisted molecular-beam epitaxy," *J Appl Phys*, vol. 97, no. 11, 2005, doi: 10.1063/1.1923166.

[102] H. J. Kim *et al.*, "The growth of In-rich InGaN/GaN single quantum wells by metalorganic chemical vapor deposition," *physica status solidi (c)*, vol. 0, no. 7, pp. 2834–2837, Dec. 2003, doi: 10.1002/pssc.200303398.

[103] S. Ruffenach, B. Maleyre, O. Briot, and B. Gil, "Growth of InN quantum dots by MOVPE," *Physica Status Solidi C: Conferences*, vol. 2, no. 2, pp. 826–832, Feb. 2005, doi: 10.1002/pssc.200460319.

[104] M. Kumar, M. K. Rajpalke, T. N. Bhat, B. Roul, A. T. Kalghatgi, and S. B. Krupanidhi, "Size dependent bandgap of molecular beam epitaxy grown InN quantum dots measured by scanning tunneling spectroscopy," *J Appl Phys*, vol. 110, no. 11, p. 114317, Dec. 2011, doi: 10.1063/1.3665639.

[105] Z. M. Wang, J. H. Lee, and B. L. Liang, "Localized formation of InAs quantum dots on shallow-patterned GaAs(100)," *Appl. Phys. Lett*, vol. 88, p. 233102, 2006, doi: 10.1063/1.2209157.

[106] T. Noda, T. Mano, and H. Sakaki, "Anisotropic Diffusion of In Atoms from an In Droplet and Formation of Elliptically Shaped InAs Quantum Dot Clusters on (100) GaAs," vol. 11, pp. 726–728, 2011, doi: 10.1021/cg101210d.

[107] A. Raab and G. Springholz, "Oswald ripening and shape transitions of self-assembled PbSe quantum dots on PbTe (111) during annealing," *Appl Phys Lett*, vol. 77, no. 19, p. 2991, Nov. 2000, doi: 10.1063/1.1323733.

[108] M. Kumar *et al.*, "Kinetics of self-assembled InN quantum dots grown on Si (111) by plasma-assisted MBE," *Journal of Nanoparticle Research*, vol. 13, no. 3, pp. 1281–1287, Mar. 2011, doi: 10.1007/S11051-010-0121-1/S/9.

[109] J. A. Venables, G. D. T. Spiller, and M. Hanbucken, "Nucleation and growth of thin films," *Reports on Progress in Physics*, vol. 47, no. 4, pp. 399–459, 1984, doi: 10.1088/0034-4885/47/4/002.

[110] A. Tuktamyshev *et al.*, "Reentrant Behavior of the Density vs. Temperature of Indium Islands on GaAs(111)A", doi: 10.3390/nano10081512.

[111] C. Heyn, A. Stemmann, A. Schramm, H. Welsch, W. Hansen, and Á. Nemcsics, "Regimes of GaAs quantum dot self-assembly by droplet epitaxy", doi: 10.1103/PhysRevB.76.075317.

[112] H. Schulz and K. H. Thiemann, "Crystal structure refinement of AlN and GaN," *Solid State Commun*, vol. 23, no. 11, pp. 815–819, Sep. 1977, doi: 10.1016/0038-1098(77)90959-0.

[113] F. Ivaldi *et al.*, “Influence of a GaN cap layer on the morphology and the physical properties of embedded self-organized InN quantum dots on GaN(0001) grown by metal-organic vapour phase epitaxy,” *Jpn J Appl Phys*, vol. 50, no. 3, p. 031004, Mar. 2011, doi: 10.1143/JJAP.50.031004/XML.

[114] S. Bietti, C. Somaschini, L. Esposito, A. Fedorov, and S. Sanguinetti, “Gallium surface diffusion on GaAs (001) surfaces measured by crystallization dynamics of Ga droplets,” *J Appl Phys*, vol. 116, no. 11, p. 114311, Sep. 2014, doi: 10.1063/1.4895986.

[115] M. Dejarld, K. Reyes, P. Smereka, and J. M. Millunchick, “Mechanisms of ring and island formation in lattice mismatched droplet epitaxy,” *Appl Phys Lett*, vol. 102, no. 13, p. 133107, Apr. 2013, doi: 10.1063/1.4799965.

[116] D. Fuster, K. Abderrafi, B. Alén, Y. González, L. Wewior, and L. González, “InAs nanostructures grown by droplet epitaxy directly on InP(001) substrates,” *JCrGr*, vol. 434, pp. 81–87, Jan. 2016, doi: 10.1016/J.JCRYSGRO.2015.11.003.

[117] “Quantum Dots Prepared by Droplet Epitaxial Method Ákos Nemcsics,” 2015, doi: 10.5772/60823.

[118] M. R. Correia *et al.*, “Direct evidence for strain inhomogeneity in InxGa1−xN epilayers by Raman spectroscopy,” *Appl Phys Lett*, vol. 85, no. 12, p. 2235, Sep. 2004, doi: 10.1063/1.1791324.

[119] M. A. Reshchikov and H. Morkoç, “Luminescence properties of defects in GaN,” *J. Appl. Phys*, vol. 97, p. 61301, 2005, doi: 10.1063/1.1868059.

[120] S. Limpijumnong and C. G. Van de Walle, “Diffusivity of native defects in GaN,” *Phys Rev B*, vol. 69, no. 3, p. 035207, Jan. 2004, doi: 10.1103/PhysRevB.69.035207.

[121] N. A. El-Masry, E. L. Piner, S. X. Liu, and S. M. Bedair, “Phase separation in InGaN grown by metalorganic chemical vapor deposition,” *Appl Phys Lett*, vol. 72, no. 1, p. 40, Jun. 1998, doi: 10.1063/1.120639.

Appendix A: Description of Research for Popular Publication

Title: InN QDs growth
By: Malak Refaei

A topological insulator is a novel phase of matter which can be achieved in semiconductor materials, and it has a feature of a conducted surface and an insulated bulk, which might be exploited for quantum computing. The prediction that indium nitride thin film can become a two-dimensional (2D) topological insulator was the primary motivation for doing this research. A step toward achieving this novel system was made by investigating the growth of indium nitride quantum dots using the droplets epitaxy method in molecular beam epitaxy (MBE) was taken by Malak Refaei, a Ph.D. student in Dr. Morgan Ware's research group at the University of Arkansas. You would ask what MBE is, why do you want to grow quantum dots, and what droplet epitaxy is. To answer these questions, let me start with MBE. MBE is the most common device used to grow a high-quality semiconductor material with different structures with sizes ranging from a few nanometers to micrometers.

Ms. Malak's research focused on developing the growth of indium nitride quantum dots. The indium nitride (InN) material has many growth challenges among other members of the III-nitride semiconductor materials family due to its complicated low-temperature growth, which makes it harder to grow a high-quality thin film without having so many defects or issues. Therefore, Ms. Malak and her advisor, Dr. Morgan Ware, considered growing quantum dots (QDs) to the same height as in a thin film. Also, instead of using the traditional way to grow the quantum dots, the droplets epitaxy method was chosen to grow the InN QDs. This method has worked well in growing QDs using other materials, but very little research has been done on growing InN QDs. This method is better than other QDs' growth methods because it can control the size of the QDs and can be grown on any other materials with minimum effects.

Now, let us explain what the quantum dot is. Quantum dots are a very tiny crystal structures, with dimensions on the order of only a few nanometers. These small crystals can trap an electron inside, which behaves differently than in a standard semiconductor material. By changing the size of the QDs, it can reach the transition to the topological insulator state. However, since the growth of InN QDs is still new and very challenging, Ms. Malak’s work has not investigated the possibilities of this transition. Instead, it focuses only on understanding and developing the growth of InN QDs using droplet epitaxy with a focus on the effects of ambient nitrogen, substrate types, and substrate growth temperatures which can be used as a foundation for future research.

Appendix B: Executive Summary of Newly Created Intellectual Property

The growth of the InN QDs using droplets epitaxy technique in MBE was extensively studied with a focus on the effects of ambient nitrogen, substrate types, and substrate growth temperatures in order to discover and learn to control the growth kinetics of this novel system. The main results attained in the course of this research are reviewed in the following list.

1. Controlling the density and size of InN QDs formed on sapphire substrate via droplet epitaxy using radio frequency molecular beam epitaxy was investigated. This investigation was accomplished with a focus on the effects of ambient nitrogen and substrate growth temperatures.
2. The self-assembled strain free growth of InN QDs grown on GaN using droplet epitaxy using radio frequency molecular beam epitaxy with a focus on the effects of ambient nitrogen and substrate growth temperatures was investigated. Also, the crystallization process was investigated under the effect of substrate growth temperatures and crystallization duration.

Appendix C: Potential Patent and Commercialization Aspects of Listed Intellectual Property Items

C.1 Patentability of Intellectual Property

There is not any intellectual property for patent consideration because there were not any devices that fabricated in this research. However, the process used to grow the InN QDs could be considered for patented. This process used to grow InN QDs on sapphire substrate and on GaN buffer layer are not novel and cannot be patented.

C.2 Commercialization Prospects

The method used in this research is not appropriate for a patent since it was already commercialized.

C.3 Possible Prior Disclosure of IP

There is no prior disclosure of IP in this work.

Appendix D: Broader Impact of Research

D.1 Applicability of Research Methods to Other Problems

The research methods used in this research is beneficial for investigation and understanding the QDs growth kinetics from the formation of liquid metal droplets to the crystallized QDs of other material systems.

The materials characterization techniques utilized in this research including Reflection High Energy Electron Diffraction (RHEED), Atomic Force Microscope (AFM), Scanning electron microscopy (SEM), Energy Dispersive X-ray Spectroscopy (EDX), and X-ray Diffraction (XRD) are appropriate to any other crystal growth. These analytical methods are beneficial to exploring the growth quality and characterize the surface morphology, uniformity, size distribution, and density of the droplets and QDs.

The plasma-assisted molecular beam epitaxy (MBE), which was utilized in this work, could be suitable to grow nanostructure of any other material systems.

D.2 Impact of Research Results on U.S. and Global Society

This research can assistant in develop an understanding of the InN QDs growth kinetics using droplets epitaxy which can be beneficial for future optoelectronic and electronic applications. Being a part of developing these future applications can make an impact on U.S. or Global Societies.

D.3 Impact of Research Results on the Environment

This research does not have any negative impact on the environment since InN and GaN are not hazardous materials. the InN QDs can be used as an active layer in solar cells which can decrease the impact of current fossil fuels and thus reduce pollution.

Appendix E: Microsoft Project for PhD MicroEP Degree Plan.

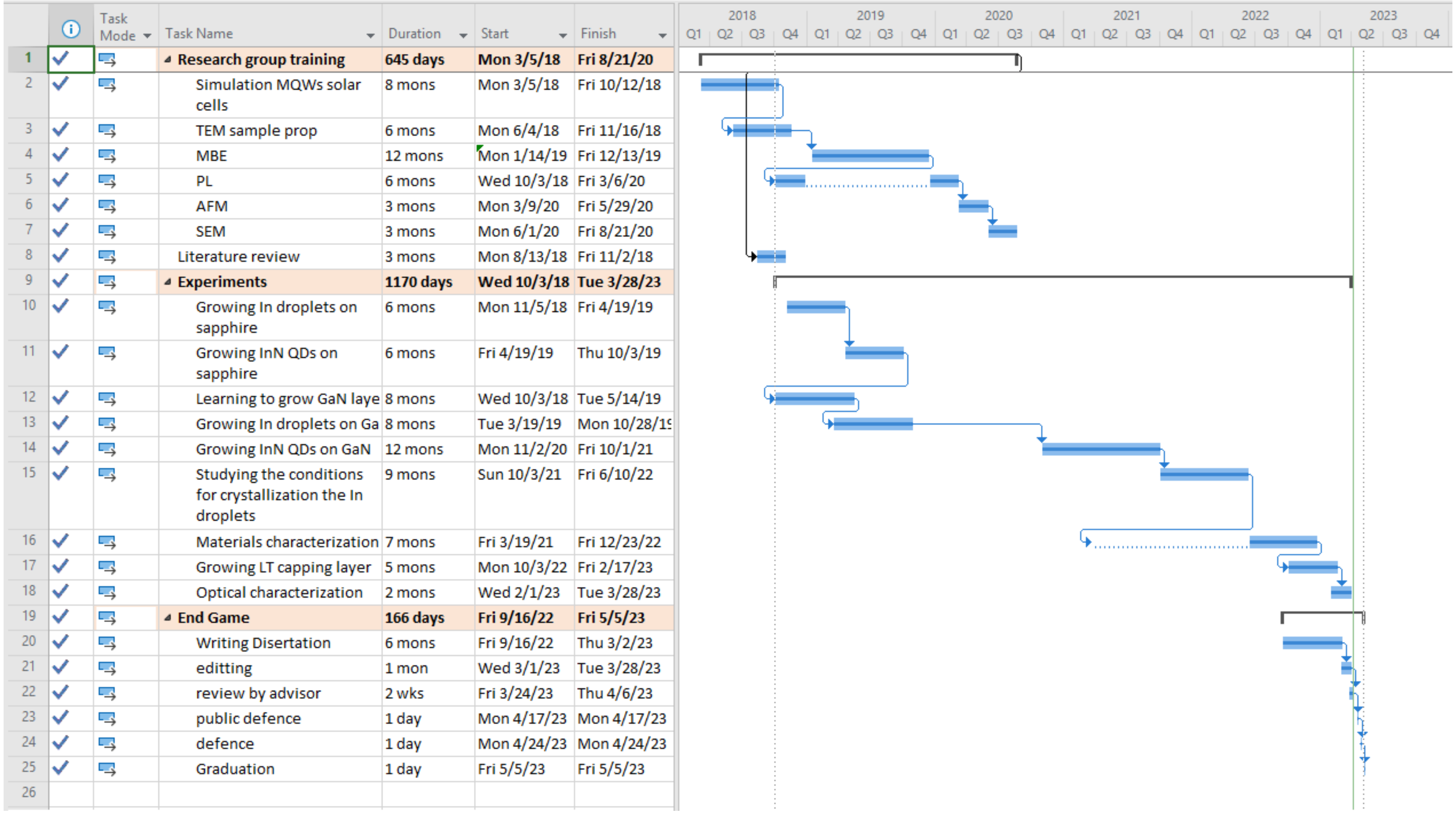

	ⓘ	Task Mode	Task Name	Duration	Start	Finish
1	✓		**Research group training**	**645 days**	**Mon 3/5/18**	**Fri 8/21/20**
2	✓		Simulation MQWs solar cells	8 mons	Mon 3/5/18	Fri 10/12/18
3	✓		TEM sample prop	6 mons	Mon 6/4/18	Fri 11/16/18
4	✓		MBE	12 mons	Mon 1/14/19	Fri 12/13/19
5	✓		PL	6 mons	Wed 10/3/18	Fri 3/6/20
6	✓		AFM	3 mons	Mon 3/9/20	Fri 5/29/20
7	✓		SEM	3 mons	Mon 6/1/20	Fri 8/21/20
8	✓		Literature review	3 mons	Mon 8/13/18	Fri 11/2/18
9	✓		**Experiments**	**1170 days**	**Wed 10/3/18**	**Tue 3/28/23**
10	✓		Growing In droplets on sapphire	6 mons	Mon 11/5/18	Fri 4/19/19
11	✓		Growing InN QDs on sapphire	6 mons	Fri 4/19/19	Thu 10/3/19
12	✓		Learning to grow GaN laye	8 mons	Wed 10/3/18	Tue 5/14/19
13	✓		Growing In droplets on Ga	8 mons	Tue 3/19/19	Mon 10/28/1
14	✓		Growing InN QDs on GaN	12 mons	Mon 11/2/20	Fri 10/1/21
15	✓		Studying the conditions for crystallization the In droplets	9 mons	Sun 10/3/21	Fri 6/10/22
16	✓		Materials characterization	7 mons	Fri 3/19/21	Fri 12/23/22
17	✓		Growing LT capping layer	5 mons	Mon 10/3/22	Fri 2/17/23
18	✓		Optical characterization	2 mons	Wed 2/1/23	Tue 3/28/23
19	✓		**End Game**	**166 days**	**Fri 9/16/22**	**Fri 5/5/23**
20	✓		Writing Disertation	6 mons	Fri 9/16/22	Thu 3/2/23
21	✓		editting	1 mon	Wed 3/1/23	Tue 3/28/23
22	✓		review by advisor	2 wks	Fri 3/24/23	Thu 4/6/23
23	✓		public defence	1 day	Mon 4/17/23	Mon 4/17/23
24	✓		defence	1 day	Mon 4/24/23	Mon 4/24/23
25	✓		Graduation	1 day	Fri 5/5/23	Fri 5/5/23
26						

Appendix F: Identification of All Software Used in Research and Dissertation Generation

Computer #1:
- Model Number: SVF14AC1QL
- Serial Number: 4-465-345-31
- Location: 1602 N Merion Way
- Owner: Malak Refaei

Software #2:
- Name: Nextnano software
- license Key: 2B4CAE39A
- Purchased by: Dr. Morgan Ware

Software #3:
- Name: Microsoft Office 2013
- Purchased by: Malak Refaei

Software #4:
- Name: Microsoft Project 2010
- Purchased by: MSDN Academy Alliance through Engineering

Software #5:
- Name: Origin 2019
- Purchased by: Malak Refaei

Software #6:
- Name: Nanoscope Analysis Software V1.50
- Purchased by: Free.

Software #7:
- Name: Mendeley Desktop ver. 1.19.4
- Purchased by: Free

Appendix G: All Publications Published, Submitted and Planned

Published

[1] **Refaei Malak**, Rohith Allaparthi, Mirsaeid Sarollahi, and Morgan E. Ware. "Investigating self-assembled strain-free growth of In droplets on GaN using droplet epitaxy." *In Gallium Nitride Materials and Devices XVIII*, vol. 12421, pp. 179-185. SPIE, 2023.

[2] Abu-Safe, Husam H., Kawther M. Al-Adamat, Husam El-Nasser, **Malak Refaei**, Mirsaeid Sarollahi, Reem Alhelais, and Morgan E. Ware. "Investigation of linear and nonlinear optical properties of amorphous carbon nanofilms prepared by electron beam evaporation." *Applied Surface Science* 576 (2022): 151818.

[3] Sarollahi, Mirsaeid, Mohammad Zamani-Alavijeh, Rohith Allaparthi, Manal A. Aldawsari, **Malak Refaei**, Reem Alhelais, Md Helal Uddin Maruf, Yuriy I. Mazur, and Morgan E. Ware. "Study of simulations of double graded InGaN solar cell structures." *Journal of Vacuum Science & Technology B, Nanotechnology and Microelectronics: Materials, Processing, Measurement, and Phenomena* 40, no. 4 (2022): 042203.

[4] Sarollahi, Mirsaeid, Mohammad Zamani-Alavijeh, Manal A. Aldawsari, Rohith Allaparthi, Md Helal Uddin Maruf, **Malak Refaei**, Reem Alhelais, Yuriy I. Mazur, and Morgan E. Ware. "Modeling of temperature dependence of Λ-graded InGaN solar cells for both strained and relaxed features." *Frontiers in Materials* 9 (2022): 1006071.

[5] Sarollahi, Mirsaeid, Mohammad Zamani Alavijeh, Rohith Allaparthi, Reem Alhelais, **Malak Refaei**, Md Helal Uddin Maruf, and Morgan E. Ware. "Modeling of V graded In(x)Ga(1-x)N solar cells: comparison of strained and relaxed features." *arXiv preprint arXiv:2202.03510* (2022).

[6] Sarollahi, Mirsaeid, Rohith Allaparthi, Reem Alhelais, Manal A. Aldawsari, **Malak A. Refaei**, Md Helal Uddin Maruf, and Morgan E. Ware. "Effects of numbers of wells on optical properties of periodic InGaN graded structure." *In Low-Dimensional Materials and Devices 2021*, vol. 11800, pp. 54-60. SPIE, 2021.

[7] Sarollahi, Mirsaeid, Pijush K. Ghosh, Manal A. Aldawsari, Shiva Davari, **Malak I. Refaei,** Reem Alhelais, Yuriy I. Mazur, and Morgan E. Ware. "Experiment-simulation comparison of luminescence properties of GaN/InGaN/GaN double graded structures." Journal of Luminescence 240 (2021): 118411.

[8] Abu-Safe, Husam H., Razan Al-Esseili, Hussein Al-Taani, Husam El-Nasser, **Malak Refaei**, Mirsaeid Sarollahi, Reem Alhelais, Mohammad Zamani-Alavijeh, and Morgan E. Ware. "The nonlinear optical properties of nickel nano-films in the cw regime: Proposed model." *Optical Materials* 121 (2021): 111531.

[9] Abu-Safe, H. H., R. Al-Esseili, M. Sarollahi, **M. Refaei**, H. Naseem, M. Zamani-Alavijeh, T. AlAbdulaal, and M. E. Ware. "Thermally-induced nonlinear optical properties of silver nano-films near surface plasmon resonance." *Optical Materials* 105 (2020): 109858.

[10] Abu-Safe, Husam H., Razan Al-Esseili, Husam El-Nasser, Mirsaeid Sarollahi, **Malak Refaei**, Mohammad Zamani-Alavijeh, Hameed Naseem, and Morgan E. Ware. "Au–Ag–Al Nano-Alloy Thin Films as an Advanced Material for Photonic Applications: XPS Analysis, Linear and Nonlinear Optical Properties Under CW Regime." *Crystal Research and Technology* 55, no. 6 (2020): 1900228.

Submitted

[1] **Refaei, Malak**, Kuchuk Andrian, Rohith Allaparthi, Mirsaeid Sarollahi, Maruf Md Helal Uddin and Morgan E. Ware. “Controlling the Size and Density of InN QDs formed on Sapphire Substrate by Droplet Epitaxy” has been submitted to JVST and still under reviewing.